Exploring the Standard and Extended Cosmological Models Using High-Precision Large Scale Observations

by

Anqi Chen

A dissertation submitted in partial fulfillment
of the requirements for the degree of
Doctor of Philosophy
(Physics)
in the University of Michigan
2021

Doctoral Committee:

Professor Dragan Huterer, Chair
Professor August E. Evrard
Professor Douglas O. Richstone
Professor Leopoldo A. Pando Zayas
Professor Junjie Zhu

Anqi Chen
anqich@umich.edu

ORCID iD: 0000-0003-0201-9971

Acknowledgements

I greatly appreciate the help and the recognition I got from many people on this journey. The first person I want to thank is my adviser Professor Dragan Huterer. He has that attitude of always being positive and straightforward, which I really want to learn from. I cannot finish many of my researches if it was not because of his encouragement. Needless to say, his academic skills and experience have also been very beneficial to me.

Next I want to thank my Dark Energy Survey colleagues, especially my office mates Jessie Muir and Noah Weaverdyck, and Agnes Ferte, Lucas Secco, among many others in the small-scales and extensions analysis group. We had countless useful discussions, and worked with each other through many hard problems. I miss the drinks after the collaboration meetings very much.

I thank Professor Scott Dodelson for his useful cosmology book and being the kind of physicist that I want to become.

I thank my friends in the physics department and the staff that provided a supportive environment for our research.

I thank Callum Jones and Judy Dyer, who spent their time to save my broken grammar in the draft of this manuscript.

I thank my committee members, Dragan Huterer, August Evrard, Leopoldo A. Pando Zayas, Douglas Richstone and Junjie Zhu for reading and evaluating my thesis.

Last but not least, I thank my father and step mother for their unconditional love.

Preface

I would like this thesis to be a useful and readable document for me, and possibly for someone else who is interested in the same topic. I intend to make this thesis a place where I book-keep my understanding on the cosmology, important derivations and conclusions, ideas, and useful references. I did spend some efforts on trying to make the story self-consistent for everyone in the first three chapters, although not sure how successful it is. I might be able to see how this thesis works on serving the above purposes in one or two years by seeing if I am or anyone else is going to look back on this manuscript.

Chapter 1-3, 6, 7 could be more useful to readers outside the Dark Energy Survey and similar collaborations. Chapter 1-3 are reviews of limited aspects of modern cosmology theory, which start from Einstein equations and other essential assumptions in ΛCDM model and end with cosmic microwave background temperature spectrum and large scale structure two-point correlation functions. Chapter 6 presents the constraint on a specific extended cosmological model, where dark matter converts into dark radiation. Chapter 7 discusses general concerns on the topic of the combined probes cosmology.

On the other hand, Chapter 4, 5 are more technical, focusing on the analysis details in the Dark Energy Survey pipeline, including the baryonic effects in cosmic shear analysis and the statistical interpretation for cosmological parameters and models.

Table of Contents

List of Tables

List of Figures

List of Appendices

Abstract

Modern precision cosmology is undergoing rapid development thanks to the measurements obtained from large scale cosmological surveys. This information both elucidates our knowledge about the universe and brings in new challenges. The first challenge is to robustly analyze the growing amount of data that need further compression and post-processes, in order to produce the cosmological interpretation correctly. The second challenge is to propose and constrain extended cosmological models that can potentially resolve the tensions appearing in the high-precision measurements. In this thesis, I first summarize modern cosmology theory predictions on background and perturbation level in chapter 13. Chapter 4-6 are about my research in the Dark Energy Survey on different topics. In Chapter 4, I present my investigation on the theory systematic uncertainty caused by baryonic feedbacks in the cosmic shear analysis, for the Dark Energy Survey Year-3 precision. The conclusion is that introducing two extra halo parameters to describe the baryonic effect can protect us from biasing the cosmological parameter constraints, but the gain on the constraint power from the small scale is too small to worth doing so. Next, in chapter 5, I discuss several technical details in terms of the statistics being done to verdict the conclusions on the extended cosmological parameters and models in DES Year-1 extensions paper. The conclusion is that the kernel used for kernel density estimation should always be linearly corrected for the Monte Carlo chains in a blinded cosmological analysis. In Chapter 6 I constrain on a phenomenological model where dark matter converts to dark radiation at low redshifts, using the Dark Energy Survey Year-1 data combined with external data. The conclusion is that when combining all data sets less than 3.7% in fraction of the current amount of dark matter could have been converted away. Furthermore, the extended model does not help much on H_0 or S_8 tensions between early and late universe measurements, and it does not fit the data better (or worse) than the ΛCDM model at current precision. Finally, in chapter 7, I further the discussion on the problem of certain ΛCDM assumptions used in the combined-probe analysis for extended cosmological models.

Chapter 1

Introduction

Although people tend to consider cosmology a long-standing research field, since human-beings have a long history contemplating the birth, existence and the future of our universe, modern cosmology is actually a young and lively developing intersection of astrophysics and high-energy physics. In fact modern cosmology as a precision science, incorporating a solid theory basis and rich observations, started only a mere 100 years ago. The foundation of modern cosmology is considered to be Albert Einstein's theory of general relativity [5], and another cornerstone is set by the observation of the expanding universe by Edward Hubble [6].

In recent decades, the increasing amount of information we have obtained from cosmological observation has been stunning, which is the essential reason for the prosperity of this research area. Physics is a discipline about building mathematical models to describe the behavior of the universe. Only with quantitative observations constantly flowing in could physicists have enough information to validate the established theories and to spot the anomalies that lead to the new, more complete theories. In the 21st century, newly-observed or high-precision cosmological signals include among others are: the large scale structure of galaxy clustering [7–9], cosmic microwave background [10], Supernovae [11], gravitational waves [12], black hole event horizons [13], 21 cm absorption feature [14], and strong gravitational lensing [15]. Most of the observations so far confirm our standard cosmological model, ΛCDM, while slight anomalies are appearing with increasing statistical significance. For this reason, how to interpret the large amount of information and to approach the statistical and systematic uncertainties in cosmology are crucial questions for the future of this discipline and for the entire physics community. With the current pace of incoming observations, and if we can interpret them carefully and correctly, I personally am confident that our understanding of the universe will take a leap in the next few decades.

In the following two sections I briefly introduce cosmology theory and observations, and close the introduction by providing an overview of how this thesis is organized.

1.1 Cosmology: Theory

In modern cosmology a theory, or a cosmological model, usually has to provide answers to the following three questions:

- The expansion history of the universe. We have known since 1929 that our universe is expanding, as that the distant galaxies are drifting away [6]. A cosmological model needs to be able to provide an explanation and prediction for these observations.

- The metric perturbations on linear (large) scales. We observe the distribution of galaxy clusters and find non-trivial statistical features in these tracers, such as halos and filaments consist of the matter over-densities [16]. Again, a cosmological model has to accommodate these large scale structures.

- The initial condition of the universe. Our universe is highly correlated on super-horizon scales and the standard explanation for this is inflation [17]. A cosmological model must further specify the model for the inflation and be able to set the initial power of perturbations.

It is not difficult to see that the framework of cosmological models is built upon the demands of explaining some of the most basic and uncontroversial observations of our universe. Starting from a gravitational theory, physicists construct a cosmological model by specifying the symmetry and the content of the universe. The most successful "Standard Model" in modern cosmology is the ΛCDM model, which adopts Einstein's general relativity, assuming a homogeneous, isotropic and flat universe, and claims that the components of the universe are baryons, photons, dark matter and dark energy.

A detailed description of ΛCDM and its extensions is provided in the second chapter of this thesis.

1.2 Cosmology: Large Scale Observations

Modern precision cosmology has constrained the parameters that specify the cosmological model down to 1%-10% uncertainty. For example, we learned from the most recent Planck 2018 cosmic microwave background data that the matter (dark matter and baryons) takes up $31.5\% \pm 1\%$ of the total energy, and the age of our universe is 13.80 ± 0.02 Gyr [10]. The modern cosmological survey analysis is no longer straightforward mathematics, but cooperative data engineering, a very involving pipeline of compressing the information and statistically interpreting it. Here I briefly introduce the major probes in cosmology and

their surveys. These are mostly on large scales, where the measured objects spread over the distances larger than galaxy cluster sizes. Arguably, it is how we conventionally categorize them as "cosmological" in certain context.

- Cosmic Microwave Background. CMB temperature and polarization anisotropy is the most constraining cosmological probe in the current generation of surveys, due to the cleanness of its signal. After leaving the last scattering surface, the photons are traveling through an almost opaque medium in the universe. Modern CMB surveys make high precision maps of the perturbation fields of background light in the sky, compressing it into the power spectrum to extract their statistical distribution features, then compare the power spectrum with theory predictions. Completed and current CMB surveys include COBE [18], WMAP [19], Planck [10], SPT [20], and ACT [21]. Major next generation CMB missions are the space based CORE science program [22], and the ground based CMB-S4 experiment [23].

- Galaxy clustering and weak lensing surveys. These are the surveys that this thesis mostly focuses on. The distribution of galaxies and mass perturbations are not completely random in our universe, but infuse the features determined by the initial condition and the expansion of the universe. The lowest order statistic description of such distribution is the two-point correlation function or the dipole spectrum taken from galaxy maps. Galaxy positions and shapes are usually affected by galaxy bias, so the cleaner mass tracer, weak lensing shear, is used in later surveys to avoid the galaxy bias uncertainty. An incomplete list of past and current galaxy clustering and weak lensing surveys includes CFHTLS [24], SDSS [25], KiDS [7] and DES [9]. Major future surveys are the space-based Euclid [26], Nancy Grace Roman Space Telescope [27], and ground based DESI [28], Vera Rubin Observatory LSST [29].

- Supernovae. Type Ia Supernovae are proposed as "standard candles" due to their uniform absolute magnitude [30]. The supernova Hubble diagram is a powerful probe to the late universe expansion history, which compiles the data of Supernovae redshifts and luminosity distances. The type Ia supernovae redshifts can be obtained from the spectral observations of their host galaxies and their calibrated or uncalibrated distances can be inferred from their luminosity. There are many surveys observing Type Ia supernovae, and a recent compilation of supernovae samples that is widely used by the cosmologists is Pantheon [11].

- Baryonic Acoustic Oscillations. Before the decoupling of photons and baryons after recombination, the two components are tightly coupled through Compton scattering.

Hence the sound horizon frozen at the last scattering surface is not preserved in the fluctuation of photons, but also in the fluctuation in the baryons. We call this feature in the galaxy clustering baryonic acoustic oscillations (BAO) [31]. The sound horizon scale is a standard ruler, so BAO observed at different redshifts are often used as geometry measurements. Most of the galaxy clustering and weak lensing surveys mentioned before are also able to carry out BAO analysis. The most constraining BAO measurements in the current generation are made by BOSS as a part of SDSS-III [8].

Other than the relatively mature large scale data products described above, gravitational-wave standard sirens [32], and 21 cm intensity maps probing cosmic dawns [33] are also promising future large scale observations.

1.3 The Outline of This Thesis

The goal of this thesis is to convey a coherent story of how we investigate the properties of our universe based on inputs from large scale observations, and to give details on the specific projects that the author contributed to for this big background purpose. In chapter 2, the standard model of modern cosmology, ΛCDM, will be described, describing "What" we are investigating about our universe. Chapter 3 is dedicated to "How" we investigate our universe, focusing on the galaxy clustering and weak lensing shear probes, which is the expertise of the author. Chapter 4 focuses on the project of baryonic effect uncertainty mitigation for Dark Energy Survey, which contributed to the DES-Y3 3x2pt data analysis. Chapter 5 outlines the author's work on DES extension model constraints. Chapter 6 is concerned with constraining decaying dark matter model using DES combined with other cosmological probes, which largely comes from the manuscript Chen (DES collab.) *et al.* [34]. The thesis ends with a consideration of future survey beyond-ΛCDM model analysis.

In summary, chapters 1-3 are based on fairly well-established work, and chapters 4-7 are based on original work carried out by the author with colleagues.

Chapter 2

Standard and Extended Cosmological Models

In this chapter, I will give a detailed description of the currently most successful cosmological model favored by various observations, ΛCDM, and some extensions to it.

2.1 Preview of the Full Story

Like summarized in the previous chapter, ΛCDM is a model stating that:

In our universe, the law of gravity is Einstein's general relativity. Our universe has a homogeneous, isotropic and flat background metric. An inflationary process set the initial conditions in our universe. The components of the universe consist of baryons, photons, dark matter and dark energy.

Under these facts or assumptions, and the particle standard model description of the interaction of baryonic matter and lights, the universe went through this time line (listing only the most important nodes) :

- Inflation. Inflation was first proposed as a solution to the flatness and horizon problems [17, 35]. If the universe starts from a hot plasma with only radiation and matter, the time before last scattering (CMB) is not long enough to bring the photons in the observed patch of the universe into causal connection, thus posing a question of why our CMB is so isotropic down to the precision one in 10^5. Hence inflation, an exponentially expanding period of the universe is needed to resolve this contradiction. If we travel backward the timeline of inflation, the observed patch of the universe at present could be contained in a small enough patch that is causally connected. Such rapid expansion of the universe could be caused by the domination of the almost constant potential

energy of a scalar named inflaton. The perturbations in the inflaton which is the predominant component of the early universe energy density sets the initial condition of the gravitational field perturbation. Thus the initial conditions were generated for cold dark matter, baryons, and every particle and field observed today.

- Big Bang Nucleosynthesis. Several minites after the Big Bang, due to the rapid expansion of the universe, the hot primordial plasma becomes cold enough ($10^7 - 10^9$K) for protons and neutrons to combine into atomic nuclei. Because the expansion rate is high, the time for such nuclear reactions is short. Therefore only very light nuclides like D, ^{3}He, ^{4}He and Li were synthesized during the BBN. The BBN depends sensitively on baryon asymmetry, lepton asymmetry and universe's expansion rate. Since we probe the relic abundance of the above light nuclei by observing the interstellar medium and high-redshift quasar absorption lines, BBN provides unique constraints on the Standard Model beyond-Standard Models, as well as cosmology. [36]

- Recombination. As the universe further expands, the primordial plasma of baryons and photons cools down to the temperature when protons can combine with electrons to form neutral Hydrogen atoms. Because we have much more photons than baryons in the universe (photon/baryon ratio $\eta_{b\gamma} \approx 10^{-9}$), and photons do not interact with each other directly, and the universe after this epoch (around 370,000 yr, redshift $\sim$ 1100) is mostly transparent to the photons. The the cosmic microwave background decoupled from the baryons in this process is almost isotropic on the sky with current temperature 2.7K, with tiny temperature anisotropies of order $\frac{\Delta T}{T} \approx 10^{-5}$. There is rich information in the CMB temperature anisotropy, as it was caused by physics factors including the acoustic oscillation of the baryon-photon plasma before the last scattering, initial gravitational perturbation, baryon masses, silk damping. The CMB anisotropy measured by Planck gives us the tightest constraints on many properties of the universe.

- Reionization. As the earliest stars started to form after the long dark age between the recombination and redshift ~ 20, the universe began to get reionized by the chemical processes in stars and galaxies. This epoch is investigated by observing the high redshift quasar absorption spectrum, and will likely be much better known to us with better observations of the 21 cm signal of the neutral hydrogen surveys in the near future.

- Structure formation. In the late universe, the universe is cool enough that the predominant effect is posed by the gravitational interaction. Under the gravity of dark matter, the perturbative overdensities in the universe start to collapse and to form

halos and structures. Hence the distribution of mass and the galaxies that trace the mass is not homogeneous, but contains statistically inhomogeneous features. Modern cosmology surveys like the Dark Energy Survey (DES) take large-area sky maps of the galaxy positions and shapes, then measure the statistically inhomogeneous features in them. Cosmological models can predict the structure formation features through N-body simulations or (semi-)analytical perturbative solutions. By cross-checking theory and observation, late time structure formation provides us with a lot of information about the universe, for example, the amount and the equation of state of the dark energy.

Throughout the history above, the universe is expanding fueled by its energy density. An illustration summarizing the history of the universe is presented in figure 2.1, taken from chapter 1 of the book [1].

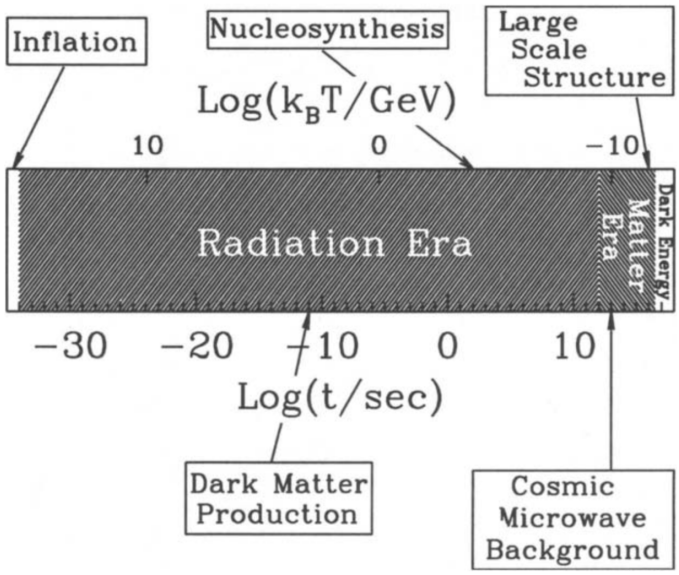

Figure 2.1: The history of the universe. Figure taken from Chapter 1 of [1].

2.2 Background Cosmology – Expansion History

This section mostly referred to the chapter 2 of *Modern Cosmology* (Dodelson 2003), skipping the curved space time treatment and some other mathmatical details, . Throughout this section I assume a flat universe, since curved case is considered an extension of ΛCDM, which we discuss later.

This section adopts natural units:

$$\hbar = c = k_B = 1, \tag{2.1}$$

and the conventional metric signature:

$$(-, +, +, +). \tag{2.2}$$

It has been confirmed by observations that our universe is homogeneous and isotropic at large spatial scales ($L \gtrsim 100$ Mpc), and the background level smooth expansion of such a universe is determined by the composition of the energy content. Specifically, the expansion rate is determined by the fraction and the equation of state of each component that together take up all the energy in this universe. I will start from the fundamental rule for the dynamics of the universe, Einstein's general relativity. General relativity theory was proposed by Einstein in 1915, and it interprets the gravitational interaction as a geometrical curvature. This is fundamental to our modern understanding of gravity. In Euclidean space, the square of distance between two points is given by:

$$ds_E^2 = dx^2 + dy^2 + dz^2. \tag{2.3}$$

Conversely in Minkowski space, which has three dimensions of space and one dimension of time, the distance between two points in spacetime is given by:

$$ds^2 = -dt^2 + dx^2 + dy^2 + dz^2. \tag{2.4}$$

From the simple expression of the above metric, it is easy to imagine that Minkowski spacetime is as "straight and perpendicular" as Euclid space, except that it has one more dimension. Such metric is usually called "flat" because it has no curvature. But just like there exist spherical and more complicated shaped surfaces, our 4D spacetime could also have non-trivial metrics. In general, we write the differential distance squared, and hence the metric of a 4D spacetime, as:

$$ds^2 = \sum_{\mu,\nu=0}^{3} g_{\mu\nu} dx^\mu dx^\nu. \tag{2.5}$$

The $\sum$ sign in front of the expression is usually not explicitly written out, and by convention the repetition of a dummy index means summing over its possible values. For Greek letters like μ and ν, the range is often 0(time), 1, 2, 3(space). Since classically dx^μ are commutative, the metric $g_{\mu\nu}$ is commonly written as a symmetric rank four matrix, with signature

$(-,+,+,+)$ as mentioned at the beginning of this section. Another completely equivalent convention is $(+,-,-,-)$. The Minkowski metric in equation 2.4 is a special case:

$$g_{\mu\nu} = \eta_{\mu\nu} = \begin{pmatrix} -1 & 0 & 0 & 0 \\ 0 & 1 & 0 & 0 \\ 0 & 0 & 1 & 0 \\ 0 & 0 & 0 & 1 \end{pmatrix}. \tag{2.6}$$

The general principle of relativity states that the laws of fundamental physics are the same in all systems of reference. Formally, it means that under the general coordinate transformation:

$$dx^\mu = \frac{\partial x^\mu}{\partial x'^\rho} dx'^\rho. \tag{2.7}$$

The corresponding metric transformation keeps the differential distance unchanged:

$$ds^2 = g_{\mu\nu} dx^\mu dx^\nu = g_{\mu\nu} \frac{\partial x^\mu}{\partial x'^\rho} \frac{\partial x^\nu}{\partial x'^\sigma} dx'^\rho dx'^\sigma; \tag{2.8}$$

$$g'_{\rho\sigma} = g_{\mu\nu} \frac{\partial x^\mu}{\partial x'^\rho} \frac{\partial x^\nu}{\partial x'^\sigma}, \tag{2.9}$$

so that the form of physics equations does not change.

Skipping the splendidly smart processes through which Einstein (and his competitor Hilbert) reached their conclusions, I present the Einstein equations here. So far these are the minimal equations that satisfy the general principle of relativity.

$$G_{\mu\nu} = R_{\mu\nu} - \frac{1}{2} g_{\mu\nu} R = 8\pi G T_{\mu\nu}, \tag{2.10}$$

where $R_{\mu\nu}$ is the Ricci curvature tensor, $R = g^{\mu\nu} R_{\mu\nu}$ is the Ricci scalar, and $T_{\mu\nu}$ is the energy-momentum tensor of the matter field.

Einstein equations connect the geometry of the spacetime on the left to the matter energy and momentum on the right side of the equations 2.10. Formally, in terms of the metric and matter field Lagrangian, we can express these tensors as:

$$\Gamma^\mu_{\nu\rho} = \frac{1}{2} g^{\mu\sigma} (\partial_\nu g_{\sigma\rho} + \partial_\rho g_{\sigma\nu} - \partial_\sigma g_{\nu\rho}), \tag{2.11}$$

$$R_{\mu\nu} = \partial_\rho \Gamma^\rho_{\mu\nu} - \partial_\mu \Gamma^\rho_{\rho\nu} + \Gamma^\rho_{\rho\sigma} \Gamma^\sigma_{\mu\nu} - \Gamma^\rho_{\mu\sigma} \Gamma^\sigma_{\rho\nu}, \tag{2.12}$$

$$T^{\mu\nu} = \frac{-2}{\sqrt{-g}} \frac{\delta(\sqrt{-g}\mathcal{L}_M)}{\delta g^{\mu\nu}} = -2 \frac{\delta \mathcal{L}_M}{\delta g^{\mu\nu}} + g_{\mu\nu} \mathcal{L}_M. \tag{2.13}$$

Here $g = \det(g_{\mu\nu})$, and $\Gamma^\mu_{\nu\rho}$ are called Christoffel symbols. We can raise and lower the

contravariant and covariant indices by multiplying by the metric tensor:

$$X^{\mu\cdots} = g^{\mu\nu} X_{\nu}^{\cdots}, \tag{2.14}$$

$$X_{\mu\cdots} = g_{\mu\nu} X^{\nu}_{\cdots}, \tag{2.15}$$

where contravariant metric is defined by:

$$g_{\mu\nu} g^{\nu\rho} = \delta^{\rho}_{\mu}. \tag{2.16}$$

The Christoffel symbols play an important role in the covariant derivative. Under coordinate transformation equation 2.7, unlike normal partial derivative, the covariant derivative ∇_μ on tensors transform covariantly with the coordinate system.

$$\nabla_\mu \phi = \partial_\mu \phi, \tag{2.17}$$

$$\nabla_\rho T^\mu{}_\nu = \partial_\rho T^\mu{}_\nu + \Gamma^\mu_{\rho\sigma} T^\sigma{}_\nu - \Gamma^\sigma_{\rho\nu} T^\mu{}_\sigma. \tag{2.18}$$

Before going into the background level solution of the Einstein equation 2.10, which is the purpose of this section, there are some comments that I would like to add. The purpose of this dissertation is to investigate the standard and the extended cosmological models. The Einstein equation 2.10 could be derived by applying the principle of least action on Einstein-Hilbert action:

$$S = \frac{1}{16\pi} \int R\sqrt{-g} dx^4 + S_M, \tag{2.19}$$

where S_M is the action of the matter field. Again, we see the elegance and the simplicity of Einstein's general relativity here – it implies that if the curved spacetime itself has Lagrangian energy, this potential energy is simply the Ricci curvature of the spacetime R. I personally think we do not need to spoil this simplicity by resorting to modified gravity theories. But on the other hand, the lack of a first principle derivation for R gravity action (in classical general relativity) points to another way to state the same issue: Einstein's general relativity is far from the "general theory" of gravity. By assuming higher order terms of the gravitational action as the low-energy effective field theory of certain high-energy complete quantum gravity, or embedding our 4D gravity in higher dimensional space gravitational theory, we could admit more complicated expressions of the gravitational action that involve $R^2, \nabla^2 R$, etc. Each of these terms is motivated by a well-established formal theory, and under the principle of least action leads to a variant of the Einstein equations 2.10. We will see how these modified gravity theories as a popular subset of the extended cosmology could be constrained by the cosmological observations.

We now return to the smooth background level solution of Einstein equations in our homogeneous and isotropic "vanilla" universe. The generic time-dependent metric that satisfies the homogeneous and isotropic conditions is the FLRW metric developed by Alexander Friedmann, Georges Lemaître, Howard P. Robertson and Arthur Geoffrey Walker in 1920s:

$$ds^2 = -c^2 d\tau^2 = -c^2 dt^2 + a(t)^2 d\Sigma^2. \tag{2.20}$$

Here although $c = 1$ in the natural units, I write it out to distinguish space and time coordinates. $d\Sigma^2$ is in positive, zero, or negative uniform curvature 3-dimensional space. In hyperspherical coordinates,

$$d\Sigma^2 = \begin{cases} dr^2 + \sin^2(r) d\Omega^2, & k = +1, \text{elliptical space} \\ dr^2 + r^2 d\Omega^2, & k = 0, \text{flat space} \\ dr^2 + \sinh^2(r) d\Omega^2, & k = -1, \text{hyperbolic space} \end{cases} \tag{2.21}$$

In ΛCDM cosmology, we assume a flat universe. Thus in Cartesian coordinate system, the metric of such a homogeneous, isotropic, time-dependent universe is:

$$g_{\mu\nu} = \begin{pmatrix} -1 & 0 & 0 & 0 \\ 0 & a(t)^2 & 0 & 0 \\ 0 & 0 & a(t)^2 & 0 \\ 0 & 0 & 0 & a(t)^2 \end{pmatrix}. \tag{2.22}$$

We call $a(t)$ the scale factor of the universe. The physical meaning of a is not difficult to see: if two points are separated by distance x at time t_0, then they will be separated by distance $a(t_1)x/a(t_0)$ at t_1. The most convenient convention is to set our current time scale factor $a_0 = 1$.

As we will see in the following paragraphs, Einstein equations solution $a(t)$ tell us that in a flat universe, as long as we have an average positive energy density, our universe will keep expanding forever. Namely, $\dot{a} = da/dt$ is always positive given a positive initial value.

Meanwhile on the right hand side of the Einstein equations, at the background level, we have a perfect isotropic fluid in the universe:

$$T^{\mu}{}_{\nu} = \begin{pmatrix} -\rho & 0 & 0 & 0 \\ 0 & p & 0 & 0 \\ 0 & 0 & p & 0 \\ 0 & 0 & 0 & p \end{pmatrix}, \tag{2.23}$$

where ρ is the energy density of the fluid, and p is the pressure.

Now we substitute the flat FLRW metric and perfect-fluid energy-momentum tensor into the Einstein equations. The time-time and space-space components give us two equations:

$$\left(\frac{\dot{a}}{a}\right)^2 = \frac{8\pi G}{3}\rho \qquad (\mu = 0, \nu = 0), \tag{2.24}$$

$$\frac{\ddot{a}}{a} = -\frac{4\pi G}{3}(3p + \rho) \qquad (\mu = i, \nu = i). \tag{2.25}$$

The quantity $\frac{\dot{a}}{a}$ tells us the expansion rate of the universe, and we call it the Hubble parameter or the Hubble rate, $H \equiv \frac{\dot{a}}{a}$. The Hubble parameter fully describes the expansion history. Equation 2.24 relates H to ρ:

$$H = \frac{\dot{a}}{a} = H_0\sqrt{\frac{\rho}{\rho_c}}, \tag{2.26}$$

where the fiducial $H_0 \approx 70$ km/s/Mpc is the present-day value of the Hubble parameter called Hubble constant, and ρ_c is the critical density, the current total energy density of the universe when it is flat. These two parameters are introduced as a physically meaningful way to specify the boundary condition of H rate solution at present time, when the scale factor is set to be $a = 1$. H_0 and ρ_c are connected by the Friedmann equation:

$$\rho_c = \frac{3H_0^2}{8\pi G}. \tag{2.27}$$

The physics in equation 2.26 is powerful, showing that the background level geometry of the expanding universe is determined by the equation of state of the perfect isotropic fluid. To see how it works, we need the continuity equation of the energy-momentum tensor and the equation of state of a perfect isotropic fluid:

$$\nabla_\mu T^\mu{}_\nu = 0, \tag{2.28}$$

$$p = w\rho. \tag{2.29}$$

In FLRW metric equation 2.22, equation 2.28 becomes (only ν=0 component is non-trivial):

$$\dot{\rho} + 3H(\rho + p) = \dot{\rho} + 3H(1 + w)\rho = 0. \tag{2.30}$$

Integrating the above equation gives us, for $w = $ const.:

$$\rho \propto a^{-3(1+w)}. \tag{2.31}$$

For a perfect fluid that obeys continuity equation, its energy density decreases with the expansion of the universe. The following statement is intuitive: consider our universe as a spotted balloon being blown up, as its surface area gets larger, the spots are separated more sparsely. However, we will see later in this section that when $w \leq -1$, i.e. the fluid has negative pressure, the opposite sens of scaling can happen.

Because the derivation of the above relationship used only the continuity equation, which is obeyed by each non-interacting species, in a universe with various components we more generally have:

$$\rho_i \propto a^{-3(1+w_i)}, \tag{2.32}$$

$$H^2 = \frac{8\pi G}{3} \sum_i \rho_i. \tag{2.33}$$

Dividing the above equation 2.33 by equation 2.27, we get:

$$\frac{H^2}{H_0^2} = \sum_i \Omega_i a^{-3(1+w_i)}, \tag{2.34}$$

where the density parameter Ω_i is defined as $\Omega_i = \frac{\rho_i(a=1)}{\rho_c}$, the present-day fraction of the energy density of a species to the total critical energy density. In a cold and nonreactive universe, by measuring the composition of the current universe and learning their equations of state, we can reconstruct the expansion history $H(a) = \dot{a}/a$ of the universe. Furthermore, the scale factor could be fairly easily determined by observing the redshift of a star or galactic spectrum at that epoch:

$$\begin{aligned} z &\equiv \frac{\lambda_{\text{obs}} - \lambda_{\text{emit}}}{\lambda_{\text{emit}}} \\ &= \frac{a(t_{\text{obs}})\lambda_{\text{cov}} - a(t_{\text{emit}})\lambda_{\text{cov}}}{a(t_{\text{emit}})\lambda_{\text{cov}}} \\ &= \frac{1-a}{a}, \end{aligned} \tag{2.35}$$

where λ_{cov} is the wavelength in the comoving coordinates in which the distance between two points stays the same if there is no dynamics (constant distance ignoring the expansion). The last equality above used the condition that the current, or observer scale factor $a_0 = 1$, and I denoted a_{emit} as a.

Clearly, $a = 1/(1+z)$ from inverting the equation 2.35. By integrating $H(a) = \frac{1}{a}\frac{da}{dt}$ from $a = 1$ to $a = 1/(1+z)$, one can get the distance to an astrophysical event, of which the

signal is sent to us through the light:

$$\chi = \int_{t(a)}^{t(a=1)} \frac{dt'}{a(t')} = \int_a^1 \frac{da'}{a'^2 H(a')}, \qquad \text{(Comoving distance)}. \tag{2.36}$$

$$d_A = a\chi, \qquad \text{(Angular} - \text{diameter distance)}. \tag{2.37}$$

$$d_L = \frac{\chi}{a}, \qquad \text{(Luminosity distance)}. \tag{2.38}$$

These distances are used in different occasions. The comoving distance, which is fixed between two points throughout the expansion of the universe, is useful when we want to describe the dynamics of a system ignoring the physical scale change due to the expansion. The angular-diameter distance d_A is used when we observe angles to infer distances, with the relationship $\theta = \frac{l}{d_A}$ where l is the physical size of a distant object. Lastly, given an astrophysical source with luminosity L, the luminosity distance is used when we infer distances from measurements of the fluxes, with the relationship $F = \frac{L}{4\pi d_L^2}$.

Now we come back to the practical and realistic case study of equation 2.34, the standard ΛCDM cosmology. In ΛCDM, when categorized in terms of the equation of state in equilibrium, the universe consists three types of energy: the non-relativistic matter, the relativistic radiation, and the dark energy. The matter has no pressure, the radiation has $p = \rho/3$, and the dark energy, often interpreted as a result of the cosmological constant, has negative pressure $p = -\rho$. Thus we have:

$$w_m = 0, \qquad \rho_m \propto a^{-3}. \tag{2.39}$$

$$w_r = \frac{1}{3}, \qquad \rho_r \propto a^{-4}. \tag{2.40}$$

$$w_\Lambda = -1, \qquad \rho_\Lambda = \text{const.}. \tag{2.41}$$

Furthermore, in a flat ΛCDM universe,

$$\frac{H}{H_0} = \sqrt{\Omega_m a^{-3} + \Omega_r a^{-4} + \Omega_\Lambda}, \qquad \text{where } \Omega_\Lambda = 1 - \Omega_m - \Omega_r. \tag{2.42}$$

Before I expand what exactly makes up the matter, radiation, and dark energy in the standard cosmology, I would like to first demonstrate how equation 2.42 determines the expansion history. Because $H > 0$, our universe is expanding given its initial conditions, namely the scale factor a is monotonically increasing. Mathematically the terms a^{-4}, a^{-3} and a^0 decrease at a descending rate as a increases. Thus we can make the prediction that the relative abundance of matter increases against radiation with time, and the relative abundance of dark energy increases against dark matter. Indeed, since the Big Bang our

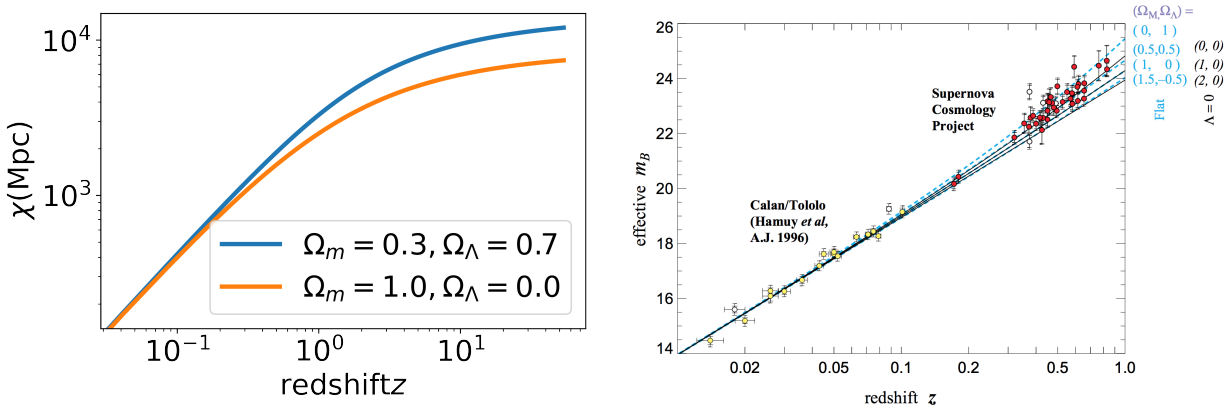

Figure 2.2: Left panel: the comoving distance as a function of redshift, in dark matter + dark energy universe, and in dark matter only universe. Right panel: Type Ia supernova effective magnitude, which is a logarithmic measure of with the luminosity distance, against redshift. This panel is taken from the reference [2].

universe has gone through radiation dominated, matter dominated, and dark energy dominated epoch in that order. The effect of different combinations of the density parameters for dark matter and dark energy are illustrated in figure 2.2.

The matter and radiation components are easy to intuitively understand. The matter includes Standard Model matter particles and dark matter, which are non-relativistic and do not interact on large scales as the universe expands. They have zero pressure. Among them, the Standard Model particles mainly consists of familiar baryons like protons and neutrons, and the leptons like electrons. In the Standard Model, neutrinos are completely massless, so they contribute to the radiation energy density in the following paragraphs.

The dark matter which, prior to 1990s had been widely accepted as a major bulk of energy density in our universe today, in ΛCDM is claimed to be completely cold. In ΛCDM, dark matter does not self-interact or interact with the Standard Model matter at a detectable level. The only interaction dark matter feels is the gravity, hence it is only through gravity that we can observe it. As early as in 1933, Fritz Zwicky inferred the extra mass in the Coma cluster of galaxies by noticing the mismatch between the galaxies' motion and the mass estimation through brightness [37]. Vera Rubin, Kent Ford and Ken Freeman's work in 1970s provided strong evidence of dark mass by measuring the galaxy rotation curves [38]. If, you are still skeptical and think that these observation effects can be due to stronger gravity at galaxy scales or are pure observational caveats (like I did in my first year of PhD), let me remind you of equation 2.42 and figure 2.2. Probes like Supernovae, CMB, and BAO, which sensitive to the geometry of the expanding universe, tightly constrain the amount of dark matter and dark energy in our universe to reproduce the observed Hubble diagram; See figure 2.2.

The radiation density decays $\propto a^{-4}$, and becomes a less important component in terms of the expansion history around $z \sim 3500$, after the matter-radiation density equality. The radiation usually refers to the photon plus the massless Standard Model neutrinos. They have relativistic dynamics and pressure $p_r = 1/3\rho_r$.

Dark energy is a less intuitive form of energy in the universe proposed to explain its accelerating expansion. Equation 2.25 tells us that if we only have fluid with $p > -\frac{1}{3}\rho$ in our universe, the expansion is always decelerating. However, since 1990s, observational evidences have indicated an accelerating expansion of the universe [39,40]. One evidence is represented by the Supernovae Hubble diagram as shown in the right panel of figure 2.2. Dark energy, which has the equation of state $p \approx -\rho$, provides the necessary negative-pressure component to explain the acceleration. In the limit $p = -\rho$, dark energy constant energy density, and does not dilute as the space expands, as if the energy is attached to the space itself. Dark energy can be represented by an extra constant term in the Einstein equation:

$$R_{\mu\nu} - \frac{1}{2}g_{\mu\nu}R + \Lambda g_{\mu\nu} = 8\pi G T_{\mu\nu}, \tag{2.43}$$

$$\rho_\Lambda = \frac{\Lambda}{8\pi G}, \tag{2.44}$$

where Λ is usually called the cosmological constant. In quantum field theory, the cosmological constant is predicted as the vacuum energy of the quantum fluctuations, but the theory prediction is $\mathcal{O}(100)$ orders of magnitudes off from the cosmological measurements.

So far, we still know little about the dark energy, and there is no evidence to prove or disprove the cosmological-constant hypothesis, which suggests dark energy is the phenomenological name of a cosmological constant of some kind. The only things we can assert about the dark energy are that it has negative pressure, $w \sim -O(1)$, and it takes up the majority of energy density in our current universe. A variety of the extended ΛCDM models contributed to explain Λ by modified gravity, dark sectors or other approaches.

2.3 Perturbative Cosmology – Photon Anisotropy and Matter Inhomogeneity Spectra

In the last section, I have presented a picture of the smooth, homogeneous universe undergoing expansion in chemical equilibrium quietly. But we know there is much more than that happening in our universe. Although it looks homogeneous on large scales, the universe does have non-trivial distribution of galaxies inside dark matter halos, and non-trivial distribution of gas and stars inside galaxies. The cosmic microwave background (CMB) is almost

isotropic over the whole celestial sphere at temperature 2.725K, but when measured with high precision maps, CMB has anisotropic fluctuation with the magnitude $\Delta T \sim 20\mu$K. The distributions of perturbation fields provide us with rich information about cosmology, as their dynamics imprinted the interactions that have happened in the expansion history of the universe.

In this section, I will focus on the inhomogeneity in the matter perturbation field and the anisotropy in the photon temperature field, explain their definitions, and schematically present how they were predicted by theory (ΛCDM). This last point is the most important goal of this section. The perturbation theory is a huge topic that could be a full thesis in its own right, so this chapter is kept basic and conceptual in the context of this theory+data thesis.

2.3.1 Boltzmann Equations

This section referred to the formalism in reference [41] and [1].

The volume averaged dynamics of the matter and radiation field is determined by the Einstein equation 2.10 and the energy-momentum current between particle species:

$$\nabla_\mu T^\mu{}_\nu = Q_\nu. \tag{2.45}$$

It is obvious that the continuity equation 2.28 is the special case when $Q_\nu = 0$. The total energy-momentum tensor of the fluid in the universe is conserved, and the energy-momentum tensor is also conserved for each decoupled species. However, we know that the departure from equilibrium happens as the universe cools down, and it results in several drastically changing epochs in the universe like the nucleosynthesis and recombination. The energy and momentum flow from one species to another will naturally cause the transition in the averaged number density and in the phase space distribution of the number density of particle species. Other than this effect, in the universe in equilibrium, local collisions can still happen and cause changes in the phase space number distribution.

In practice, in order to establish the anisotropy and inhomogeneity in the universe, we need to solve the phase space distribution of particles determined by the Boltzmann equations. The physical meaning of Boltzmann equation is that the number density of a particle species in the phase space changes as particles are created or destroyed by the collision processes. Suppose the phase space distribution of a particle species is described by $f(x^i, p_j, \tau)$:

$$dN = f(x^i, p_j, \tau) dx^1 dx^2 dx^3 dp_1 dp_2 dp_3, \tag{2.46}$$

where x^i, p_j are the comoving coordinates and comoving conjugate momenta, and $d\tau = \frac{dt}{a(t)}$ is the conformal time. The general energy-momentum tensor $T_{\mu\nu}$ takes the form:

$$T_{\mu\nu} = \int dp_1 dp_2 dp_3 (-g)^{-1/2} \frac{p_\mu p_\nu}{p^0} f(x^i, p_j, \tau), \tag{2.47}$$

where, recall, $g = \det(g_{\mu\nu})$. So the time component of the equation 2.45 should be consistent with the momentum integrated Boltzmann equation. In terms of the space coordinates and the momenta, the Boltzmann equation is:

$$\frac{df}{d\tau} = \frac{\partial f}{\partial \tau} + \frac{\partial f}{\partial x^i}\frac{dx^i}{d\tau} + \frac{\partial f}{\partial p_j}\frac{dp_j}{d\tau} = C[f]. \tag{2.48}$$

The right hand side of the equation is the collision term, which is a functional of the phase space distribution function. This term is determined by the Standard Model (or any other non-gravitational) interactions felt by the particle species. For cold dark matter, which only interacts through gravity, this term is zero. However, the left hand side of the Boltzmann equation makes things not as simple as they seem. The momentum derivative $\frac{dp_j}{d\tau}$ is determined by the geodesic equation of the particle, and it needs input from the local spacetime metric perturbation. Thus the complete set of equations that need to be solved includes the Boltzmann Equation 2.48 for each species in the universe, and the Einstein equation 2.10 perturbatively expanded in coordinates. In synchronous gauge, where g_{00}, g_{0i} are unperturbed by definition, we can write the metric perturbation as h_{ij}:

$$ds^2 = -dt^2 + a^2(t)(\delta_{ij} + h_{ij})dx^i dx^j. \tag{2.49}$$

Let us take a step back to look at the system of equations at hand. The particle distribution perturbative variables are defined in the phase space x^i, p_j and the metric perturbative variables in the configuration space x^i. When considering the total fluid in the universe, the degrees of freedom include 10 symmetric energy-momentum tensor components plus 10 symmetric spacetime metric components. Einstein equations reduce 10 degrees of freedom, and space-time gauge fix further 4 degrees of freedom, leaving 6 free variables. Without losing generality, we could say these degrees of freedom are specified by the fluid features, for example the equation of state factor w and its anisotropic stress.

Because we are not concerned about the local momentum of the particles in cosmology, when processing Boltzmann and Einstein equations we integrate the magnitude of momentum out. As for the coordinate space, we usually make Fourier transformation and express everything in the k-space where the equations are easier to manipulate as $\nabla_i \to ik_i$. For

non-relativistic species, things are simple and we set $p_j = 0$ everywhere. Then we are left with a solution of the Boltzmann equation about the inhomogeneity of the matter distribution in k-space. For relativistic species, the anisotropy of the momentum $\hat{k} \cdot \hat{p}$ becomes important, and the Boltzmann equation needs to be solved in terms of a series of hierarchical moments of the phase space distribution function. These moments, as we shall see in the next subsection, corresponds to the CMB anisotropy spectrum.

The descriptive summary above should be sufficient for me to proceed into the observational cosmology with the CMB temperature and polarization spectrum and the matter power spectrum in the next two subsections. I will leave the mathematical details about the linear perturbative expansion and phase space Fourier transformations of the Boltzmann and Einstein equations from this point on to reference [41]. In practice, cosmologists numerically solve the Boltzmann and Einstein equations using the codes developed in recent decades, like CAMB [42] and CLASS [43]. These codes are optimized in terms of efficiency and precision. Most importantly, cosmologists can modify the codes directly related to the physical equations, to tailor these Boltzmann solvers for the extended ΛCDM models. All one needs to do is to derive the Boltzmann and Einstein equations in the notations adopted by the codes' original authors, then incorporate these modifications in the codes.

2.3.2 Photon Field Anisotropy

In the last subsection, I schematically introduced how to theoretically derive the perturbation equations in cosmology. This subsection and the next discuss about the spectra of the perturbation fields.

The cosmic microwave background, of photons that travel to us from the last scattering surface is on average, remarkably uniform. We can measure the tiny polarization and temperature anisotropy with the current instruments. Here I will focus on the temperature anisotropy to keep things basic in this subsection. The two point correlation function of the temperature fluctuation can be defined as:

$$\Theta(\hat{n}) \equiv \frac{\Delta T(\hat{n})}{\bar{T}}, \tag{2.50}$$

$$C(\theta) = \langle \Theta(\hat{n}_1)\Theta(\hat{n}_2) \rangle, \tag{2.51}$$

where $\hat{n}$ is the unit vector pointing to the observation direction, and $\cos(\theta) = \hat{n}_1 \cdot \hat{n}_2$ for two

points on the sky. We can expand $\Theta(\hat{n})$ into the spherical harmonics:

$$\Theta(\hat{n}) = \sum_{\ell=0}^{\infty} \sum_{m=-\ell}^{m=\ell} a_{\ell m} Y_{\ell m}(\hat{n}), \tag{2.52}$$

where $a_{\ell m}$ are complex coefficients, and $Y_{\ell m}$ are the Bessel functions of the second kind. Then we define the angular power spectrum of the temperature anisotropy, as:

$$\langle a_{\ell m} a^*_{\ell' m'} \rangle = C_\ell \delta_{\ell \ell'} \delta_{m m'}, \tag{2.53}$$

where δ_{ij} is the Kronecker delta, and the bracket denotes averaging over the perturbation field being drawn from the inflation. Substituting equations 2.52, 2.52 into equation 2.51, we get:

$$C(\theta) = \frac{1}{4\pi} \sum_{\ell=0}^{\infty} (2\ell + 1) C_\ell P_\ell(\cos(\theta)), \tag{2.54}$$

where $P_\ell(\cos(\theta))$ are the Legendre polynomials. The angular power spectrum of the photon temperature anisotropy C_ℓ can be theoretically predicted by solving the Boltzmann equation of the photons. In general, the photons obey the unperturbed Bose-Einstein distribution f_0:

$$f_0(p, T) = \frac{g_s}{h^3} \frac{1}{e^{p/k_B T} - 1}, \tag{2.55}$$

where g_s is the number of spin degrees of freedom. When there is fluctuation in the temperature, then

$$f(x^i, p, n_j, \tau) = f_0 \left(\frac{p}{1 + \Theta(x^i, n_j, \tau)}, \bar{T} \right), \tag{2.56}$$

where $\bar{T}$ is the background average temperature.Here we neglected the relatively rare distortion of the frequency spectrum that might be introduced by the electron-photon scattering after recombination, assuming $\Theta(x^i, n_j, \tau)$ is independent on p. Thus we can make a linear expansion to relate phase space distribution function solution to the temperature fluctuation. Because the velocity of us observers is too slow compared to photons, the coordinate conjugate k-space should be averaged out to obtain the C_ℓ angular power spectrum that we measure.

2.3.3 Matter Field Inhomogeneity

Unlike the relativistically moving photons, the cold or baryonic matter phase space distribution is almost independent of the momentum magnitude and orientation. Instead, its density depends on the space coordinate conjugate $\vec{k}$, thus the inhomogeneity in the space is of more

interest. At a given time, the dimensionless overdensity of matter field is defined as:

$$\delta_m(\vec{x}) = \frac{\rho_m(\vec{x})}{\bar{\rho_m}}, \tag{2.57}$$

where $\rho_m(\vec{x})$ is the matter density field and $\bar{\rho}_m$ is the background average matter density. The two point correlation function of the over density is:

$$\xi_m(\vec{x}, \vec{x}') \equiv \langle \delta_m(\vec{x}) \delta_m(\vec{x}') \rangle. \tag{2.58}$$

We can make the Fourier tranform to get the matter power spectrum:

$$\delta_m(\vec{k}) \equiv \int \delta_m(\vec{x}) e^{i\vec{k}\cdot\vec{x}} d^3x, \tag{2.59}$$

$$P_m(\vec{k}, \vec{k}') \equiv \frac{1}{(2\pi)^3} \langle \delta_m(\vec{k}) \delta_m(\vec{k}') \rangle. \tag{2.60}$$

Since our universe is isotropic and homogeneous,

$$P_m(\vec{k}, \vec{k}') = \delta_D(\vec{k} - \vec{k}') P_m(k), \tag{2.61}$$

so that $P(k)$ only depends on magnitude of vector $\vec{k}$. Here $\delta_D(\vec{k})$ is the Dirac-delta function. Notice that $P(k)$ has dimension $\sim k^{-3}$, and the dimensionless logarithmic band power could be useful:

$$\Delta^2_m(k) \equiv \frac{k^3 P_m(k)}{2\pi^2}. \tag{2.62}$$

For a particle with constant mass, its overdensity $\delta(k)$ is proportional to phase space distribution $f(k)$. Similar to the case of photons, in practice we use the Boltzmann codes to numerically solve the matter fluctuation and translate them into the matter power spectrum. However, I would like to give some approximated analytical solutions which are much less accurate than the Boltzmann codes but still capture key features of the large scale structure growth. Schematically, the matter power spectrum could be broken down into three components: the primordial power, the transfer function and the growth function.

$$P_m(k, a) = P^0_m(k) \times T(k) \times \left(\frac{D(a)}{D(1)} \right)^2, \tag{2.63}$$

where $P^0_m(k)$ is the primordial matter power spectrum determined at the exit of inflation. Here $T(k)$ transfer function describes the effect resulted from different horizon-crossing time for the modes. The modes that enter the horizon early, namely $k > aH$ before the matter-radiation equality evolves very differently from the modes that enter after matter-radiation

equality. The pressure of the radiation significantly slows down the structure growth. And lastly, $D(a)$ is defined as:

$$D(a) \equiv \frac{\delta_m(a)}{\delta_m(a_*)}, \tag{2.64}$$

where a_* is a late enough time when every mode is in the horizon and the growth of the over-density becomes scale independent. In such epoch, where $k\tau >> 1$, we can simplify the Boltzmann and Einstein equations to get a linear growth equation:

$$\frac{d^2\delta_m}{da^2} + \left(\frac{d\ln(H)}{da} + \frac{3}{a}\right)\frac{d\delta_m}{da} - \frac{3\Omega_m H_0^2}{2a^5 H^2}\delta_m = 0. \tag{2.65}$$

We will see in the next chapter how $P(k)$ is related to the direct observations in practice. Unlike the clean CMB temperature C_ℓ that we can in principle measure out of a full sky map of the cosmic microwave background photon, the theory predicted matter power spectrum needs projection onto 2D planes (or mapping into the redshift space) to be compared with the real world observations.

2.4 Summary and Extensions to ΛCDM Model

In this chapter, I tried to present a full picture of the framework of the modern cosmology theory, taking ΛCDM model as an example. Starting from the theory of gravity, a cosmology model serves to draw the expansion and structure formation history on a homogeneous and isotropic spacetime canvas. I presented the timeline for the drastic (non-equilibrium) major events that happened since the Big Bang. Skipping more involved mathematical details, I schematically explained how the theories give quantitative predictions on the background and perturbative level. All these predictions are in an amazing agreement with our observations so far, and that is why ΛCDM is the most successful cosmological model today.

However, as I implied in the flow of ΛCDM story above, there are plenty of assumptions for us to challenge and plenty of room for us to propose extensions to the vanilla-ΛCDM model. We are doing this for a reason – despite the success of ΛCDM, some anomalies that cannot be fully explained by ΛCDM have started to show up as the precision of observations rapidly improves. For example, the $3\sigma - 5\sigma$ discrepancy between the early universe and late universe measurement of the Hubble constant has stimulated a hot debate in the community [10, 44, 45]. Moreover, the Hubble constant measured by observing the redshift and the distance to the nearby Supernovae takes the value (73.48 ± 1.66)km s^{-1} Mpc^{-1} [46], while the model-fitting to the ΛCDM model of the CMB temperature anisotropy spectrum constrains the Hubble constant to be (67.27 ± 0.60)km s^{-1} Mpc^{-1} [10]. The possibility

of non-cosmological systematic error causing the Hubble tension still exists. But with the growing number of independent early and late universe measurements of the Hubble constant confirming the persistence of the tension (see a compilation of the current status in [44]), the investigation on a possible theoretical resolution seems more necessary than ever. Although not as statistically prominent as the Hubble tension, other surprises like the lower amplitude of the matter fluctuation in cosmic shear surveys [7] and enhanced global 21 cm signal absorption [47] appeared and are waiting for further confirmation [48].

Most of the extended cosmological models to ΛCDM model include one or more of the following theoretical elements:

1. Non-default background metric. For example, a non-flat universe with constant positive curvature (de Sitter space) or negative curvature (anti-de Sitter space) is a very popular extended model. Also under the microscope are the assumptions of the perfect inhomogeneity and isotropy, and the number of space dimensions of our universe.

2. Modified gravity. As briefly mentioned before, the Hilbert-Einstein action, equation 2.19, is the simplest possible form of gravity. Higher order terms could be resulted from an effective field theory of a UV complete theory. These theories alter the Einstein equations.

3. More complicated composition and dynamics of the fluid in the universe. Theorists have introduced new particle species to ΛCDM, and/or changed their equation of motion and interactions. These theories alter the Boltzmann equations.

In this thesis, I present a state-of-art analysis of a phenomenological model where the dark matter converts into the dark radiation. I am also involved deeply in the DES extensions group, where curved spacetime, modified gravity, massive neutrinos and the time-varying equation of state for dark energy are studied with combined cosmological probes. It is not easy to find a model that cures the tensions while keeping the successful features of the ΛCDM. But each time we experiment with a different model, we are one step closer to finding the right handle to pull. Not only are the analysis techniques transferable to new surveys and new models, but also we learn how the universe reacts to the different variations we introduce into it – they are not easy to see through intuitively or even through analytical calculations, given the complexity of the universe itself. This thesis hopefully contributes one piece to the puzzle.

Chapter 3

Large Scale Structure Observables

In the previous chapter, I presented how to predict the matter overdensity inhomogeneity, described by matter power spectrum $P(k)$, starting from the cosmological model. $P(k)$ lives in the 3D wave-number space, while in practice we are only able to measure the angular distribution of the matter field, since all of our observations are performed from the Earth. Hence in this chapter, I will present how we theoretically obtain the angular correlation functions of the mass tracers for a galaxy survey. I will continue in the first half of the next chapter, describing how to fuse theory predictions into a survey likelihood, using DES as the example.

In this section I will start with the strategy of projecting an arbitrary mass tracer to the angular 2D space, then present how it works for the galaxy position and the weak lensing shear case by case. By a mass tracer, I mean a field roughly tracing the mass overdensity defined in equation 2.57, but "dressed" by other physics and systematics, denoted as $\delta(\vec{x})$.

The 2D angular distribution of mass, projected along the radial direction, is given by:

$$\delta(\vec{\theta}) = \int_0^{\chi_\infty} d\chi W(\chi)\delta(\vec{x}(\chi, \vec{\theta})), \tag{3.1}$$

where $\vec{x}$ are the comoving configuration space coordinates, and χ_∞ is the comoving distance at $z \to \infty$. Here the weight function W is normalized to 1:

$$\int_0^{\chi_\infty} d\chi W(\chi) = 1. \tag{3.2}$$

The 2D conjugate to $\vec{\theta}$ is the 2D multipole vector $\vec{l}$:

$$\delta(\vec{l}) = \int d^2\theta e^{-i\vec{l}\cdot\vec{\theta}}\delta(\vec{\theta}), \tag{3.3}$$

and the angular power spectrum then becomes:

$$\begin{aligned} C(l) &= \frac{1}{(2\pi)^2}\int d^2l' \langle \delta(\vec{l})\delta(\vec{l'})\rangle \\ &= \frac{1}{(2\pi)^2}\int d^2l' \int d^2\theta \int d^2\theta' e^{-i(\vec{l}\cdot\vec{\theta}+\vec{l'}\cdot\vec{\theta'})} \\ &\times \int_0^{\chi_\infty} d\chi W(\chi) \int_0^{\chi_\infty} d\chi' W(\chi') \int \frac{d^3k}{(2\pi)^3} P(k) e^{i\vec{k}\cdot[\vec{x}(\chi,\vec{\theta})-\vec{x}'(\chi',\vec{\theta'})]}, \end{aligned} \tag{3.4}$$

where we used the definition of 3D power spectra:

$$\langle \delta(\vec{x})\delta(\vec{x}')\rangle = \int \frac{d^3k}{(2\pi)^3} P(k) e^{i\vec{k}\cdot(\vec{x}-\vec{x}')}. \tag{3.5}$$

The integrals over l', θ, θ' and the two k components along the angular direction, k_1, k_2, are all sample trivial Gaussian or Dirac-delta function integrals, so without losing any generality,

$$C(l) = \int_0^{\chi_\infty} d\chi \frac{W(\chi)}{\chi^2} \int_0^{\chi_\infty} d\chi' W(\chi') \int_{-\infty}^{\infty} \frac{dk_3}{(2\pi)} P\left(\sqrt{k_3^2 + l^2/\chi^2}\right) e^{ik_3[\chi-\chi']}. \tag{3.6}$$

We need to do some approximations to simplify the integral over k_3. Notice that when we deal with small angles, which is usually the case in the galaxy surveys, $l \sim \theta^{-1}$ is large, so $l/\chi >> 1/\chi$. Meanwhile, for the characteristic comoving distances spanned by the weighting function $W(\chi)$, if k_3 is so large that $k_3\chi >> 2\pi$ then the plane wave $e^{ik_3\chi}$ would be very oscillatory. Such mode's peaks and valleys cancel out in the integral over the comoving distance (redshift). Thus only the modes with small $k_3 << 1/\chi << l/\chi$ contribute considerably to small angle correlations, i.e. large l moments. Hence we can carry out the Limber approximation and obtain [49]:

$$C(l) = \int_0^{\chi_\infty} d\chi \frac{W^2(\chi)}{\chi^2} P\left((l+\frac{1}{2})/\chi\right). \tag{3.7}$$

3.1 Galaxy Clustering Two-point Correlation Function

Galaxies tend to form in the gravitational potential wells, hence they trace the overdensity of the matter. We can relate the matter overdensity and the galaxy number overdensity by the galaxy bias:

$$\delta_g(k,z) = b(k,z)\delta_m(k,z). \tag{3.8}$$

In the simplest linear model the galaxy bias $b(k,z)$ is usually assumed to be a constant.

The weight function for a galaxy sample is determined by the angular number density of

the galaxies:

$$W(\chi) = \frac{n_g(z(\chi))}{\int dz n_g(z)} \frac{dz}{d\chi}. \tag{3.9}$$

In tomographic galaxy surveys like DES, we partition galaxy samples into several redshift bins, thus have multiple $n^i(z)$ distributions centered at raising order of redshift. This fact will only change the weight function square $W^2(\chi)$ in equation 3.7 to $W^a(\chi)W^b(\chi)$, where a and b are the indices of the redshift bin. Substituting the weight function for the galaxy clustering and the galaxy overdensity into equation 3.7, the angular moments for the galaxy clustering between two tomographic redshift bins take the form [50]:

$$C_{gg}^{ab}(l) = \int d\chi \frac{q_g^a(\frac{l+1/2}{\chi}, \chi) q_g^b(\frac{l+1/2}{\chi}, \chi)}{\chi^2} P_m\left(\frac{l+1/2}{\chi}, z(\chi)\right), \tag{3.10}$$

$$q_g^a(k, \chi) = b^a(k, z(\chi)) \frac{n_g^a(z(\chi))}{\int dz n_g^i(z)} \frac{dz}{d\chi}. \tag{3.11}$$

And the angular two-point correlation function is [51]:

$$w^{ab}(\theta) = \int \frac{dl}{2\pi} l J_0(l\theta) C_{gg}^{ab}(l), \tag{3.12}$$

where $J_0(l\theta)$ is the zeroth order Bessel function of the first kind.

3.2 Weak Lensing Shear Two-point Correlation Functions

In this section I will introduce the weak lensing shear angular spectrum. It will be a longer and more complicated journey than the previous section on galaxy clustering, as we need to start from the physics of weak lensing.

In general relativity, gravitational force is equivalent to the curved spacetime. In another word, gravity bends light. The matter overdensity in the universe correlates with the fluctuation of the gravitational potential, and the scalar perturbed metric could be written as:

$$ds^2 = (-1 - 2\Psi(x))dt^2 + a^2(t)(1 + 2\Phi(x))d\vec{x}^2, \tag{3.13}$$

where x are 4D spacetime coordinates, $\vec{x}$ are 3D space coordinates. Furthermore, in the late universe dominated by matter, we do not have anisotropic stress and the Einstein equation tells us $\Psi = -\Phi$.

We want to know how the light that traveled to us from a distant source is bent by the

gravitational fluctuations, and how the image is distorted. More quantitatively, supposing a light source is located at $\vec{\theta}_S$, and is observed to be at $\vec{\theta}_O$, we can quantify the weak lensing effect by:

$$A_{ij} \equiv \frac{\partial \theta_S^i}{\partial \theta_O^j}. \tag{3.14}$$

The following derivations assumes a small deviation angle and small gravitational fluctuation. The space coordinates in the frame aligned with the line of sight can be written as $(\chi\theta^1, \chi\theta^2, \chi)$. The geodesic equation is:

$$\frac{d^2x^i}{d\lambda^2} = -\Gamma^i_{\mu\nu}\frac{dx^\mu}{d\lambda}\frac{dx^\nu}{d\lambda}. \tag{3.15}$$

We can simplify the transverse geodesic equation to the following form given the perturbed metric in equation 3.13:

$$\frac{d^2}{d\chi^2}\left(\chi\theta^i\right) = 2\Phi_{,i}. \tag{3.16}$$

Using the boundary condition that $\theta^i(\chi) = \theta_S^i$ and $\theta^i(0) = \theta_O^i$, we obtain from integrating the transverse geodesic equation:

$$\theta_S^i = \theta_O^i + 2\int_0^\chi d\chi' \Phi_{,i}(\vec{x}(\chi'))\left(1 - \frac{\chi'}{\chi}\right). \tag{3.17}$$

We are going to substitute this solution to equation 3.14. In the integral term, the only dependence on θ_O^i comes from $\vec{x}$ in $\Phi_{,i}(\vec{x}(\chi'))$, and because the deviation angle is small, we can adopt the approximation $\frac{\partial\Phi_{,i}(\vec{x}(\chi'))}{\partial\theta_O^j} = \Phi_{,ij}(\vec{x}(\chi'))\chi'$. Thus we get:

$$A_{ij} - \delta_{ij} = 2\int_0^\chi d\chi' \Phi_{,ij}(\vec{x}(\chi'))\chi'\left(1 - \frac{\chi'}{\chi}\right) = \begin{pmatrix} -\kappa - \gamma_1 & -\gamma_2 \\ -\gamma_2 & -\kappa + \gamma_1 \end{pmatrix}. \tag{3.18}$$

In the parametrization of the symmetric matrix $A_{ij} - \delta_{ij}$ introduced by the second equality, parameter κ is called the convergence, describing the magnification of the lensed image, and γ_1, γ_2 are the two components of the shear, describing the distortion of the lensed image.

The derivations so far are for a single source. When we have a number density distribution of the galaxies, to obtain the convergence κ and the distortion shear we do the radial integration over the $n(z)$ galaxy sample:

$$\psi_{ij} = 2\int_0^{\chi_\infty} d\chi \frac{n_\kappa(z(\chi))}{\int dz n_\kappa(z)}\frac{dz}{d\chi}\int_0^\chi d\chi' \Phi_{,ij}(\vec{x}(\chi'))\chi'\left(1 - \frac{\chi'}{\chi}\right) = \begin{pmatrix} -\kappa - \gamma_1 & -\gamma_2 \\ -\gamma_2 & -\kappa + \gamma_1 \end{pmatrix}. \tag{3.19}$$

The correlation between ψ_{ij} components give us the convergence and shear correlations, as they are linear combinations of ψ_{ij}. We denote the 2D vector $\vec{l} = (l\cos(\phi_l), l\sin(\phi_l))$, and similarly for $\vec{\theta}$ to explicitly express the components of ψ_{ij}. The 2D moments for the convergence $\kappa = (\psi_{11} + \psi_{22})/2$ can be calculated from:

$$\langle \psi_{ij}\psi_{lm}\rangle = (2\pi)^2\delta^2(\vec{l} - \vec{l'})P^{\psi}_{ijlm}, \tag{3.20}$$

$$P_\kappa(\vec{l}) = \frac{1}{4}(P^{\psi}_{2222} + P^{\psi}_{1111} + 2P^{\psi}_{2211}) = \frac{(l+1/2)^4}{4}\int_0^{\chi_\infty} d\chi \frac{g^2(\chi)}{\chi^6} P_\Phi((l+1/2)/\chi, z), \tag{3.21}$$

where the lensing kernel function $g(\chi)$ and the gravitational potential power spectrum P_Φ are defined as:

$$\langle \Phi(\vec{k})\Phi(\vec{k'})\rangle = (2\pi)^3\delta^3(\vec{k} - \vec{k'})P_\Phi(k), \tag{3.22}$$

$$g(\chi) \equiv 2\chi \int_\chi^{\chi_\infty} d\chi' \left(1 - \frac{\chi}{\chi'}\right) \frac{n_\kappa(z(\chi))}{\int dz n_\kappa(z)} \frac{dz}{d\chi}, \tag{3.23}$$

and we used Limber approximation.

We have two components for the shear, γ_1 and γ_2, which could also be linearly expressed by ψ_{ij} thus their correlation functions:

$$P_{\gamma_1}(\vec{l}) = \frac{1}{4}(P^{\psi}_{2222} + P^{\psi}_{1111} - 2P^{\psi}_{2211}) = \cos^2(2\phi_l)P_\kappa(l), \tag{3.24}$$

$$P_{\gamma_2}(\vec{l}) = P^{\psi}_{1212} = \sin^2(2\phi_l)P_\kappa(l). \tag{3.25}$$

Then we can Fourier transform a moments spectrum back to a angular two point correlation function through:

$$w_X(\theta) = \int \frac{dl^2}{(2\pi)^2} e^{i\vec{l}\cdot\vec{\theta}} P_X(\vec{l}). \tag{3.26}$$

In practice, instead a fixed coordinate system, we usually decompose the shear into tangential and cross direction, γ_t and $\gamma_\times$, which could be done by setting the 2D coordinate system for each pair of convergence such that $\phi_\theta = 0$. In such coordinates, $\gamma_t \equiv -\gamma_1$, $\gamma_\times \equiv -\gamma_2$ [52], as illustrated in 3.1. Accordingly, the two point correlation functions of the shear are also between two components. Since $\langle\gamma_t\gamma_\times\rangle = 0$, we usually adopt the two correlation functions $\xi_\pm$ defined as:

$$\xi_\pm = \langle\gamma_t\gamma_t\rangle \pm \langle\gamma_\times\gamma_\times\rangle. \tag{3.27}$$

Remembering that $\phi_\theta = 0$ in $\gamma_t, \gamma_\times$ decomposition, the Fourier transformation equation 3.26

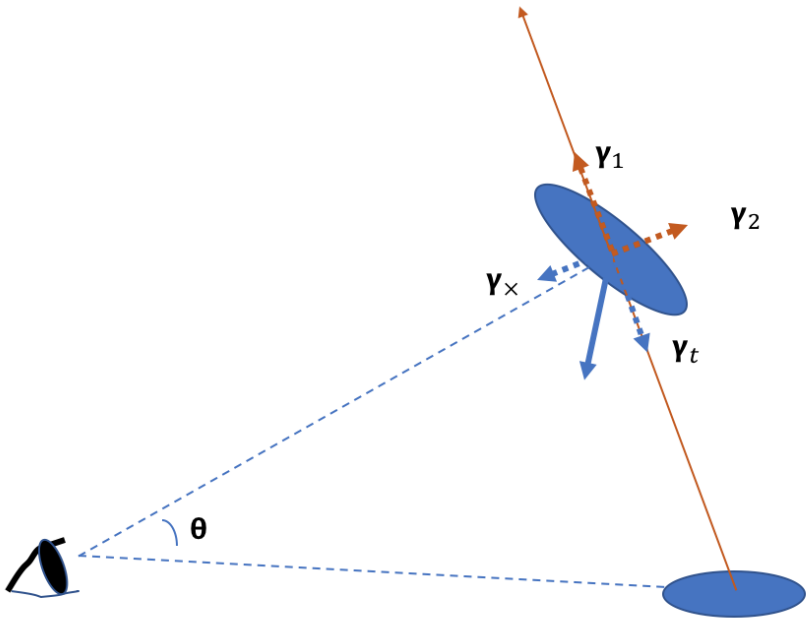

Figure 3.1: For an observer, γ_t is the component of the shear defined along the inverse of vector $\vec{\theta}$, and $\gamma_\times$ is the component perpendicular to $\vec{\theta}$.

gives us:

$$\xi_+^{ab}(\theta) = \int \frac{ldl}{2\pi} J_0(l\theta) P_\kappa^{ab}(l), \tag{3.28}$$

$$\xi_-^{ab}(\theta) = \int \frac{ldl}{2\pi} J_4(l\theta) P_\kappa^{ab}(l), \tag{3.29}$$

$$P_\kappa^{ab}(l) = \frac{(l+1/2)^4}{4} \int_0^{\chi_\infty} d\chi \frac{g^a(\chi) g^b(\chi)}{\chi^6} P_\Phi((l+1/2)/\chi, z), \tag{3.30}$$

where J_0 and J_4 are the zeroth and fourth Bessel function of the first kind. Here we consider two samples cross-correlated like in the previous section for the galaxy clustering.

In real world, we use the ellipticity of the galaxy image as an estimator of the shear. With moments measured from a galaxy image, the ellipticities are:

$$q_{ij} \equiv \int d^\theta I_{\rm obs}(\theta) \theta_i \theta_j, \tag{3.31}$$

$$\epsilon_1 \equiv \frac{q_{11} - q_{22}}{q_{11} + q_{22}}, \tag{3.32}$$

$$\epsilon_2 \equiv \frac{2q_{12}}{q_{11} + q_{22}}. \tag{3.33}$$

In the case where the unlensed (original) image of the galaxy is circular and all the distortions

are small under weak lensing, we find the approximation:

$$\epsilon_1 \simeq 2\gamma_1,\ \epsilon_2 \simeq 2\gamma_2. \tag{3.34}$$

One might worry that since we observe the galaxies edge-on most of the time, the original image is not circular anyway. But remember that we are statistically measuring the two point correlation functions. If the orientations of the galaxies are uncorrelated with each other, this randomly generated ellipticity will not have any effect on the correlation function. However, during the formation of the galaxies, some of them are indeed correlated with their the orientations. This factor brings in an important systematic uncertainty in the weak lensing measurements, called the intrinsic alignment, and it can be modeled at linear and nonlinear level [53, 54].

3.3 Galaxy-Galaxy Lensing Two Point Correlation Function

We call the two point correlation function of the tangential shear and the galaxy position the galaxy-galaxy lensing function. It takes one kernel from the galaxy sample, $W(\chi)$, and another kernel from the weak lensing shear, $g(\chi)$:

$$\gamma_t^{ab}(\theta) = \int \frac{ldl}{2\pi} J_2(l\theta) \frac{(l+1/2)^2}{2} \int_0^{\chi_\infty} d\chi \frac{g^a(\chi) W^b(\chi)}{\chi^4} P_{\Phi m}((l+1/2)/\chi, z), \tag{3.35}$$

where $P_{\Phi m}$ is the 3D k-space cross correlation spectrum for the matter overdensity and gravitational potential field.

Chapter 4

Baryonic Effects on the DES Cosmic Shear Analysis (Original Work)

In last chapter, I derived predictions for some large scale structure observables. From this chapter on, the contents are mostly based on the original work carried out by myself with collaborators in the Dark Energy Survey, and will present more technical details. This chapter starts with an overview of the Dark Energy Survey, which serves as background information also for the following chapters. After the DES introduction, I will focus on my major contribution to the DES Year-3 key paper – the effort to mitigate the impact of baryonic systematics on the DES Year-3 cosmic shear analysis.

4.1 DES Overview

The Dark Energy Survey is one of the currently ongoing photometric galaxy surveys, together with the Kilo-Degree Survey (KiDS) [55], Hyper Suprime Cam (HSC) [56]. DES has already finished its six years of data taking, covering ~ 5000 deg^2 of the sky as shown in figure 4.1, and recording information about $\sim$ 300 million galaxies. At the time the projects in this thesis were carried out, DES was still processing its large scale structure data products from Year-3 galaxy maps. All of the projects in this thesis use real DES Year-1 data product or synthetic DES Year-3 data products, as will be specified in the introductory or methodology sections of the following chapters.

The key cosmological data product of DES is something we call the 3x2pt data product, which is a combined measurement (joint covariance matrix) of the galaxy clustering, weak lensing shear, and the galaxy-galaxy lensing two-point correlation functions. Their theory predictions have been calculated in the previous section. The methodology including the covariance matrix calculation and the validation tests for the 3x2pt combined likelihood is

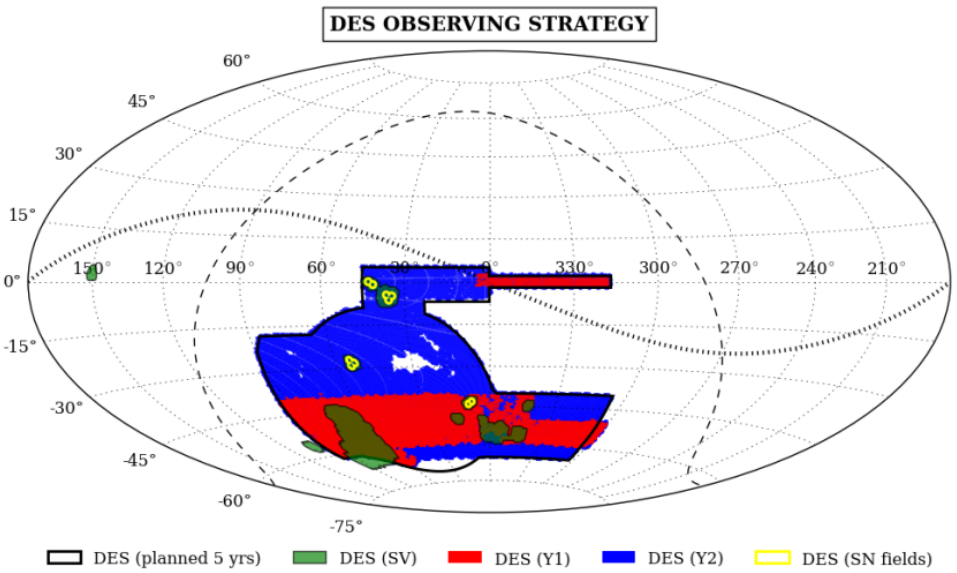

Figure 4.1: The observing stragegy footprint of DES. See https://www.darkenergysurvey.org/the-des-project/survey-and-operations/ .

presented in the paper [50], and the measurements of the data products are summarized in [51,52,57]. The following paragraphs will provide a brief summary of the above information.

In the galaxy-galaxy lensing context, the source galaxies are lensed by the lens galaxies. Hence there is physically meaningful correlation between the image-distortion, namely the shear, of the source galaxies and the position of the lens galaxies. The source and lens galaxy number densities are denoted by n_κ and n_g in chapter 3. The 3x2pt correlation functions are measured from m redshift bins of the source galaxy catalog and n redshift bins of the lens galaxy catalog, where m and n are dependent on the algorithm used to categorize the galaxy samples into redshift bins.

For the lens galaxies, DES Year-1 used the redMaGiC [58] algorithm to construct galaxy position samples and to derive the photometric redshift estimates (photo-z) for the lens population $n_g^a(z)$. The lens galaxies are binned into five redshift ranges, $z = [(0.15-0.3), (0.3-0.45), (0.45-0.6), (0.6-0.75), (0.75-0.9)]$.

For the source galaxies, DES Year-1 used METACALIBRATION [59, 60] to measure the galaxy shape samples and the source galaxy population $n_\kappa^a(z)$ photo-z. The catalog from METACALIBRATION is cross-checked with another algorithm IM3SHAPE [61], validating its use for cosmological analysis purpose [52, 62]. We have four redshift bins for the source galaxies $z = [(0.2-0.43), (0.43-0.63), (0.63-0.9), (0.9-1.3)]$.

The redshift distributions of the resulting lens and source galaxy populations are illustrated in figure 4.2.

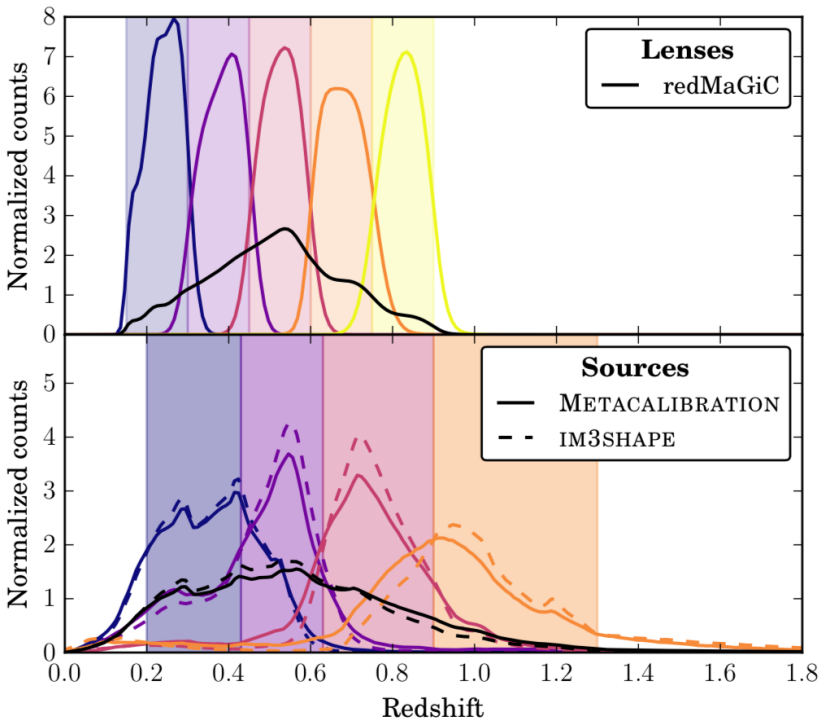

Figure 4.2: The lens and source galaxy population distribution against redshift. The catalogs produced by redMaGiC and METACALIBRATION are used for DES Year-1 cosmology analysis.

Given the galaxy position and shape measurements, we use the Landy-Szalay estimator to obtain the two-point correlations [63]:

$$\hat{\xi} = \frac{\mathrm{DD} - 2\mathrm{DR} + \mathrm{RR}}{\mathrm{RR}} \tag{4.1}$$

where $\hat{\xi}$ is the estimator for any sort of two-point, DD is the number of pairs with a separation in an log-spaced angular bin $[\theta, \theta e^{\Delta}]$, RR is the same for a randomly distributed catalog, and DR is the cross-correlated pair counts between data and random distributions. DES measure each of the 3x2pt spectrum using treecorr algorithm [64] [1], in 20 log-spaced angular bins in the range $2.5' < \theta < 250'$.

In DES Year-1 3x2pt, we have 5 auto-correlated galaxy clustering two-point functions $w^a(\theta)$, $\sum_{n=1}^{4} n \times 2 = 20$ weak lensing cosmic shear two-point functions $\xi_{\pm}^{ab}$, and $4 \times 5 = 20$ galaxy-galaxy lensing two-point functions. In total, we have 45 angular 2pt function measurements and $45 \times 20 = 900$ data points. The 400 measurements of DES Year-1 cosmic shear correlations are shown in figure 4.3. The points in the grey area are removed from the cosmology analysis due to the systematic uncertainties mainly caused by the baryonic

[1] https://github.com/rmjarvis/TreeCorr

effects. As we can see from figure 4.3, these systematics forced us to abandon a considerable amount of the information that could potentially help constrain cosmology. Later in this chapter I will investigate how we balance between the constraining power and the systematic bias due to baryonic effects, under DES Year-3 precision.

We use the Bayesian statistics to carry out the cosmological parameters analysis. In order to do so, we utilize the Monte Carlo or nonlinear regression algorithms to maximize the posterior for the best-fit parameter matching the measured data. The posterior is expressed by the following equation in terms of the prior and the measured data likelihood at a point $\mathbf{p}$ in the n-dimensional parameter space:

$$P(\mathbf{p}|\mathbf{D}) = \frac{\mathcal{P}(\mathbf{p})L(\mathbf{D}|\mathbf{M}(\mathbf{p}))}{P(\mathbf{D})}, \tag{4.2}$$

where $\mathbf{D}$ is a measured data vector, for example the 900 data points in the 3x2pt analysis; $\mathbf{p}$ is a point in the full varying parameter space, including the cosmological parameters and the nuisance parameters modeling the systematics; $\mathbf{M}(\mathbf{p})$ is the theory prediction for $\mathbf{D}$ given parameters $\mathbf{p}$. The left-hand side of this equation is the posterior of the parameters given a measurement, $\mathcal{P}(\mathbf{p})$ is the prior information on the parameters before measurement, L is the likelihood, and $P(\mathbf{D})$ is the probability only dependent on data, called the Bayesian evidence. The calculation of $P(\mathbf{D})$ requires an integral over the full parameter space. Such an integral is difficult to compute, because the the dimension of the full parameter space is usually too high. For this reason, in practice most of the time we just treat $P(\mathbf{D})$ as a normalization factor, when we are mainly interested in the parameter posteriors. However, the Bayesian evidence could provide important information in the model selections.

Assuming Gaussianity, we can calculate the likelihood of the measured data vector $\mathbf{D}$ with the model parameters $\mathbf{p}$.

$$L(\mathbf{D}|\mathbf{p}) \propto \exp\left(-\frac{1}{2}\left[(\mathbf{D}-\mathbf{M}(\mathbf{p}))^T C^{-1}(\mathbf{D}-\mathbf{M}(\mathbf{p}))\right]\right) \tag{4.3}$$

where C is the covariance matrix. In DES Year-1 analysis, the covariance matrix is theoretically calculated using the software **COSMOLIKE** [65]. The final covariance matrix used in the analysis consists of Gaussian and non-Gaussian contributions computed analytically using the four-point correlation functions. The non-Gaussian part is mainly induced by the non-linear density field at small scales and employs a halo model in its derivation. The Gaussian part can be expressed by the product of two-point correlation functions, and is inversely proportional to the number of measured modes in $[\theta, \theta e^{\Delta}]$ range [50, 66]. Hence for DES Year-3 which has three times the survey volume as DES Year-1, the error bar

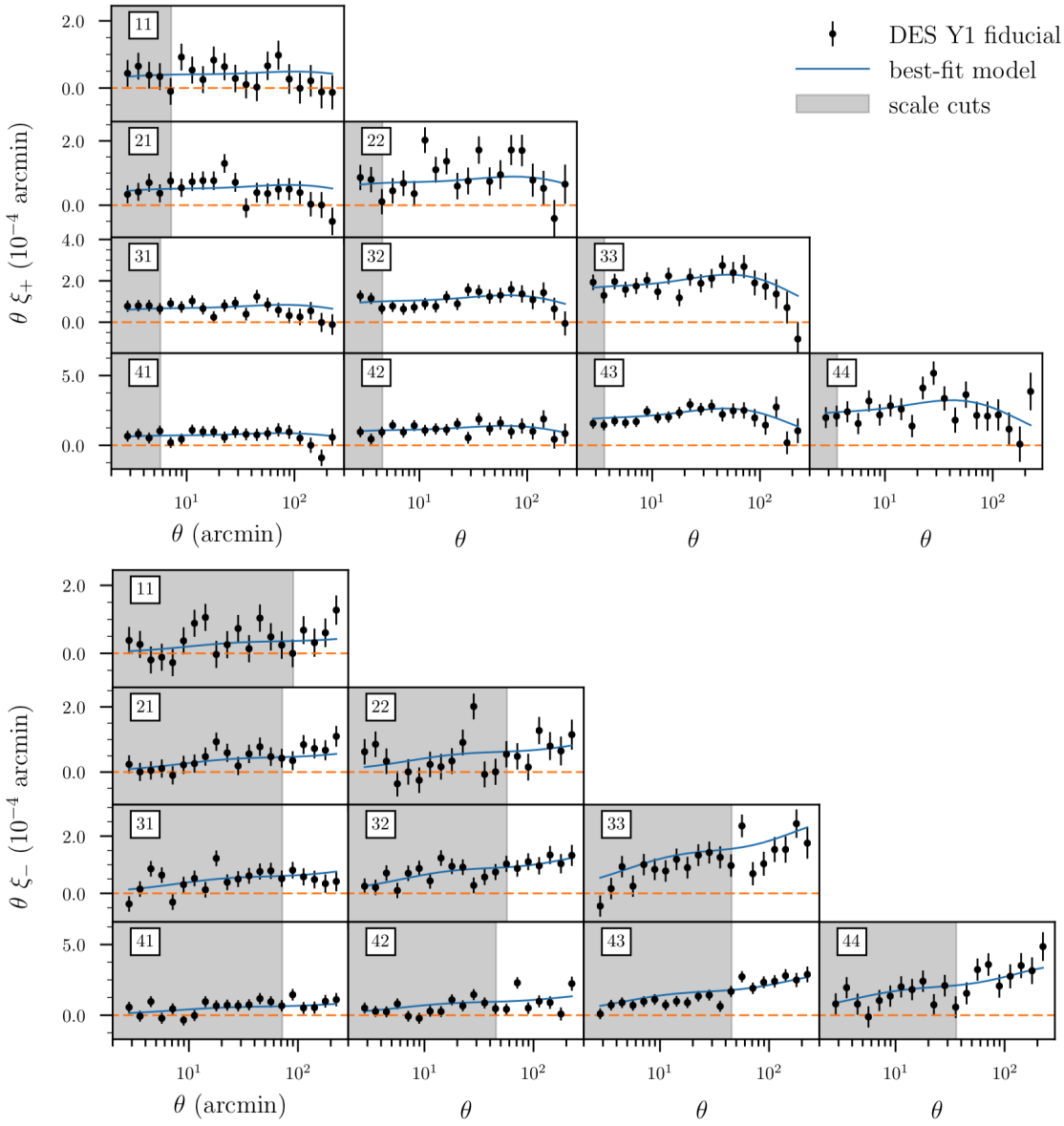

Figure 4.3: DES Year-1 measurement of cosmic shear two-point correlation functions $\xi_{\pm}$. The points in the grey area were cut out from the cosmology analysis, due to the lack of knowledge on the systematic uncertainties caused by the baryonic effect.

$\sigma_{\text{Year}-3} \sim \sqrt{C} \sim N_{\text{modes}}^{-1/2} \sim V_{\text{survey}}^{-1/2} \sim \frac{\sigma_{\text{Year}-1}}{\sqrt{3}}$. This is just the leading order improvement on the constraining power of DES Year-3 analysis. Y3 GOLD photometric data set also improved the althorithms for photometric calibration, objects classification etc. comparing to Y1 GOLD data set, as discussed in detail in [67].

The rest of this chapter investigates that under Year-3 precision, i.e. using the covariance calculated under Year-3 conditions, how cosmic shear constraints on cosmological parameters are affected by the baryonic feedback and how the corresponding systematic uncertainties should be approached in the DES Year-3 analysis. Note that since this project happened when other analysis choices of Year-3 were being developed at the same time, the Year-3 covariance matrix used in the tests which depends on the cosmology is not exactly the same as the finalized version. The survey volume factor mentioned in the previous paragraph is predominant comparing to other details in the pipeline engineering, hence the covariance matrix used in this study is expected to capture the change in precision with sufficient accuracy.

4.2 Baryonic Feedback in Cosmic Shears

The cosmic shear two-point correlation function or harmonic space spectrum, as presented in the previous chapter, is a powerful measurement of the two-dimensional projection of the matter power spectrum in three-dimensional k-space. The matter power spectrum that captures structure formation features in the universe can be very reliably predicted by solving the perturbation equations at linear scale. However, perturbation equations are only accurate when the perturbations to density are small with $\delta << 1$. When this condition fails, higher order terms like δ^2 become important and the equation becomes nonlinear. In late universe, nonlinear effects on the matter power spectrum starts to show up for wave numbers $k \gtrsim 0.1h$ Mpc^{-1}. On smaller scales, i.e. larger wave number k, we need to emulate the N-body simulation measurements [68,69] or use empirically fitted Halo models [70,71] to predict nonlinear matter power spectrum. Nonlinear matter power spectrum has a little bit higher theoretical uncertainty than the linear scale physics due to their complexity, but still considered to be precise enough for the current generation observations, with better than $\sim 5\%$ precision at scales $k < 1h\text{Mpc}^{-1}$ depending on the methodology.

These calculations are feasible thanks to the simplicity of dark matter interaction. The dark matter dominates the matter density in our universe, and it feels gravity only on cosmological scales. A bigger challenge for current generation of precision cosmology experiments is presented when considering the effect of baryonic interactions on structure formation. Standard Model interactions are much stronger than gravitational interaction, hence as expected

they redistribute the matter perturbation field in more dramatic ways that are not calculable through linear perturbation theories. The most prominent baryonic effects that redistribute the total matter density field are the active galactic nuclei (AGN) or Supernovae feedback that in general expels the gas content, and the central galaxy or gas cooling that results in a steeper density profile towards halo centers [72]. These baryonic processes could alter the matter power spectrum at scales $0.1h\text{Mpc}^{-1} \lesssim k \lesssim 10h\text{Mpc}^{-1}$ by as much as $10\% - 20\%$ [73]. This number has large uncertainty, much larger than the precision requirement $\lesssim 5\%$ on the prediction of the matter power spectrum for the current generation weak lensing surveys. Astrophysicists have been trying to develop the simulations with hydrodynamic fluid solvers to elucidate the baryonic feedback effects. But even in hydrodynamic simulations, the baryonic effects varies in different simulation suites due to different sub-grid recipe parameters. The scale of AGN and other baryonic events are too small to be resolved under current simulation precision so sub-grid recipe is necessary. Such sub-grid recipe parameters describing the magnitude and other features of the baryonic feedback lack theory predictions and high-resolution observations to cross-check with. Hence the baryonic feedback is a major cause of the systematic uncertainty in weak lensing surveys at small scales. The possible realizations of the baryonic effects from several hydrodynamic simulations are illustrated in figure 4.4. The y-axis of figure 4.4 shows the difference between the baryon-contaminated and dark-matter-only synthetic cosmic shear measurements, where the baryonic feedback predicted by different simulation suites are implemented into the synthetic data as described in sub-section 4.3.1.

As the leading current generation weak lensing survey, the DES explored several strategies to mitigate the baryonic systematics. I contributed to these effort by testing one of the strategies for the DES analysis pipeline, which uses a halo model built to describe the baryonic effects on nonlinear matter power spectrum. The final goal is to determine the best way to approach the baryonic uncertainty for DES Year-3 cosmology analysis.

To start, I will present the (incomplete) list of options for the purpose of mitigating the baryonic effects, then continue on to the specific strategy we tested in the methodology section.

Baryonic Effect Mitigation Strategies

1. **Parametrized Baryon Models.** People have spent extensive efforts trying to accurately model the baryon effect on the matter power spectrum. Unlike PCA, most of the baryonic parameters introduced by this type of the models have physical meanings. Hence these baryonic parameters are better-motivated to be constrained in combined

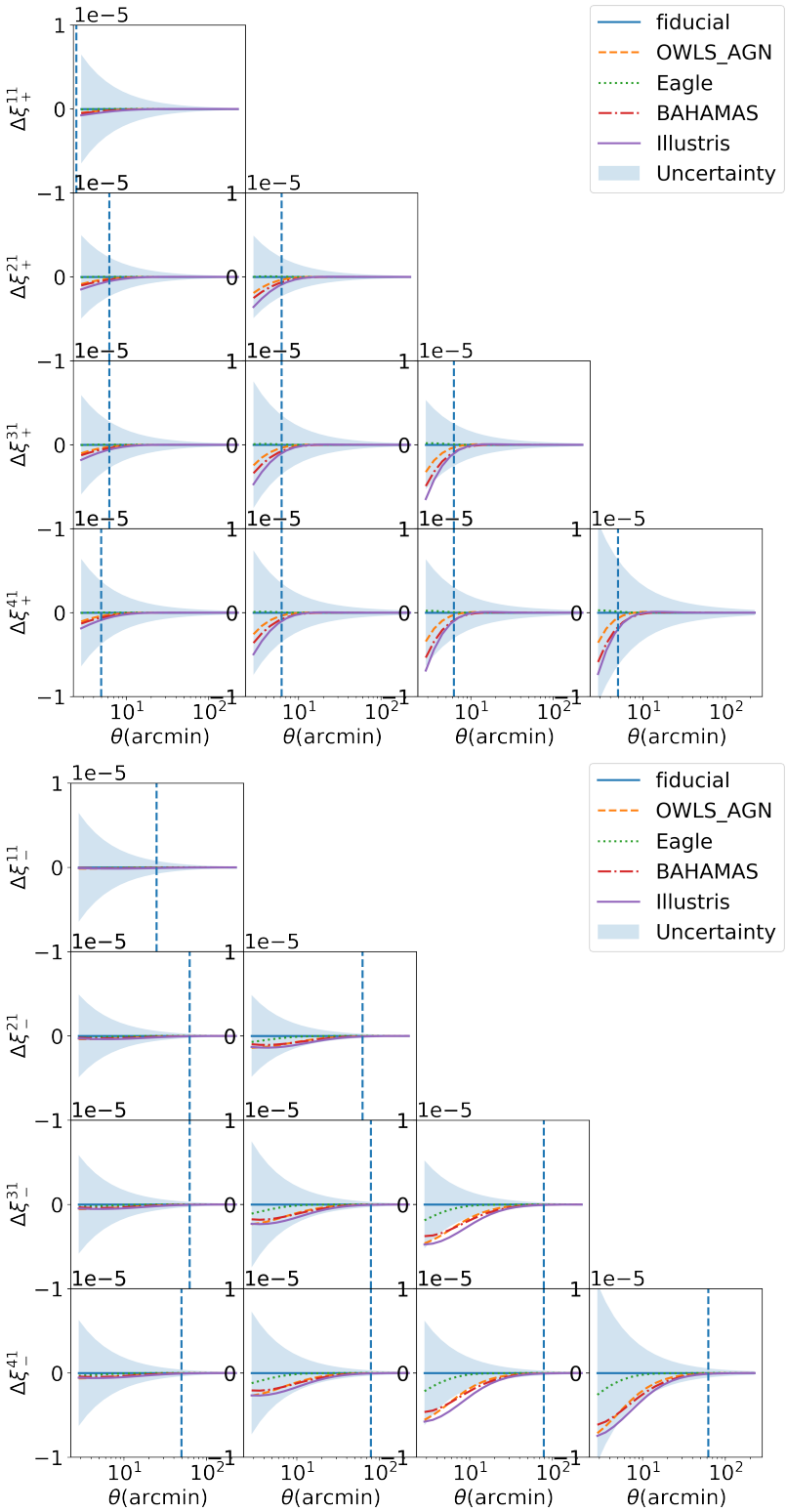

Figure 4.4: The baryonic effect on cosmic shear $\xi_\pm$ depicted by the difference between baryonic and dark-matter-only synthetic data (y-axis). They are generated based on the comparison between the hydrodynamic and dark-matter-only simulations of OWLS_AGN, eagle, BAHAMAS-$T_{\rm heat} = 8.0$WMAP-9 and Illustris suites. The dashed vertical lines are the DES Year-3 scale cuts. The survey measurement uncertainty is theoretically calculated based on DES Year-3 footprint.

observations, for example cosmic shear with X-ray clustering. They could possibly set priors on the baryonic effect for future surveys. The baryonification, or the baryon correction model (BCM) is a promising model which describes the rescaling of power spectrum due to baryonic physics, by the parameters characterizing the gas, galaxy fraction and their density profiles in halos [72]. Mead el al. proposed another halo model in 2015 that could capture the nonlinear and baryonic features of the matter power spectrum in ΛCDM, massive neutrino, $w(a)$ dark energy, and modified gravity cosmology [74, 75]. Mead's halo model introduces seven halo parameters, but most of them are fixed to the best-fit values of the (DMO) N-body Cosmic Emu suite of simulations [76]. The baryonic effects are claimed to be captured by varying two halo parameters among the seven, validated against the hydrodynamic OWLS simulations [77]. In this chapter I will examine how efficient they are at mitigating the baryonic systematics in DES Year-3 cosmology analysis.

2. **Principle Component Analysis.** This method carries out principle component analysis on several suites of hydrodynamic simulations, and takes the first one or a few principle components to span a linear space in hope that it captures the baryonic effect features for general cases. Huang et al.'s work explored this method on DES Year 1 data extensively [78]. In general, it is a powerful tool to deal with baryonic systematics, while one of its short-comings is the lack of physics interpretation of the principle component amplitude constraints.

3. **Simulation-Built Emulators.** If we can measure the matter power spectra from enough realizations of hydrodynamic simulations, sampling the cosmological parameter space densely enough, we can interpolate the spectrum as a function of the cosmological parameters. Such cosmological emulators have been built for several suites of hydrodynamical simulations, including but not limited to the Mira-Titan universe [68] and the Coyote universe [79, 80]. The advantage of emulators is their relatively reliable numerical simulations of the universe from first principles, despite that the baryonic effects still vary in a (narrower and narrower) range based on sub-grid recipe choices. However, due to the expensiveness of the high-resolution hydrodynamic simulations, the emulator predictions on matter power spectrum are only able to cover a very narrow range of the cosmology. For this reason, in the real data analysis where we need to sample a wide area of the cosmological parameter space, we can not use the emulator as our theoretical prediction currently. In any case, the node simulations of the emulators provide accurate measurements of the power spectra with baryonic effects. They are the perfect ingredients necessary for the model building efforts for the baryonic effects

described in the parametrized baryon models paragraph.

4. **Scale Cuts.** Lastly, we come to the computationally most economical strategy to mitigate baryonic effects. Since the baryonic effects only impact observables below certain physical distance scales, to avoid the corresponding systematics we can just cut the small scales out from the data set used for cosmological analysis. There are multiple ways to determine the scale cuts, from roughly restoring the physical scale in the angular space [50] to cleaner x-cuts decoupling the lensing kernels [81]. The DES Year 1 analysis used the scale-cut strategy [9], and I will show by the end of this chapter that for DES Year 3 precision, this is still the most economical and reliable way of handling the baryonic systematics.

4.3 Methodology

We carried out the baryonic systematics tests by runing full Monte Carlo chain on DES Year-1 analysis pipeline. The analysis pipeline and the samplers for Monte Carlo process is described in appendix A. The baseline ΛCDM analysis pipeline has 26 varying parameters, while wCDM introduces one more cosmological parameter w, and the HMcode introduces another two halo model parameters A and η_0, as listed in table 4.1 and table 4.2.

In all of the validation tests in this project, we used the covariance matrix calculated by COSMOLIKE for DES Year-3 precision, as of the version produced by the analysis group in April 2019. All the data vectors are synthetic and are generated at the cosmology near the bestfit of the DES Year-1+Planck result. The synthetic data vectors are calculated from the theory prediction pipeline (See appendix A), with no noise added.

HMcode is the code calculating the nonlinear power spectrum from Mead's halo model as mentioned in the previous section [74,75]. It is claimed to be able to capture the baryonic effects in the nonlinear matter power spectrum by varying two halo parameters, the minimum halo concentration A and the constant part of the halo bloating parameter η_0. The definition of these two parameters will be briefly summarized in the following paragraphs. In short, they are designed to give more freedom to the halo density profile due to the uncertain redistribution of the matter field from baryonic feedback.

To start with, the halo model prediction of the matter power spectrum can be represented by a smooth combination of the one-halo and two-halo terms:

$$\Delta^2(k) = \left[(\Delta^2_{2H})^\alpha + (\Delta^2_{1H})^\alpha)\right]^{1/\alpha}, \tag{4.4}$$

where the two-halo term is basically the linear matter power spectrum damped at quasi-

Table 4.1: Cosmological and nuisance parameters in DES-Y1 3x2pt baseline ΛCDM analysis, and their priors. The center values listed in the flat priors are the values at which the testing synthetic data vectors are generated. The baseline synthetic data vector is generated by the fiducial DES pipeline at center values, and the baryonic synthetic data vector on this basis is contaminated by the baryonic effects measured from simulations, as described in subsection 4.3.1. The definition of the nuisance parameters can be found in appendix A.

Parameter	Prior
Cosmological	
$\Omega_{\rm m}$	flat $(0.1, 0.295, 0.9)$
h	flat $(0.55, 0.6881, 0.9)$
$\Omega_{\rm b}$	flat $(0.03, 0.04680.07)$
$n_{\rm s}$	flat $(0.87, 0.9676, 1.07)$
$A_{\rm s}$	flat $(5 \times 10^{-10}, 2.26 \times 10^{-9}, 5 \times 10^{-9})$
$\Omega_\nu h_0^2$	flat $(0.0006, 0.0006155, 0.01)$
σ_8 (derived)	center value 0.8345
$S_8 = \sigma_8\sqrt{\Omega_m/0.3}$ (derived)	center value 0.8275
Lens Galaxy Bias	
b_1	flat(0.8, 1.45, 3.0)
b_2	flat(0.8, 1.55, 3.0)
b_3	flat(0.8, 1.65, 3.0)
b_4	flat(0.8, 1.8, 3.0)
b_5	flat(0.8, 2.0, 3.0)
Intrinsic Alignment	
$A_{IA}(z) = A_{IA}[(1+z)/1.62]\eta_{IA}$	
A_{IA}	flat (-5.0, 0.0, 5.0)
η_{IA}	flat (-5.0, 0.0, 5.0)
Lens photo-z shift (red sequence)	
Δz_l^1	Gauss (0.0, 0.007)
Δz_l^2	Gauss (0.0, 0.007)
Δz_l^3	Gauss (0.0, 0.006)
Δz_l^4	Gauss (0.0, 0.01)
Δz_l^5	Gauss (0.0, 0.01)
Source photo-z shift	
Δz_s^1	Gauss (0.0, 0.016)
Δz_s^2	Gauss (0.0, 0.013)
Δz_s^3	Gauss (0.0, 0.011)
Δz_s^4	Gauss (0.0, 0.022)
Shear calibration	
$m^i, (i = 1, ...4)$	Gauss (0.012, 0.023)

linear scales, and the one-halo term is determined by the density profile of the halo. The

Table 4.2: Varying parameters in addition to the defaults in table 4.1. In wCDM cosmolgy where dark energy is allowed to have the equation of state parameter $w \neq -1.0$, we vary w in the flat prior listed here. When we push to smaller scales of the cosmic shear analysis, we use HMcode to replace takahashi-halofit and introduce two more halo parameters.

Parameter	Prior
Cosmological	
w	flat $(-2.0, -1.0, -0.33)$
Halo Model – HMcode	
A	flat $(1.0, 3.13, 7.5)$
η_0	flat $(0.4, 0.603, 1.0)$

halo density profile in HMcode starts from the NFW profile [82]:

$$\rho(r) = \frac{\rho_N}{(r/r_s)(1 + r/r_s)^2}, \tag{4.5}$$

where the scale radius is usually determined by $r_s = r_v/c$, with r_v being the virial radius of the halo and c being the concentration. Their first baryonic Halo parameter A is defined as the minimum halo concentration:

$$c(M, z) = A\frac{1 + z_f(M)}{1 + z}, \tag{4.6}$$

where $z_f(M)$ is the formation redshift of the halo as a function of halo mass M. Since z of our observation are always smaller than $z_f(M)$, A is by definition the minimum concentration of the halo. The variation of A will change the scale of the core of a NFW-profile halo.

To obtain the one-halo term of the power spectrum in the wave-number space, we need the Fourier transformed density profile:

$$W(k, M) = \frac{1}{M}\int_0^{r_v} \frac{\sin(kr)}{kr} 4\pi r^2 \rho(r, M) dr \tag{4.7}$$

Here [75] introduces another halo parameter to capture the bloating effect on the halo due to the baryonic feedback. This adaption to the baryonic effects is done by rescaling the halo density profile used for the one-halo term in the power spectrum:

$$W(k, M) \to W(\nu^\eta k, M). \tag{4.8}$$

The peak threshold $\nu \equiv \delta_c(z)/\sigma(M, z)$. $\delta_c(z)$ is the critical over-density, defined as the linearly evolved over-density at redshift z for an initial over-density δ_i that completed its nonlinear spherical collapse at redshift z. $\sigma(M, z)$ is the matter over-density field filtered on

a comoving radius R that $M = \frac{4\pi}{3} R^3 \bar{\rho}$ (the density is also the comoving one).

$$\sigma(R, z) = \int_0^\infty \Delta^2(k, z) \left(\frac{3 j_1(kR)}{kR} \right)^2 d \ln k \tag{4.9}$$

η could have higher order dependence on σ_8, where σ_8 is the filtered over-density field defined above with $R = 8h^{-1}$ Mpc. In the default HMcode setting we only vary the zeroth-order term, η_0, for baryonic effects.

In the original paper [74,75], HMcode's ability to model the baryonic feedback by varying halo parameters A and η_0 is tested on several simulations in the OWLS suite with different sub-grid baryonic event recipes. HMcode is also adopted for the cosmology anlaysis or validation tests in several recent weak lensing surveys, including KiDS-450 [55] and HSC first-year [83]. Thus we would like to test if HMcode could also help DES Year-3 to mitigate the baryonic effects.

There are two criteria to consider in the baryonic analysis choices. The first is the minimization of the bias on cosmological parameters. If our theory predicted data vectors generated from the prior parameter space do not include a good fitting to the real universe measurement, the cosmological parameters that we are most interested in might be biased. The second criteria is the maximization of the constraining power on cosmological parameters. It can be achieved by including more data points into the analysis. By pushing scale cuts to smaller angles, we are likely to see the increase in both the constraining power and the bias. Because as figure 4.4 shows, the amplitudes of baryonic effects grow at smaller scales. We need to experiment on different analysis choices to find a balance between the bias and the constraining power on Ω_m and σ_8, the two best-constrained cosmological parameters in DES survey.

4.3.1 Baryon Contaminated Simulated Data Vectors

We need a synthetic and controllable realization of the baryon effects on the data vectors to test our anlaysis recipes. To do so, as described in Huang el al. [84], we take the measured ratio between the hydrodynamic simulated matter power spectrum and the corresponding dark-matter-only (DMO) simulated matter power spectrum, then multiply this ratio to the theory predicted nonlinear matter power spectrum in a cosmology.

$$P_m^{\text{th,baryon}} = \frac{P_m^{\text{sim,hydro}}}{P_m^{\text{sim,DMO}}} P_m^{\text{th,DMO}} \tag{4.10}$$

The 3x2pt data vector derived from such baryonic contaminated matter power spectrum

is labeled as synthetic baryonic data vector, and the 3x2pt derived from DMO nonlinear matter power spectrum is labeled as synthetic DMO, or the baseline data vector. The Cosmosis module that processes such baryonic decoration of the nonlinear matter power spectrum can be found in the repository https://bitbucket.org/joezuntz/cosmosis-standard-library/src/des-y3/structure/.

4.3.2 Analysis Choices

We run MCMC chains on the synthetic baryonic or DMO data vectors to investigate the influence of our analysis choices on the cosmological parameter constraining power and bias. The DES analysis pipeline is described in the appendix A. The controlled variation in our analysis choices are mainly on these three factors:

1. **The nonlinear module.** DES fiducial Year-1 analysis uses takahashi-halofit [71] to model the nonlinear matter power spectrum, which assumes dark matter only cosmology. We implemented the HMcode based on dark matter + baryonic halo model [75] into the Cosmosis, and use it as an alternative nonlinear module.

2. **The halo (baryonic) parameters.** After validating with multiple hydrodynamic simulations, the general baryonic effect is claimed be described by the two halo parameters A and η_0 of the HMcode [74], so marginalizing over them can help mitigate the baryonic systematics. [75] has also provided fiducial bestfit values of them to be $A = 3.13$ and $\eta_0 = 0.603$ in DMO case (fittings to all cosmic emu simulations [79, 80]). We can choose between varying HMcode parameters $A \in [1.0, 7.5], \eta_0 \in [0.4, 1.0]$ with flat priors, or fixing HMcode parameters $A = 3.13, \eta_0 = 0.603$. The prior range is determined from [74] Figure 6, which should cover the 2σ credible interval of the fitting to OWLS suite of simulations, covering the dark-matter-only case and several other ansatzs for the baryonic feedback.

3. **Scale cuts.** We try to push to smaller scales for the cosmic shears and include more data points in our 3x2pt analysis. We did this by multiplying a smaller-than-one factor with the Year-1 scale cuts illustrated in figure 4.3. Naturally, as the scale cuts on ξ_- are larger to start with, when we push to smaller scales there will be more data points joining in the analysis from ξ_- than from ξ_+. The corresponding number of data points for different scale cut choices are summarized in table 4.3.

After running full analysis pipeline on different combinations of the simulated data vectors and analysis choices, we reach the conclusions in the next section.

Scale Cuts	# of pts in 3x2pt	# of pts in cosmic shear
Y1 cuts	457	227
0.7× Y1 cosmic shear	497	267
0.5× Y1 cosmic shear	514	284
0.3× Y1 cosmic shear	550	320
0.1× Y1 cosmic shear	590	370

Table 4.3: The number of measurements when applying different scale cuts on $\xi_{\pm}(\theta)$. Throughout 3x2pt tests, the scale cuts on $w(\theta)$ and $\gamma_t(\theta)$ are unchanged from the Year-1 cuts, because the small scale systematics on these two are dominated by the physics other than baryonic effects.

4.4 Results

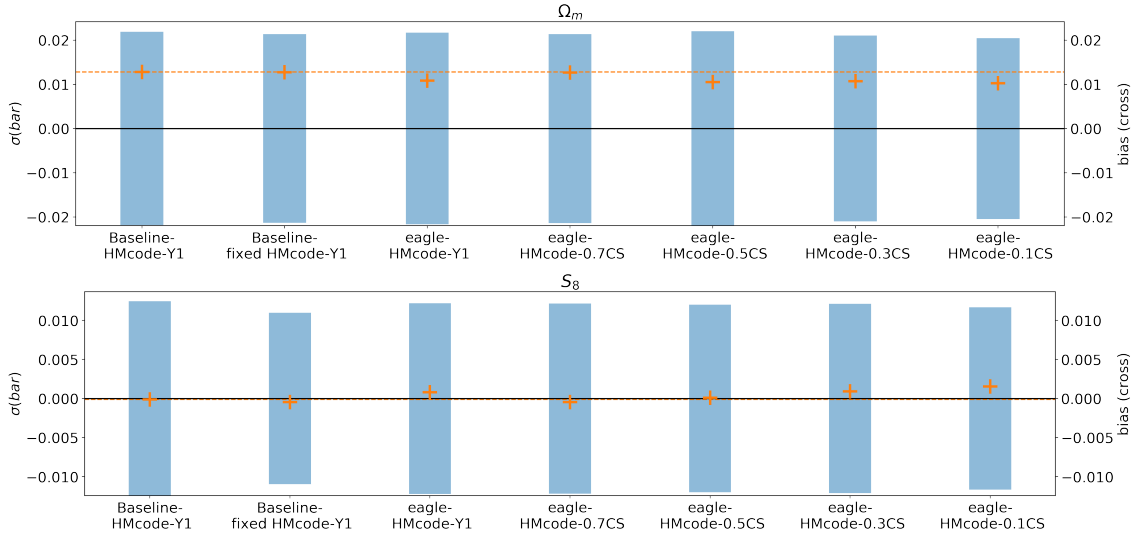

Figure 4.5: The baryonic systematics tests investigating the constraining power and bias on cosmological parameters when we push to smaller scales. The baseline synthetic data vector is generated by HMcode, fixing halo parameters $A = 3.13, \eta_0 = 0.603$. eagle data vector is generated by contaminating the baseline data vector by the baryonic effect measured from eagle simulations. The blue bars in the figure are the standard deviations of Ω_m and S_8 in the Monte Carlo chains with different analysis choices. The orange crosses are the 1D marginalized peak deviations from the fiducial values. Because there are projection effects in the high-dimensional parameter space, the bias should be compared with the baseline chain on the left. The first three chains in the figure use DES Year-1 scale cuts, and the rest of them subsequently use $0.7, 0.5, 0.3, 0.1\times$ Year-1 cosmic shear scale cuts, keeping the galaxy clustering and galaxy-galaxy lensing scale cuts unchanged. Other than the second chain which used HMcode but fixing the halo parameters, other chains vary $A \in [1.0, 7.5], \eta_0 \in [0.4, 1.0]$.

The result of analysis-choice tests are illustrated in the figure 4.5. The blue bars are

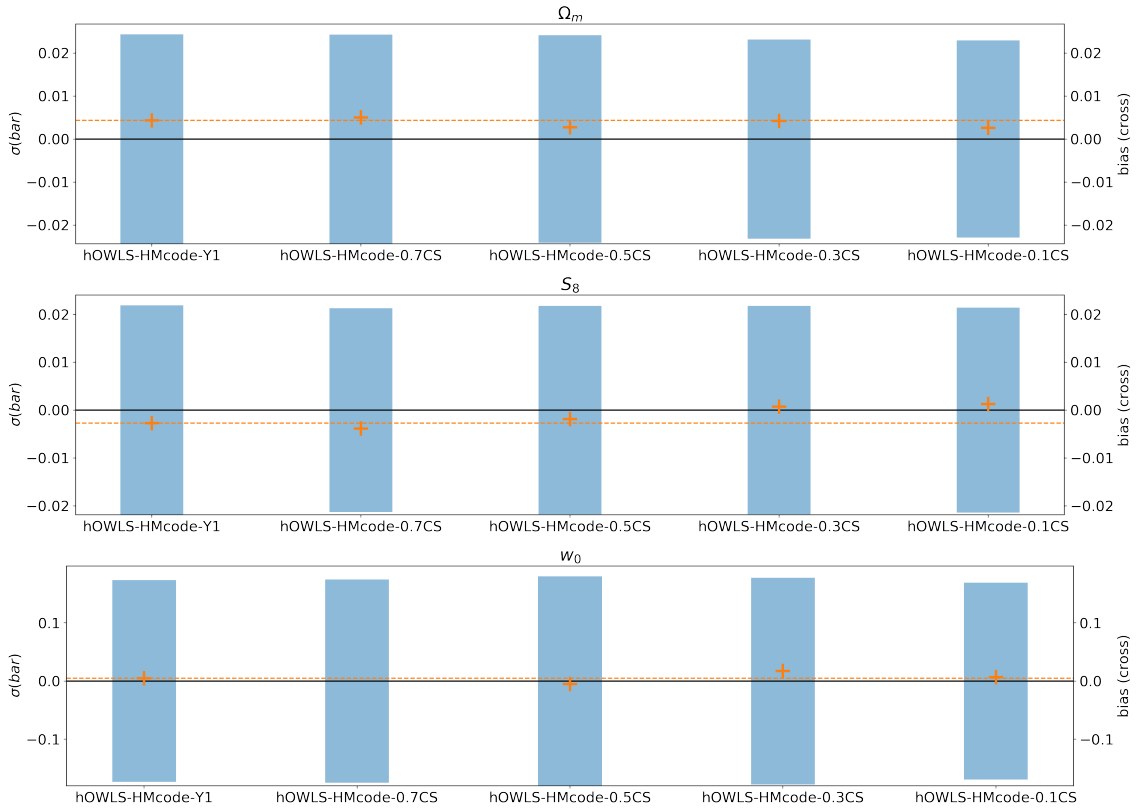

Figure 4.6: Similar tests as figure 4.5, except for that we generate DMO baseline data vector using takahashi-halofit, vary w_0 in wCDM cosmology, and contaminate baseline data vector with stronger baryonic feedback measured from OWLS-AGN simulations. There are difference between takahashi-halofit and HMcode even in the DMO case, so these chains cannot be compared directly to the baseline run in figure 4.5. But the trend from left to right, from larger scale to smaller scale in this stronger baryonic feedback case demonstrates the same conclusion as before: the cosmological parameters are protected from baryonic bias, however we do not gain much constraining power on them from the baryon-affected small scale physics.

the standard deviation of Ω_m and S_8 in the MCMC chain, characterizing the constraint power. The orange crosses are the marginalized 1D peak bias from the truth value of the parameter. Note that because there are projection effects in the high-dimensional parameter space, the biases should be compared with the baseline run one, where we have the dark matter only data vector in ΛCDM uncontaminated by any baryonic effects. The results in figure 4.5 used eagle simulation measurements to contaminate the data vectors. We see that after introducing two extra halo parameters to capture the baryonic features, when including smaller scale data into the analysis we are protected from extreme bias, with the difference of cosmological parameter 1D peak values between baryonic and dark-matter-only validation tests $< 0.2\sigma$. So HMcode does help mitigating the bias due to the baryonic effects.

However, the blue bars denoting the constraint power did not shrink notably up until 0.3 times Year-1 cosmic shear scale cuts. Another similar set of tests for wCDM data vectors contaminated by OWLS-AGN simulation is illustated in Figure 4.6. Again in a different cosmology, OWLS-AGN tests confirm the result that smaller scale cosmic shear measurements do not contribute much to the constraining power on Ω_m and S_8. Qualitatively speaking, given the increase of the number of data points from DES Year-1 scale cuts to 0.1 times Year-1 cosmic shear scale cuts listed in table 4.3, we expect the uncertainty to shrink $\sim 12\%$ percent based on the principle of $\sigma \sim \frac{1}{\sqrt{N_{\rm pts}}}$. However for both Ω_m and S_8, which are the two tightest-constrained cosmological parameters for DES, the Monte Carlo chains obtain only $\sim 6\%$ shrinkage in the standard deviation for these two parameters. Large amount of the additional information at small scales only contribute to the constraints on the nuisance halo parameters, as shown in figure 4.7. Taking the definition of figure of merit (FoM) to be [3]:

$$\mathbf{FoM} = (\det C)^{-1/2} \tag{4.11}$$

The increase of $\mathbf{FoM}^{\Omega_m - S_8}$ is $\lesssim 3.0\%$, while $\mathbf{FoM}^{A-\eta_0}$ multiplies by $\mathcal{O}(1)$ factors when we push to smaller scales.

Such small gain in the constraining power of Ω_m and S_8 is even approaching the uncertainty due to the Monte Carlo sampler, i.e. the choice of using polychord, multinest or emcee sampler, and the statistical fluctuation between each realization of the Monte Carlo chains. Meanwhile, the analysis choices using more data points and more time consuming nonlinear code (HMcode) are increasingly CPU-time expensive. So for DES Year-3 anlaysis, the most economical and conservative analysis choice is still to exert the scale cuts that exclude the baryonic scales.

DES Year-3 has higher precision than Year-1 thanks to its larger survey area. We need to determine new scale cuts for the Year-3 analysis. In Year-1, the scale cuts on cosmic shear data vector are determined by removing any data point where the OWLS-AGN baryonic feedback contribution exceeds 2% [52]. The scales determined by this criterion are then validated by the testing chains. For DES Year-3, I proposed a better-motivated criterion to determine the scale cuts. Instead of the percentage of the baryonic effect contribution, we use the $\Delta\chi^2$ between the dark matter only and baryon contaminated data vector as a measure of the baryonic systematics.

$$\Delta\chi^2_{\rm baryon} = \left(\mathbf{D}_{\rm baryon} - \mathbf{D}_{\rm DMO}\right)^{\rm T} C^{-1} \left(\mathbf{D}_{\rm baryon} - \mathbf{D}_{\rm DMO}\right) \tag{4.12}$$

Schematically, $\Delta\chi^2$ is a measure of the deviation due to certain systematics in the units of statistical uncertainty. This quantity is what directly affects the likelihood thus the

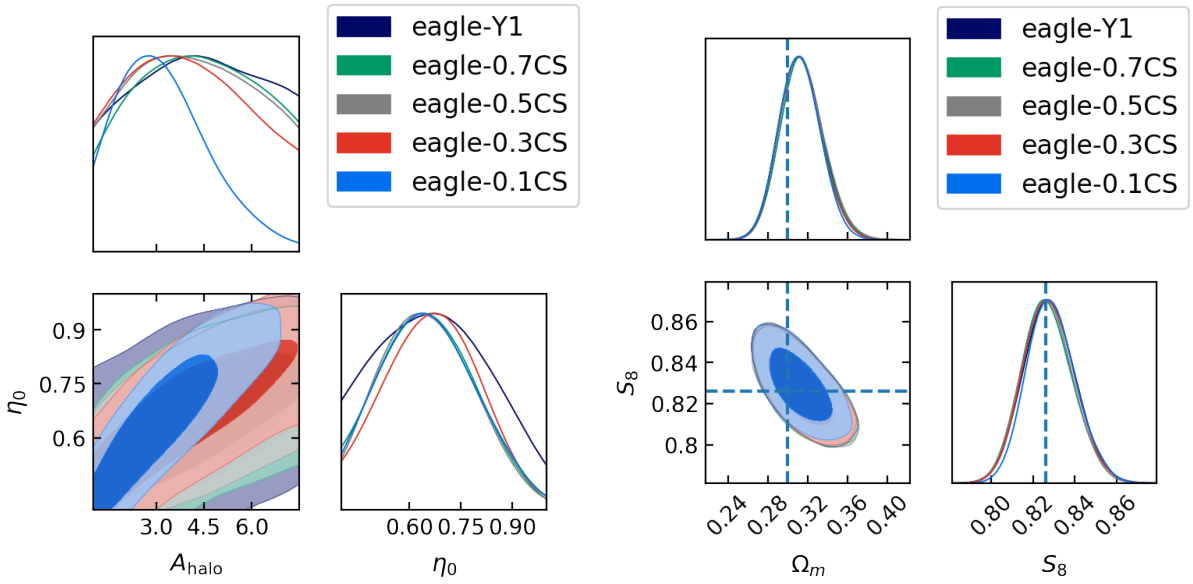

Figure 4.7: The comparison on the constraining power gain pushing to smaller scales between halo parameters and cosmological parameters. The halo parameters, as expected, are very loosely constrained at larger scales because the cosmology there lacks sensitivity to them. When pushing to smaller scales, the figure of merit of halo parameters increases significantly. Meanwhile, for initially well-constrained cosmological parameters, small scale data did not help much. The increase in figure of merit (FoM) $\lesssim 3.0\%$, where the FoM is defined as in [3].

parameter constraints.

We generate scale cuts that restrict the $\Delta\chi^2$ caused by OWLS-AGN baryonic feedback to be smaller than $0.25, 0.5, 1.0, 1.5$ and 2.0, then ran validation tests on them. In the most unfortunate case, regardless of the degrees of freedom of the data vector or the model parameter space, $\Delta\chi^2 = 1.0$ could be projected into $\lesssim 1.0\sigma$ bias on a single parameter. So the limitation on the systematic uncertainty induced $\Delta\chi^2$ should be tested on this order of magnitude regardless of the degrees of freedom. The passing criterion for the chain-run validation tests is that the bias on parameters Ω_m, S_8 and w_0 due to the baryonic effect is smaller than 0.3σ. The scale cuts satisfying this criterion is the $\Delta\chi^2 < 0.5$ one, and it is used for the final cosmic shear only and 3x2pt Year-3 analysis.

Chapter 5

Extended Model Constraints in DES (Original Work)

This chapter is focused on my contribution to DES Year-1 extended model anlaysis in reference [85]. DES Year-1 extended model paper constrained four well-known extensions to ΛCDM models: the curved space, the extra relativistic species, the time-dependent dark energy equation of state, and the modified gravity. My work focused on securing the correct statistics for the cosmological parameter reports in table 5.1, and producing the max a posteriori (MAP) $\Delta\chi^2$ for model comparisons.

5.1 Overview on the DES Year-1 Extended Model Analysis

In this section I briefly introduce the models and the data in the DES Year-1 extended model analysis. The details about the analysis pipeline and the systematics validation can be found in [85]. The fiducial analysis pipeline on which the extension analyses are based on has also been introduced in chapter 4 and appendix A, and the 26 varying parameters of the ΛCDM analysis pipeline are listed in table 4.1 [1].

5.1.1 Extension Models

1. **Curved universe.** In ΛCDM cosmology, we assumed a flat universe as a result of the slow-roll inflation. In this work the departure from zero curvature is characterized

[1] Some center values for the nuisance parameters Gaussian priors are calibrated with the real photo-z data, but they are not very important for the topics here. Interested reader could refer to [85].

by the density parameter of curvature $\Omega_k \in [-0.25, 0.25]$, with flat prior. Ignoring the amount of the radiation in late universe today, we have

$$\frac{H(a)}{H_0} = \left[\Omega_m a^{-3} + (1 - \Omega_m - \Omega_k) + \Omega_k a^{-2}\right]^{1/2} \tag{5.1}$$

The impact of the above equation on the expansion and the structure growth are modeled by Einstein-Boltzmann codes with non-zero Ω_k.

2. **Extra relativistic species.** The Standard Model contains three neutrino species, which are the only (decoupled) relativistic species in the late time in ΛCDM cosmology. As they are thermally produced in the early universe, the abundance of the relativistic species can be calculated from the photon abundance measured from CMB. Given current accurately measured CMB temperature, the number density of the relativistic species is expressed as:

$$n = N_{\text{eff}} \times 113\text{cm}^{-3} \tag{5.2}$$

where N_{eff} the effective number of relativistic species is defined by the above equation. Because the neutrinos are slightly coupled in the $e^{\pm}$ annihilation era, which is the major event determining the photon abundance, the effective non-integer $N_{\text{eff}} = 3.046$ in the Standard Model accounts for this correction. A larger N_{eff} would imply extra species of relativistic particles, for example the sterile neutrinos. In this work, we take a flat prior for $N_{\text{eff}} \in [3.0, 9.0]$.

3. **Dynamical dark energy.** Although in ΛCDM the acceleration of the expansion of the universe is predicted to be caused by the cosmological constant introduced in equation 2.44, so far we do not have much knowledge about the nature of dark energy. Many of the candidate energy-momentum tensor with negative pressure have been studied in the literature. So in the DES Year-1 extension paper, as an extension to ΛCDM cosmology which has $w = -1.0$ constant equation of motion parameter, we investigate a two-parameter equation of motion for dark energy:

$$w(a) = w_0 + w_a(1 - a) \tag{5.3}$$

In such so-called flat w_aCDM cosmology, the Hubble parameter becomes:

$$\frac{H(a)}{H_0} = \left[\Omega_m a^{-3} + (1 - \Omega_m) a^{-3(1+w_0+w_a)e^{-3w_a(1-a)}}\right]^{1/2} \tag{5.4}$$

Again, the Boltzmann code CAMB accepts (w_0, w_a) parametrization, and models the

expansion history and structure growth for us. We set flat priors for $w_0 \in [-2.0, -0.33]$ and $w_a \in [-3.0, 3.0]$.

4. **Modified gravity.** A popular explanation to the accelerated expansion of the universe is modified gravity. There are various formal proposals for the modified gravity [86–88], and for the observation analysis the $\mu - \Sigma$ approximation we adopted below is an efficient description for the majority of cosmologically-motivated gravity theories. In Newtonian gauge, the gravitational perturbation can be characterized by ϕ and ψ (notice that they are subtly different from the Ψ and Φ defined in chapter 2 as Ψ has a different sign):

$$ds^2 = a^2(-(1+2\psi)dt^2 + (1-2\phi)dx^2) \tag{5.5}$$

In general relativity and with no anisotropic stress at late times, $\psi = \phi$. $\mu-\Sigma$ modified gravity is defined by the following generalization of the Poisson equation:

$$k^2\psi = -4\pi G a^2(1+\mu(a))\rho_m\delta_m \tag{5.6}$$

$$k^2(\psi+\phi) = -8\pi G a^2(1+\Sigma(a))\rho_m\delta_m \tag{5.7}$$

For simplicity, we introduce the two extension parameters μ_0 and Σ_0 by the functional form:

$$\mu(z) = \mu_0\frac{\Omega_\Lambda(z)}{\Omega_\Lambda}, \quad \Sigma(z) = \Sigma_0\frac{\Omega_\Lambda(z)}{\Omega_\lambda} \tag{5.8}$$

where $\Omega_\Lambda(z)$ is the time-dependent density parameter of the dark energy, and Ω_Λ is the current value. This way $\mu(z)$ and $\Sigma(z)$ are specified by a total of two extra parameters μ_0 and Σ_0.

We set flat priors on the modified gravity parameters $\mu_0 \in [-3.0, 3.0]$ and $\Sigma_0 \in [-3.0, 3.0]$. The expansion history and the linear perturbations of this extension are modeled by a version of the Boltzmann code modified for the modified gravity, MG-CAMB [2].

5.1.2 Data Sets

We used three of data set combinations to constrain the extension cosmology: DES-only, External-only, and DES+External data sets. Here I briefly introduce each of them.

[2] https://aliojjati.github.io/MGCAMB/mgcamb.html

DES data.

We use the publicly released DES Year-1 "3x2pt" data product including galaxy clustering, galaxy-galaxy lensing and cosmic shear two-point correlation functions described in chapter 4 for our analysis [89]. For the curved space, extra relativistic species, and dynamical dark energy constraints, we use DES Year-1 key paper scale cuts. For the modified gravity tests, we use more stringent scale cuts that only preserve the linear scales. In this case we are left with 334 data points in 3x2pt.

External data.

1. CMB & CMB lensing. In this work we use Planck 2015 CMB likelihoods. We use the Planck TT lite likelihood for multipoles $30 \leq \ell \leq 2508$, and low-multipole $2 \leq \ell \leq 30$ likelihood compiled for TT, EE, BB and TE. We also used the CMB lensing likelihood from temperature map only, for $8 \leq \ell \leq 2048$.

2. BAO + RSD. We use baryonic acoustic oscillation and redshift space distortion measurements of BOSS Data Release 12 [90] . The BOSS DR12 likelihood include the measurements of $H(z_i)$, $d_A(z_i)$ and $f(z_i)\sigma_8(z_i)$ at redshifts $z_i = 0.38, 0.51, 0.61$, with the joint covariance matrix. Here f is the linear growth rate $f \equiv d\ln(D)/d\ln(a)$ of the matter perturbation. We also separately included the measurement of $D_V(z) \equiv [cz(1+z)^2 D_A^2(z)/H(z)]^{1/3}$ and $f\sigma_8(z)$ from 6dF galaxy survey [91] and from SDSS DR7 main galaxy sample [92], at redshift $z = 0.106$ and $z = 0.15$ respectively.

3. Supernovae. In this work we use the binned luminosity distance-redshift measurements for Pantheon SNe Ia sample [93]. The redshift range is between $0.01 < z < 2.3$.

5.2 The Statistical Details in the Analysis

The parameter spaces of cosmological models are usually of very high-dimension and not necessarily Gaussian. For example DES Year-1 ΛCDM analysis has 26 varying parameters and and the $\Omega - \sigma_8$ contour constrained by 3x2pt measurement is banana-shaped. Hence the regression analysis on the cosmological parameters is highly non-linear and need to be carried out by Monte Carlo (MC) techniques. The sampling algorithms that are often adopted include the Metropolis-Hastings algorithms [94] and the nested-sampling algorithms [95, 96]. Metropolis-Hastings algorithms usually save more sample points and make better estimations for the model parameter posterior shapes. On the other hand, nested-sampling algorithms are good at Bayesian evidence calculation, which is a value Metropolis-Hastings algorithms

cannot produce. Despite the way that the samples are randomly drawn from the parameter space, at the end of the day, we need to estimate the probability distribution from the Monte Carlo samples. There are multiple publicly available packages designed for this task, including ChainConsumer[3], GetDist[4], anesthetic[5], etc. We use GetDist for the production of the results in the DES Year-1 extension paper listed in table 5.1. One valuable feature of GetDist is the linear and higher order correction to the kernel in kernel density estimation, as described in detail in subsection 5.2.1. Subsection 5.2.2 discusses max a posteriori $\Delta\chi^2$ interpretation for model comparison.

Curvature	DES Y1	External	DES Y1 + External	$[(\Delta\chi^2)_{\rm DES}, (\Delta\chi^2)_{\rm Ext}, (\Delta\chi^2)_{\rm DES+Ext}]$
Ω_k	$0.16^{+0.09}_{-0.14}$	$0.0023^{+0.0035}_{-0.0030}$	$0.0020^{+0.0037}_{-0.0032}$	$[-0.9, -0.2, -0.1]$
Number Rel. Species	DES Y1	External	DES Y1 + External	$[(\Delta\chi^2)_{\rm DES}, (\Delta\chi^2)_{\rm Ext}, (\Delta\chi^2)_{\rm DES+Ext}]$
$N_{\rm eff}$	< 5.38	< 3.32	< 3.28	$[0.2, 0.4, -0.7]$
Dynamical dark energy	DES Y1	External	DES Y1 + External	$[(\Delta\chi^2)_{\rm DES}, (\Delta\chi^2)_{\rm Ext}, (\Delta\chi^2)_{\rm DES+Ext}]$
w_0	$-0.69^{+0.30}_{-0.29}$	$-0.96^{+0.10}_{-0.08}$	$-0.95^{+0.09}_{-0.08}$	$[-1.9, -0.0, -0.1]$
w_a	$-0.57^{+0.93}_{-1.11}$	$-0.31^{+0.38}_{-0.52}$	$-0.28^{+0.37}_{-0.48}$	
w_p	$-0.91^{+0.19}_{-0.23}$	$-1.02^{+0.04}_{-0.04}$	$-1.01^{+0.04}_{-0.04}$	
Modified Gravity	DES Y1	External	DES Y1 + External	$[(\Delta\chi^2)_{\rm DES}, (\Delta\chi^2)_{\rm Ext}, (\Delta\chi^2)_{\rm DES+Ext}]$
Σ_0	$0.43^{+0.28}_{-0.29}$	$0.26^{+0.14}_{-0.13}$	$0.06^{+0.08}_{-0.07}$	$[-0.2, -3.4, -0.4]$
μ_0	—	$0.16^{+0.43}_{-0.47}$	$-0.11^{+0.42}_{-0.46}$	

Table 5.1: The summary of extended cosmological parameter constraints and the $\Delta\chi^2$ of each extended model comparing to ΛCDM model. The center values are the peak of the 1D marginalized probability density, and the ± values denote the 68% credential level. The $\delta\chi^2$ are reported for DES, External, and DES+External data sets for each extension model's max a posteriori (MAP) parameter comparing to ΛCDM's MAP parameter.

5.2.1 Hard Prior Boundary Strategy for Kernel Density Estimation

To obtain a relatively smooth posterior distribution from the scattered MC chain samples and to infer the credential level from the estimated distribution, we usually use kernel density estimation (KDE) to approximate the marginalized probability density function of a

[3]https://samreay.github.io/ChainConsumer/index.html
[4]https://getdist.readthedocs.io/en/latest/index.html
[5]https://github.com/williamjameshandley/anesthetic

parameter [97]:

$$\hat{f}(x) = \frac{1}{n}\sum_{i=1}^{n} K_h(x - X_i) \tag{5.9}$$

where X_i are the sampled parameter sequences in the chain, n is the total number of the samples in the chain, x is an arbitrary parameter sequence, and $K_h(x - X_i)$ is the kernel function. K_h is usually chosen to be the Gaussian function centering at zero with width parameter h, for example in the ChainConsumer codes. By tuning h, Gaussian kernel is sufficient to approximate the 1D marginalized posterior shapes in most of the cases. However, as pointed out in [97], the symmetry of the Gaussian kernel brings in a caveat when the posterior is cut off by the hard boundary of the prior. The simplest solution is to use a non-symmetric kernel [98] for KDE, and the first order correction of the non-symmetric kernel takes the form:

$$K'_h(x) = K_h(x)(A_0 + A_1^a x_a + ...) \tag{5.10}$$

where x_a is each individual parameter of the parameter vector (sequence) x.

The linear correction to KDE has important effects when our constraint on an extended cosmological parameter pushes against the hard boundary. For example in figure 5.1, DES and DES+external data constrain $N_{\rm eff}$ down to the Standard Model lower bound 3.0 for three neutrino species. The right panel is the old version of the plot made by the ChainConsumer code, which was the default for the DES Year-1 key paper. Because it only uses the symmetric kernel for KDE, the peaks of the marginalized posterior for $N_{\rm eff}$ constrained by external and DES+external data are biased away from the boundary. Even worse, the $1-\sigma$ credential level for DES sets a fake lower bound for $N_{\rm eff}$. The symmetric kernel wrongfully estimates a non-zero probability density across the hard boundary set by the prior, so the marginalized 1D peak of the probability is biased to the right of the boundary. In contrast, the left panel is the result from GetDist using the linearly corrected kernel. We see that the marginalized posterior estimation by GetDist concretely respected the hard boundary set by the prior. As shown in table 5.1, we also obtain only the upper bound of the $N_{\rm eff}$ for all the data sets as it should be. So getting the symmetry of the KDE right is not just a trivial choice that only affects the aesthetics of the plot, it indeed affects the robustness of the credential level reports when the posterior is pushing against the prior boundary.

In fact, the finding on $N_{\rm eff}$ constraint has warned us that we should always use higher order corrected kernel for KDE no matter if we were seeking an upper bound or not. To avoid a priori bias, most of the cosmological surveys practice blinding nowadays. We only noticed our wrong-doing on $N_{[\rm eff]}$ because of our a priori knowledge here, which is a little bit harmful to the blindness. The real data in principle have the possibility to (surprisingly)

constrain any cosmological parameters against our a priori knowledge, especially at present time when various tensions are showing up between surveys. So we should make sure to evolve or abandon the outdated codes that only implemented the simplest KDE process.

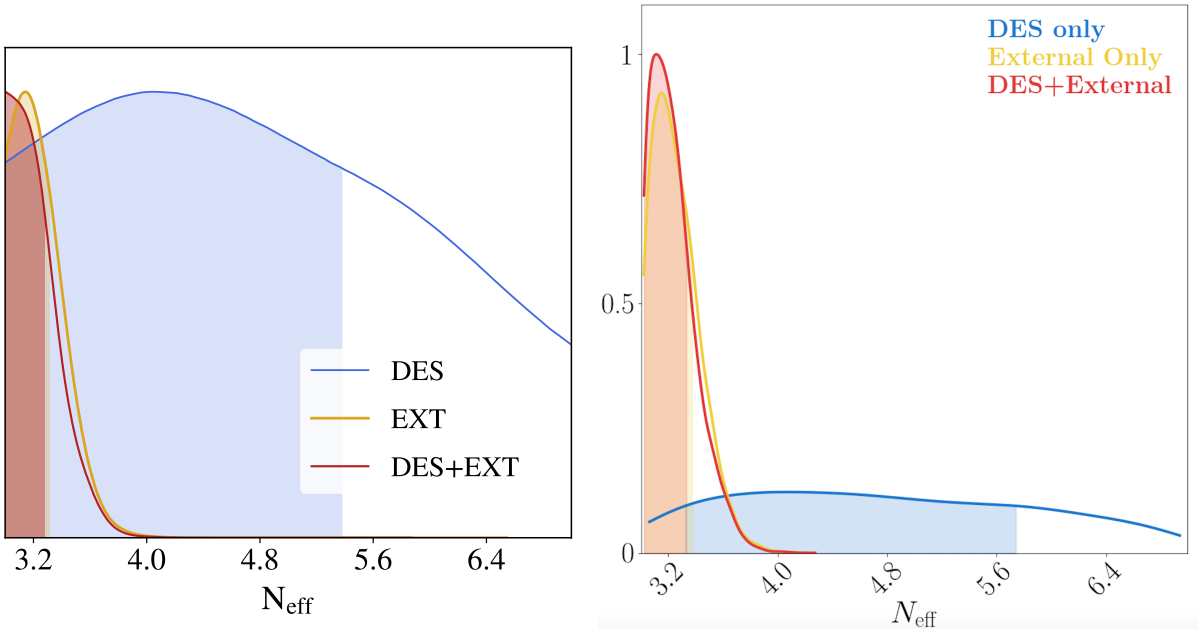

Figure 5.1: The constraints on the effective number of the relativistic species $N_{\rm eff}$ using DES, External, and DES+External data sets. Both panels used the same three Monte Carlo chains as labeled in the legend. Left panel: the $N_{\rm eff}$ constraints analyzed by GetDist. Here the KDE kernel adopted the linear correction in equation 5.10, thus was able to approach the non-symmetric probability density distribution near the boundary of $N_{\rm eff} = 3.0$. Right panel: the old plot made by ChainConsumer KDE, which only has Gaussian kernel. The different normalization is only a plotting choice. Near the boundary, the symmetric Gaussian kernel failed to resume the peak of the probability distribution at the boundary.

5.2.2 MAP $\Delta\chi^2$ Model Comparison

Other than the constraints on the extended parameters, another important answer we are seeking in the extension model analysis is how good these extended models fit to the data, comparing to ΛCDM. This will give us a metric of the "goodness" of our model at describing the real universe. In chapter 6, we will see several more advanced statistical metrics for the purpose of model comparison, but due to the variety of the models studied at the same time in the DES extension paper, we kept things simple to the most widely used max a posteriori $\Delta\chi^2$ comparison between extension models and ΛCDM model.

Suppose $\chi^2_{\rm A,MAP}$ and $\chi^2_{\rm B,MAP}$ are the χ^2 for all combined likelihoods at the max a posteriori

sample point in the Monte Carlo chain run for model A and the chain for model B,

$$\Delta\chi^2 = \chi^2_{\mathrm{A,MAP}} - \chi^2_{\mathrm{B,MAP}} \tag{5.11}$$

If $\Delta\chi^2 < 0$, it means that in the parameter space of model A we can find a better fit to the data vector than the parameter space of model B. It does not conclusively say that model A is better than model B, because $\Delta\chi^2$ needs to be punished by extra degrees of freedom to serve as reliable model comparison metric, like Akaike information criterion (AIC) or Bayesian information criterion (BIC). The $\Delta\chi^2$ in table 5.1 reported for the four extended models are so small that we do not need further effort to recognize that none of the models tested here is a sufficiently better fit than ΛCDM for either DES, External, or DES+External data sets. This is expected given the extension parameter constraints are not violating the ΛCDM default values: $\Omega_k = 0, N_{\mathrm{eff}} = 3.046, w_0 = -1.0, w_a = 0.0$, and $\Sigma_0 = 0.0, \mu_0 = 0.0$; See table 5.1. Chances still exist when the constraints on these extended parameters get tighter with future higher-precision measurements.

Some subtleties I want to mention here are the details in how we obtain the MAP χ^2, as it was widely acknowledged as the first glance on model comparison issues. Again, remember that we are trying to estimate the properties of a smooth posterior distribution from the scattered MC samples. Especially when we are using the nested samplers, which typically has $\mathcal{O}(10)$ times less sample points than the Metropolis-Hasting samplers, the sparsity of the scatters in the very high dimensional parameter space makes it very difficult to read out the maximum posterior directly from the sampled points. We need to run an optimizer on the maximum posterior point iteratively to reach a better estimation of the MAP point. In DES Year-1 extensions we used the maxlike sampler in cosmosis to achieve a stable MAP posterior value. In this process, we saw an improvement of posterior ~ 0.5 from the sampled point value to the maxlike value. The drifting of MAP parameters could also reach several $\mathcal{O}(0.1)\sigma$. All of this points to the fact that MAP point might have larger degeneracy and uncertainty in the parameter space than one might presume due to the highly nonlinear correlations between the parameters. Hence the N-dimensional space single-point MAP values should not be read into as conclusively as the marginalized quantities, like mean values and credible intervals, which are more statistically stable.

Chapter 6

Dark Matter to Dark Radiation Conversion Model (Original Work)

This chapter is based on paper [34]. Although the main-body of the paper was proposed, investigated, and written by myself, this work is definitely completed by the joint effort of many people in the DES collaboration, as shown in the author list of the paper. The contribution from the DES Year-1 extension group that validated the default analysis pipeline is especially indispensable to this work.

6.1 Introduction

Over the past few years, there has been a notable improvement in both the variety and precision of cosmological probes. Signals predicted long ago, such as gravitational waves and global 21-cm absorption, were finally observed, providing new insights and solidifying our understanding of the universe. The enhanced precision of relatively mature observational techniques such as measurements of galaxy clustering, weak lensing, and anisotropies in the cosmic microwave background (CMB) temperature and polarization fields has allowed us to test the ΛCDM paradigm to an unprecedented degree.

Recent cosmological observations have revealed a discrepancy in the inferred Hubble constant at $\gtrsim 4\sigma$ level between early- and late-universe probes [44, 45, 99]. With a strengthening of the various steps in the local distance-ladder measurements of H_0, as well as tightening constraints of medium-to-high redshift probes such as strong and weak gravitational lensing, the Hubble tension is becoming more significant [100–103] and enormous effort has been devoted to understanding its origin. A number of theories have thus far been proposed to help ameliorate or resolve the tension [104–114], but so far none have done so to a satisfactory degree.

A parallel development over the last few years has been the consistently lower value of the amplitude of mass fluctuations σ_8 measured in gravitational lensing compared to that measured by the CMB experiments [55, 89, 115–118]. While not currently statistically as strong as the Hubble tension, the persistence of the σ_8 measurement discrepancies, as well as their possible origin as a mismatch between the geometrical measures and the growth of structure expected in the currently-dominant ΛCDM paradigm, deserves special attention. It would be very exciting, and compelling, if both the H_0 and σ_8 tensions were solved simultaneously, though the success of extant models on this front is at best mixed [119–124].

One possible explanation for why weak lensing surveys measure a smaller amplitude of fluctuations than the CMB is that the present-day matter content has decreased at a higher rate than predicted by ΛCDM model. Models where dark matter converts into a new species with radiation properties that is not directly detectable (hence 'dark radiation') can enable such a trend. These models also have the potential to reconcile the Hubble tension, as they predict a smaller matter content as time evolves. Accordingly, dark energy dominates faster than in ΛCDM in these models, giving a larger late-time acceleration rate (indicated by a higher H_0). Therefore, decaying or annihilating dark matter models, such as those studied previously in Refs. [125–142], offer a tantalizing hope of resolving the H_0 and σ_8 tensions simultaneously.

In this paper, we are specifically interested in the class of models where the energy density in dark matter monotonically converts into dark radiation, with the bulk of the activity happening at low redshift (late time). Our motivation is to investigate whether a model where dark matter converts to dark radiation — henceforth, a **DMDR** model — can satisfy the twin requirements of both being favored by the data and helping alleviate the Hubble and σ_8 tensions.

In general, interacting dark matter models have the potential to resolve some observations in cosmology that might be otherwise difficult to explain in the standard ΛCDM model. Because models with beyond-cold-dark-matter particle content often wash out small-scale structure [143,144], they are well positioned to help alleviate the well-documented challenges observed on small scales (the core/cusp, missing-satellites and too-big-to-fail problems of CDM [145]). The Integrated Sachs–Wolfe (ISW) effect has been measured to have an amplitude significantly higher than that predicted in ΛCDM when stacking large voids in the large-scale structure [146, 147]; the decrease of dark matter would suppress the Weyl potential on large scales, thus enhancing the ISW effect and could thus help to explain this. Finally, cosmic rays from unidentified sources, specifically the galactic positron excess at $\sim$ 300 GeV [148] and the $\sim$3.5 keV [149] X-ray line from nearby galaxies, have been hypothesized to be sourced by the decay of dark matter [150–154] (although they may be inconsistent

with some specific dark matter particle models [155, 156]). All of these lines of inquiry motivate further study of the properties of, and constraints on, the DMDR conversion classes of models. For example, Wang et al. [150, 157] investigated a decaying dark matter model that could be mapped into the parameter space of the phenomenological DMDR conversion scenario studied in this paper, and showed that their model can mitigate some of the aforementioned small-scale CDM challenges.

On the theory side, dark matter – dark radiation conversion is predicted in various physically-motivated scenarios [133, 158, 159]. In particle-dark-matter theories, an unstable dark matter component is predicted in various extensions of the Standard Model. For example, in non-minimal supersymmetric models, the dark sector has a spectrum of particles analogous to particles in the Standard Model, and heavier particles can decay into the lightest supersymmetric particle [160] which could have the relativistic and nonreactive-to-visible-matter properties of dark radiation [161] (equivalent to sterile neutrino). In some other cases, supersymmetric sectors directly include bosons like dark photons. More generally, beyond-Standard-Model physics including fifth-force type additional interactions can naturally accommodate dark matter and dark radiation couplings. Some have proposed such coupled models as a mechanism to solve the 21 cm absorption anomaly seen by the EDGES experiment [47, 162]. Furthermore, inspiraling and colliding primordial black holes (PBHs) — dark-matter candidates in their own right [163] — could transfer energy from dark matter to gravitational waves, which are also a form of dark radiation [136, 164]. PBHs could also evaporate into beyond-standard-model relativistic species through Hawking radiation [165]. Various constraints on PBH abundance were extensively studied by the dynamical, lensing, evaporation and accretion footprints of the PBHs [163, 166], but several mass windows remain unconstrained, and previously 'closed' windows sometimes re-open when revisited with improved analysis tools [167–169].

Any of the aforementioned theoretical models could underlie a phenomenological dark matter-dark radiation conversion model. The key signature of such a model, compared to the standard ΛCDM model, is the decreased fraction of dark matter in favor of both dark radiation and dark energy.

Our goal is to study a phenomenological cosmological DMDR model using the state-of-the-art cosmological observations. In this work we utilize the CMB temperature, polarization, and lensing potential angular power spectra measured by Planck [99], together with type Ia supernovae from Pantheon [93], baryon acoustic oscillations (BAO) from the BOSS [90], MGS [92], and 6dFGS [91] surveys, and tomographic galaxy clustering and weak lensing measured by the Dark Energy Survey (DES) [89].

This work is presented as follows. We introduce our DMDR model in section 6.2, stressing

its signatures in the CMB and matter power spectrum. In section 6.3, we present the details of our analysis pipeline, including the datasets we use and the theoretical predictions of the DMDR model. In section 6.4, we report combined constraints on the DMDR model from DES-Y1 and external data, along with model comparison between DMDR and ΛCDM. We conclude in section 6.5.

6.2 The DMDR model

Our specific implementation of the dark matter – dark radiation conversion model is based on the phenomenological model studied by Bringmann et al. [136], hereafter B18. We focus on the case where the conversion process accelerates in time, and the major departures from ΛCDM happen at late times, as shown in figure 6.1. To obtain a phenomenological model with this behavior, we impose an additional boundary condition onto the original B18 three-parameter ansatz to obtain a steeper rate of dark matter conversion in the recent past ($z \lesssim 10$); see the next subsection. Overall, our DMDR model introduces two additional parameters compared to ΛCDM.

We now describe the background equations for the model, followed by the description of its perturbations.

6.2.1 Background Equations

The background evolution of the DMDR model is specified by the ansatz of the decreasing dark matter density and the modified continuity equation

$$\rho_{\rm dm}(a) = \frac{\rho^0_{\rm dm}}{a^3}\left[1+\zeta\frac{1-a^\kappa}{1+\zeta a^\kappa}\right] \tag{6.1}$$

$$\frac{1}{a^3}\frac{d}{dt}(a^3\rho_{\rm dm}) = -\frac{1}{a^4}\frac{d}{dt}(a^4\rho_{\rm dr}) = -\mathcal{Q} \tag{6.2}$$

where $\rho_{\rm dm}$ and $\rho_{\rm dr}$ are dark matter and dark radiation energy densities, $\rho^0_{\rm dm}$ is the dark matter density today, a is the scale factor, and we introduce two new parameters[1]:

1. ζ, the total amount of dark matter that has already converted into dark radiation, divided by the amount of dark matter at current time.

[1]The original ansatz in B18 has three parameters: ζ, κ, a_t, where the last parameter is the characteristic scale factor when the conversion happened. Here we set the mathematical condition $\rho_{\rm dm}a^3 = 0$ as $a \to \infty$ to obtain an accelerated decreasing curve near $a = 1$. This condition leads to an identity among the three parameters, $1 - \zeta a_t^\kappa = 0$. We then substitute $a_t = \exp(-\log(\zeta)/\kappa)$ back into the B18 ansatz, arriving at our equation (6.1) which contains the remaining parameters ζ and κ. Keeping ζ or a_t in our model is equivalent; we made the choice based on the fact that ζ is a more physically intuitive parameter in this case.

2. κ, the parameter characterizing the conversion rate. The duration of the conversion roughly corresponds to $O(1/\kappa)$ orders of magnitude change in the scale factor.

Equation (6.1) provides an ansatz for the time evolution of the comoving density of dark matter. In our late-time DMDR conversion model, the bulk of the conversion occurs around the present time ($a \simeq 1$). Equation (6.2) specifies that the energy transfers from dark matter to dark radiation. It also determines the energy transfer flux, $\mathcal{Q}$, as a function of the scale factor a, taking the derivative of equation (6.1).

Like the original B18 model, our DMDR model has the generality to cover a wide class of decaying/annihilating dark matter models. For most of the popular decaying/annihilating dark matter models with smooth and simple transition curve, in the $a < 1$ region a specific value of κ that numerically mimic the transition curve of the dark matter density can be found. Note, since the condition of accelerating conversion rate in the near past is similar to pushing the transition time (labeled by the maximum dark-matter conversion rate) to the future, in the single-body decaying dark matter scenario it suggests a very small decay rate, $\Gamma \ll H_0^{-1}$.

To illustrate the evolution of background quantities, we first discuss the fiducial cosmological model. We fix the non-DMDR cosmological parameters to the following values based on DES-Y1 fiducial values: matter and baryon densities relative to critical $\Omega_{\rm m} = 0.3028$ and $\Omega_{\rm b} = 0.04793$, scaled Hubble constant $h = 0.6818$, spectral index and amplitude of primordial density fluctuations $n_s = 0.9694$ and $A_s = 2.198 \times 10^{-9}$, physical neutrino density $\Omega_\nu h^2 = 0.0006155$ (corresponding to the sum of the neutrino masses of 0.058 eV), and optical depth to reionization $\tau = 0.06972$. These parameters, which are common to both DMDR and ΛCDM models, are also adopted in the illustrations and Fisher forecasts throughout the following sections. We stress that the values of the standard cosmological parameters such as h and $\Omega_{\rm m}$ are by definition set at the present time. Thus the high-z region of the DMDR models in these figures has higher dark matter density. The detailed effect of the DMDR parameters ζ and κ is illustrated in the first batch of Figures in this paper, which we now describe.

Figure 6.1 shows how the density of dark matter evolves with scale factor, relative to ΛCDM, for different conversion rates. Varying ζ scales the curves up and down; in the illustrative plots that follow we choose $\zeta = 0.1$. We show the matter density evolution for four different values of the conversion rate κ; results in figure 6.1 and subsequent figures shows rapid changes in the dark matter density in $a \gtrsim 0.1$, suggesting that we may be able to place constraints on such models using current LSS observations.

Figure 6.2 shows how the density of dark radiation evolves with scale factor for different conversion rates, relative to ΛCDM. As the conversion rate parameter κ increases, the density

of dark radiation in the late universe increases faster. When the dark radiation is produced in the nearer past (for higher κ), it dilutes less than if produced over a longer span of time (lower κ); thus there is more dark radiation at $a = 1$ in a larger-κ universe. One may worry that large-κ models may be automatically ruled out because they apparently lead to a high number of effective relativistic species $\Delta N_{\rm eff} = \rho_{\rm dr}/\rho_\nu$, but note that the conversion to dark radiation happens at very low redshifts in our DMDR model and thus renders a simple comparison with $\Delta N_{\rm eff}$ constraints derived from the CMB impossible. Hence a detailed analysis of the combination of CMB, LSS and geometric probes is necessary. A more direct impact of dark radiation will be on the expansion history, however, and this will be constrained by the supernova data in our analysis. For the hypergeometric function required to calculate the background density of the dark radiation, we used the special function routine by Shanjie Zhang and Jianming Jin [170].

Figure 6.3 shows how the Hubble expansion rate evolves with scale factor for different conversion rates, relative to ΛCDM. Note that we implicitly hold the present-day values of Ω_m and h constant in this plot. Then, increasing the conversion rate of dark matter κ *increases* the amount of dark matter at $a < 1$ relative to today, and hence leads to a more rapid expansion rate, so that $H^{\rm DMDR}(a)/H^{\rm LCDM}(a) > 1$ as seen in figure 6.3.

6.2.2 Perturbation Equations

In order to get the matter and radiation perturbation power spectra, we next need to write down the linear perturbation equations of motion for both dark matter and dark radiation, then implement them in the Boltzmann numerical solver CAMB [171]. We adopt the synchronous gauge throughout this section, following the convention of CAMB. The metric perturbation in synchronous gauge is [172]:

$$ds^2 = a^2(\tau)[-d\tau^2 + (\delta_{ij} + h_{ij})dx^i dx^j], \tag{6.3}$$

where τ is the comoving time, and h_{ij} with $i, j = 1, 2, 3$ is the metric perturbation.

Most often, dark radiation is treated as a new species of massless neutrinos (e.g. [136, 173]). This conjecture works fine in the scenario with no massive neutrinos, but it produces an incorrect matter power spectrum that evolves discontinuously away from ΛCDM when *massive* neutrinos are present. Such behavior is expected because dark radiation (unlike the massless neutrinos) does not interact with massive neutrinos nor does it share the same temperature and entropy with them. In CAMB, the distribution of the energy between neutrino species are specified by a set of time-independent degeneracy numbers, but this is not

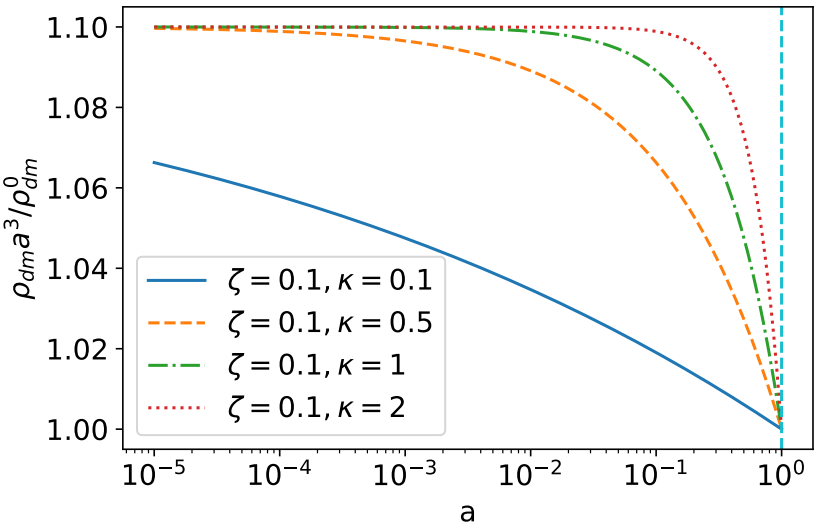

Figure 6.1: Temporal evolution of the comoving dark matter density (in units of current dark matter density $\rho^0_{\rm DM}$. The legend shows the assumed values of ζ, the fraction of dark matter that has converted into dark radiation since the early universe relative to current density, and κ, the conversion rate of dark matter. We fixed the standard cosmological parameters to their fiducial values as reported in section 6.2.1.

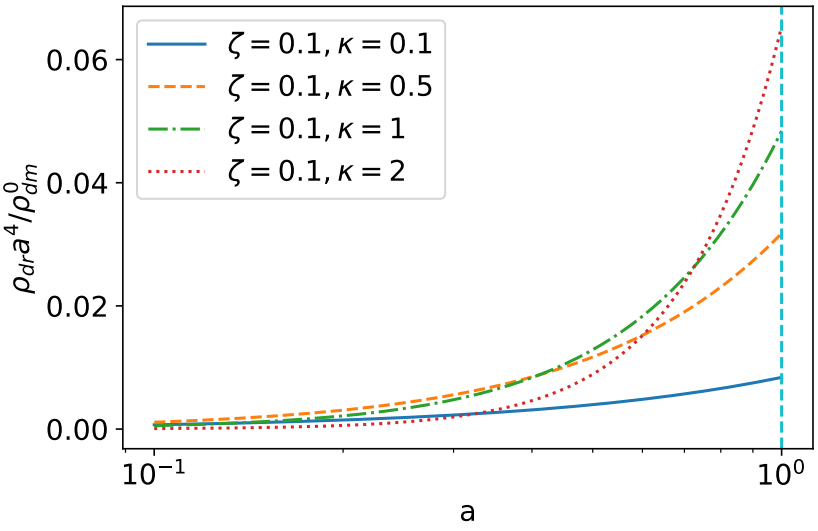

Figure 6.2: Same as figure 6.1, but now showing the temporal evolution of the dark *radiation* density.

applicable to the model with energy transfer from dark matter to dark radiation.[2] Therefore,

[2]In the all-massless neutrino case the problem of incorrect time-independent degeneracy numbers could be hidden, because there is no need to partition the energy for the massless species sharing the same equation of motion.

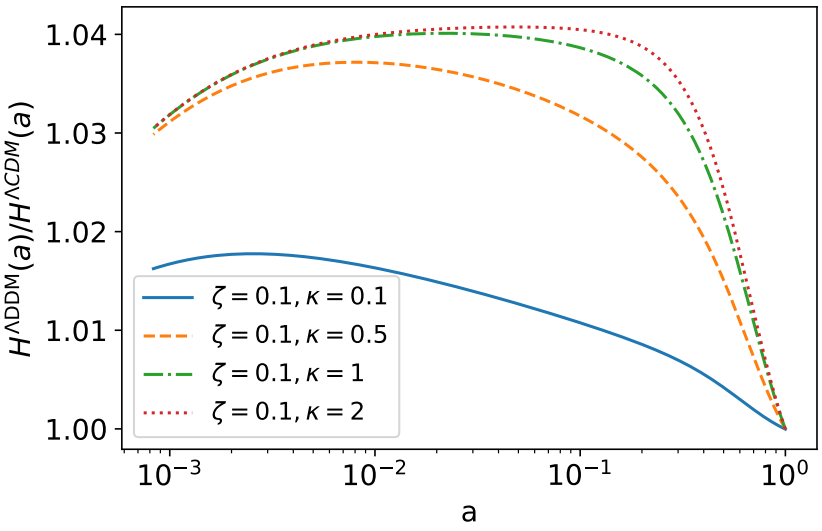

Figure 6.3: Same as figure 6.1, but now showing time evolution in the ratio between DMDR and ΛCDM Hubble parameter.

as long as the model does not allow for dark matter to massless neutrino conversion, the two species are physically distinct and treating dark radiation as a new type of a massless neutrino is incorrect. Thus we choose to treat dark radiation as an independent perturbation component in the Boltzmann equations.

In our model, we assume the dark matter to always be cold, meaning that the conversion process to the dark radiation does not provide enough recoil kinetic energy to heat up the dark matter. At the same time, dark radiation in our model does not self-interact or dissipate energy via interactions with dark matter, standard-model particles, or photons after their production, so that dark radiation simply free-streams. As a result, the phase-space perturbation equations for the dark radiation differ from the massless-neutrino ones only by a collision term. Adopting the perturbation-expansion notation from [172], we have

$$dN = f(x^i, P_j, \tau) dx^1 dx^2 dx^3 dP_1 dP_2 dP_3 \tag{6.4}$$

$$f(x^i, P_j, \tau) = f_0(q) \left[1 + \Psi(x^i, q, n_j, \tau)\right] \tag{6.5}$$

$$F(\vec{k}, \hat{n}, \tau) = \frac{\int q^2 dq q f_0(q) \Psi(\vec{k}, q, \hat{n}, \tau)}{\int q^2 dq q f_0(q)} \tag{6.6}$$

where x^i are comoving coordinates, P_i are their conjugate momentum, dN is the particle number in the phase space differential volume. Here the momentum variable P_i is replaced by q and n_i variables through $P_i = (\delta_{ij} + \frac{1}{2}h_{ij})qn_j$ in the second equation, and k-space is

Fourier transformed from x-space.

The dark radiation phase-space equation of motion reads

$$\begin{aligned} \frac{\partial F_{\rm dr}(\vec{k},\hat{n},\tau)}{\partial\tau} &+ ik\mu F_{\rm dr}(\vec{k},\hat{n},\tau) = -\frac{2}{3}\dot{h}(\vec{k},\tau) \\ -\frac{4}{3}(\dot{h}(\vec{k},\tau) &+ 6\dot{\eta}(\vec{k},\tau))P_2(\hat{k}\cdot\hat{n}) + \left(\frac{\partial F_{\rm dr}(\vec{k},\hat{n},\tau)}{\partial\tau}\right)_C, \end{aligned} \tag{6.7}$$

where $(\partial F_{\rm dr}(\vec{k},\hat{n},\tau)/\partial\tau)_C$ is the additional collision term due to the conversion between dark matter and dark radiation, to be contrasted with the collisionless massless neutrino equations.

We adopt a simple form for the collision perturbation equation involving no dependence on polarization or momentum anisotropy. Specifically,

$$\left(\frac{\partial F_{\rm dr}(\vec{k},\hat{n},\tau)}{\partial\tau}\right)_C = \frac{\mathcal{Q}(a)a}{\rho_{\rm dr}(a)}(-F_{\rm dr}(\vec{k},\hat{n},\tau) + \delta_{\rm dm}(\vec{k},\tau)). \tag{6.8}$$

where $\mathcal{Q}$ is defined in equation (6.2). When writing down the equation (6.8), we adopted the minimal form for the perturbation variation of the conversion term $\mathcal{Q}$:

$$\delta\mathcal{Q} = \mathcal{Q}\delta_{\rm dm}. \tag{6.9}$$

In principle, the form of $\delta\mathcal{Q}$ is determined by the microphysics of the dark matter-dark radiation conversion process. The minimal form above has been adopted by previous literature [134, 135, 174], and B18 has demonstrated that the current generation cosmology observations do not have high enough precision to distinguish the detailed $\delta\mathcal{Q}$ perturbation, by carrying out case studies on Sommerfeld enhancement and single-body decay process.

After harmonic expansion of equation (6.7), we get the hierarchy equations for dark radiation. Along with the dark matter perturbation equations, the full set of perturbation equations in DMDR model reads [172, 173, 175, 176]:

$$\delta'_{\rm dm} + k\mathcal{Z} = \frac{a}{\bar{\rho}_{\rm dm}}(\mathcal{Q}\delta_{\rm dm} - \delta\mathcal{Q}) = 0 \qquad \text{[Dark Matter]} \tag{6.10}$$

$$\delta'_{\rm dr} = -\frac{4}{3}k\mathcal{Z} - kq_{\rm dr} - \frac{a\mathcal{Q}}{\bar{\rho}_{\rm dr}}(\delta_{\rm dr} - \delta_{\rm dm}) \qquad \text{[Dark Radiation, } \ell = 0] \tag{6.11}$$

$$q'_{\rm dr} = \frac{k}{3}\delta_{\rm dr} - \frac{2}{3}k\beta_2\pi_{\rm dr} - \frac{a\mathcal{Q}}{\bar{\rho}_{\rm dr}}q_{\rm dr} \qquad \text{[Dark Radiation, } \ell = 1] \tag{6.12}$$

$$\pi'_{\rm dr} = \frac{2}{5}kq_{\rm dr} - \frac{3}{5}k\beta_3 J^{\rm dr}_3 + \frac{8}{15}k\sigma - \frac{a\mathcal{Q}}{\bar{\rho}_{\rm dr}}\pi_{\rm dr} \qquad \text{[Dark Radiation, } \ell = 2] \tag{6.13}$$

$$J^{\rm dr\prime}_\ell = \frac{k}{2\ell+1}[\ell J^{\rm dr}_{\ell-1} - \beta_{\ell+1}(\ell+1)J^{\rm dr}_{\ell+1}] - \frac{a\mathcal{Q}}{\bar{\rho}_{\rm dr}}J^{\rm dr}_\ell, \text{[Dark Radiation, } \ell > 2] \tag{6.14}$$

where J_ℓ are the harmonic expansions of the phase space perturbation, $J^{\rm dr}_0 \equiv \delta_{\rm dr}$, $J^{\rm dr}_1 \equiv q_{\rm dr} = \frac{4}{3}\theta_{\rm dr}/k$, $J^{\rm dr}_2 \equiv \pi_{\rm dr} = \Pi^{\rm dr}/\bar{\rho}_{\rm dr}$ in CAMB convention; $\mathcal{Z}$ and σ are the metric perturbation coefficients, and β_ℓ are the harmonic expansion coefficients of the gradient operator defined in reference [173]. Further details of this derivation are included in Appendix B.2.

The modifications described above are relevant for the continuity equations. For the Einstein equations, the correction is rather straightforward: we simply add the dark-radiation perturbations to the total energy-momentum perturbations.

6.2.3 CMB and Matter Power Spectrum

We now have the ingredients necessary to numerically compute the CMB polarized temperature anisotropies and matter perturbation power spectra, and thus derive the observable quantities that can be compared to data. We implement the background and perturbation equations in the previous two subsections in the Einstein–Boltzmann code CAMB [171] which is used in the `cosmosis` pipeline that we discuss in more detail below.[3]

Figure 6.4 illustrates the relative differences between the DMDR and ΛCDM matter power spectra and their CMB spectra. As with the background-evolution illustrations above, we fix the parameters common to both DMDR and ΛCDM model to their fiducial values listed in section 6.2.1, and we only vary DMDR-specific parameters ζ and κ. This ensures that the two cosmologies always converge at late times (see also figure 6.1). In the early universe, DMDR has more dark matter than ΛCDM, and this makes the matter and CMB power spectra resemble those in a ΛCDM cosmology, but with more dark matter. This, in turn, shows up as the small-scale power enhancement, as well as the phase shift in the case

[3]DMDR-CAMB using the background and perturbation equations in this work can be found here: https://bitbucket.org/anqich/ddm-camb/src/master/. Please email the corresponding author to get access if it is needed.

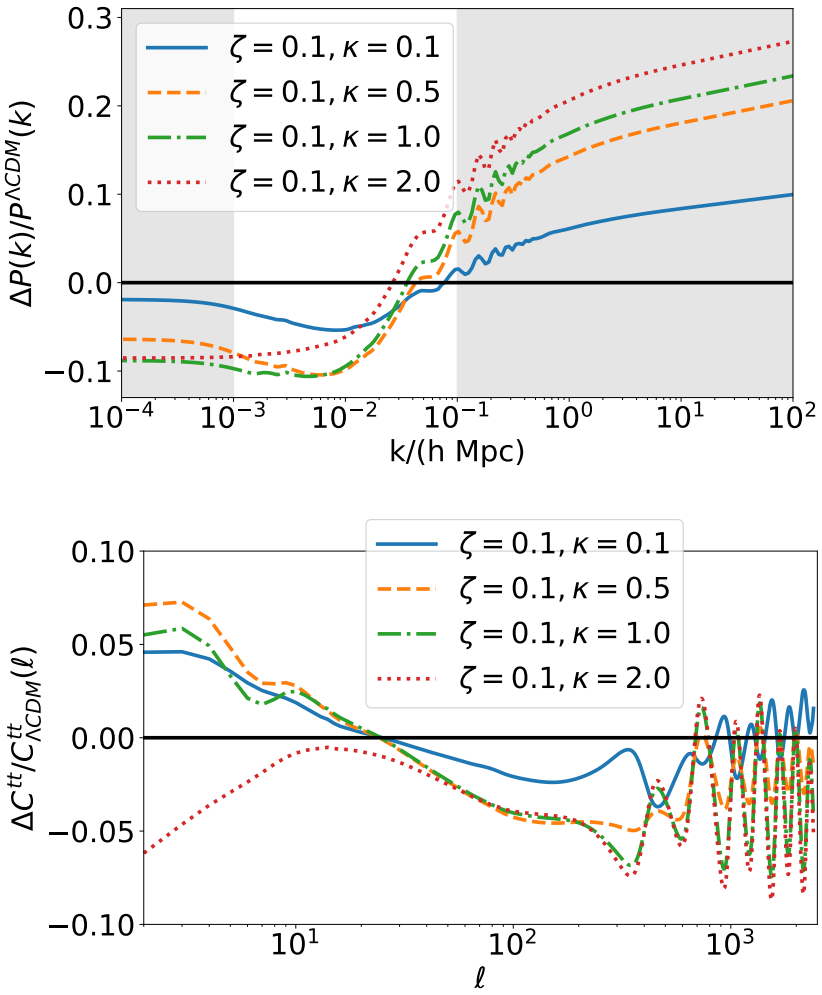

Figure 6.4: Relative difference in the matter power spectrum (upper panel) and CMB TT spectrum (lower panel) between DMDR and ΛCDM. We explore the same four sets of (ζ, κ) values as in the previous three figures. In the left panel, the white region (between the two shaded regions) denotes roughly the scales used by the DES 3x2pt analysis.

of the CMB power spectrum.

A distinctive feature in DMDR is the dip in the matter power spectrum at $k \sim 10^{-2}$, the scale corresponding to the horizon crossing at matter–radiation equality. This feature is mostly due to the different expansion history in a higher dark-matter density universe in DMDR. Although we see an increase in the matter power around $k \sim 0.1h$/Mpc, and might worry that it could boost the amplitude of mass fluctuations σ_8 and thus exacerbate the LSS tension with CMB, note that this is not the case because we have artificially held most of the cosmological parameters fixed. In fact, DMDR can be qualitatively compared and contrasted with the early dark energy (EDE) models [105, 122]. While the EDE models

which have a larger dark-matter-to-dark-energy ratio after recombination than ΛCDM, the DMDR model have a *smaller* such ratio relative to ΛCDM. This works in the direction of reconciling the σ_8 tension.

In the CMB temperature power spectrum shown on the right in figure 6.4, the decreasing dark matter density leads to an increase in the late integrated Sachs–Wolfe (ISW) effect caused by the decrease of the gravitational potential as dark matter converts into dark radiation (an exception is the $\kappa = 2$ case which we discuss separately below). Late-ISW effect is caused by the decrease of Weyl potential in the dark-energy-dominant epoch as the expansion of universe accelerates. In ΛCDM, the decrease of the Weyl potential only happens in the dark-energy-dominated epoch while the potential remains constant in dark matter epoch, but in the DMDR model the late-ISW effect also accumulates in the dark-matter-dominated epoch. This is because the Weyl potential is mainly contributed to by dark matter and a decreasing comoving density of dark matter leads to a decreasing Weyl potential even before dark energy takes over. Although DMDR imprints in the late-ISW effect are probably buried in the cosmic variance, it does gives these models an additional signature that can be sought in e.g. studies of the ISW imprints in the large voids [147].

The red curve in figure 6.4 requires further discussion. This is the case where the dark matter converts at very late times ($z \simeq O(1)$) and rapidly. Therefore, the increased dark-energy-to-dark-matter ratio that is characteristic of DMDR model occurs too late for the late-time ISW to fully benefit from it. In addition, a DMDR model with the same present-day Ω_m as a ΛCDM model has more matter relative to dark energy at $z > 0$; therefore, contributions to late-time ISW occur later in DMDR than in ΛCDM. These two effects combine to severely suppress the late-time ISW effect in high-κ DMDR models.

Lastly, we also present the DMDR effect on the lensing potential power spectrum for CMB; see figure 6.5. We observe an increase of the lensing potential at small scales (large multipoles L) that mimics the amplified large k modes of matter power spectrum seen in figure 6.4.

6.2.4 Nonlinear Matter Power Spectrum Strategies and DES-Y1 Scales Used

Obtaining accurate theoretical predictions for nonlinear clustering in cosmological models outside of ΛCDM is typically challenging, as these predictions require running suites of cosmological simulations designed specifically for the extended models. This situation can be contrasted to that in ΛCDM (and its simplest extension that assume a free but constant dark energy equation of state, wCDM), where the modeling of nonlinear matter power spectrum

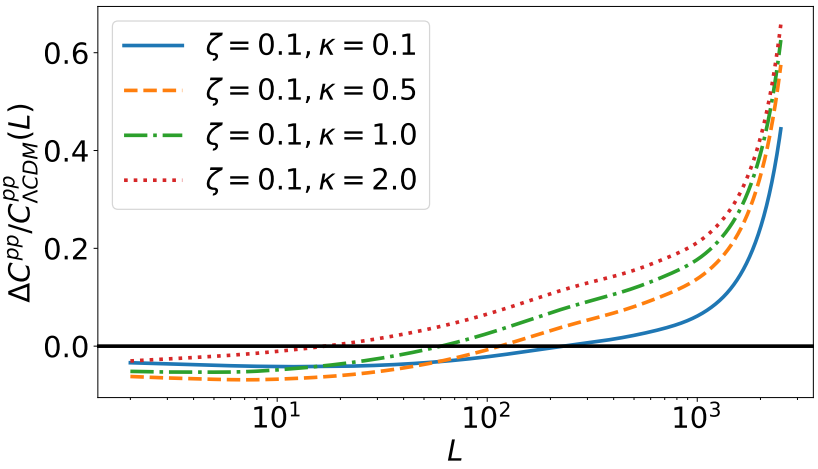

Figure 6.5: Relative difference in the CMB lensing potential spectrum between DMDR and ΛCDM, as a function of κ for $\zeta = 0.1$.

has been extensively studied with N-body simulations [77, 79, 177] and analytical fits or models [71, 178–180]. Limited previous studies of the small-scale structure formation in DMDR include simulations of a less general class of decaying dark matter models than the one we adopt here [134], and the demonstration that relativistic species have negligible contribution to the gravitational physics of the small-scale structure formation [181]. One potentially useful alternative to running simulations is recent work [182] which proposes to accurately model beyond-ΛCDM models by suitably rescaling the ΛCDM result in order to get one into the desired new model. These results are potentially useful and we may study and implement some of them in the future, but they are currently not validated to the level sufficient to enable us to model the nonlinear clustering in our DMDR cosmological model.

We therefore choose to limit our analysis to purely-linear scales, thus following the same strategy as in the DES-Y1 modified gravity analysis [85] (see also reference [183]). To summarize, we start with the difference between the nonlinear and linear-theory predictions of the observed data in the standard ΛCDM model at best-fit values of cosmological parameters, $\mathbf{d}_{\rm NL} - \mathbf{d}_{\rm lin}$. Using also the full error covariance of DES-Y1, $\mathbf{C}$, we calculate the quantity

$$\Delta\chi^2 \equiv (\mathbf{d}_{\rm NL} - \mathbf{d}_{\rm lin})^T \, \mathbf{C}^{-1} \, (\mathbf{d}_{\rm NL} - \mathbf{d}_{\rm lin}) \tag{6.15}$$

and identify the single data point that contributes most to this quantity. We remove that data point, and repeat the process masking out $\mathbf{d}_{\rm NL} < \mathbf{d}_{\rm lin}$ region until $\Delta\chi^2 < 1$. The resulting set of 334 (compared to the DES-Y1 3x2pt baseline 457) data points that remain constitutes our fiducial choice of linear-only scales.

6.2.5 Expectations and Forecasts

Before analyzing the data, we perform a forecast of the expected constraints. We do so in order to understand the parameter degeneracy structure, especially in regards to the new parameters ζ and κ. We would also like to understand what constraints are expected on these parameters. However, not all the likelihoods we plan to use in the real-data analysis have the corresponding mock likelihoods available. So for the forecast, we only use the DES-Y1 3x2pt and the Planck 2018 TT-TE-EE-lite data centered at the fiducial ΛCDM cosmology. The likelihood of simulated Planck data vector was calculated by implementing a wrapper of the work of reference [184] in `cosmosis`.

To obtain the forecasts on parameter constraints, we adopt the Fisher matrix methodology. The Fisher matrix is defined as

$$\mathcal{F}_{ij} = \sum_{mn} \frac{\partial v_m}{\partial p_i} [C^{-1}]_{mn} \frac{\partial v_n}{\partial p_j} + [\mathcal{I}^{-1}]_{ij} \tag{6.16}$$

evaluated at the fiducial cosmology, where v_m are the theoretically predicted data values, p_i are the cosmological and nuisance parameters, C_{ij} is the covariance matrix of the data, and $\mathcal{I}_{ij}$ is the covariance matrix of parameter priors. Fisher matrix calculations typically incorporate Gaussian priors on the parameters. Because we have flat priors on some of our parameters (see table 6.1), we adopt Gaussian priors of which the *variance* scales with the range (hence variance) of the flat priors that we have. Such Gaussian prior approximations are illustrated by black lines in figure 6.6. Thus we add $\mathcal{I}_{ij} = \delta_{ij}\mathrm{Var}[\mathcal{P}(p_i)]$, where δ_{ij} is the Kronecker Delta and $\mathcal{P}(p_i)$ any one of the Gaussian approximation of the flat priors from table 6.1. We center the cosmological parameters at the values listed in section 6.2.1. For the near-fiducial ΛCDM Fisher calculation, we adopt the DMDR parameter values of $\zeta = 10^{-4}$ and $\kappa = 1.0$, where all the cosmological observables have negligible difference from ΛCDM due to small ζ yet is sensitive enough to the two additional parameters. We use the `cosmosis`[4] [185] Fisher sampler to forecast the constraints on the DMDR parameters.

In the Fisher forecast results shown in figure 6.6, we observe that:

- The DMDR model breaks the tight correlation between Ω_m and h for *Planck*. In ΛCDM Ω_m and h are strongly anticorrelated because $\Omega_\mathrm{m}h^2$ is tightly constrained by the morphology of the acoustic peaks in the CMB spectrum. In DMDR, the background evolution has more freedom given by the variation of ζ and κ, thus weakening this degeneracy by adding more degrees of freedom in this 2D space.

- Furthermore, DES has a different degeneracy direction from Planck in the Ω_m–h plane,

[4] https://bitbucket.org/joezuntz/cosmosis/wiki/Home

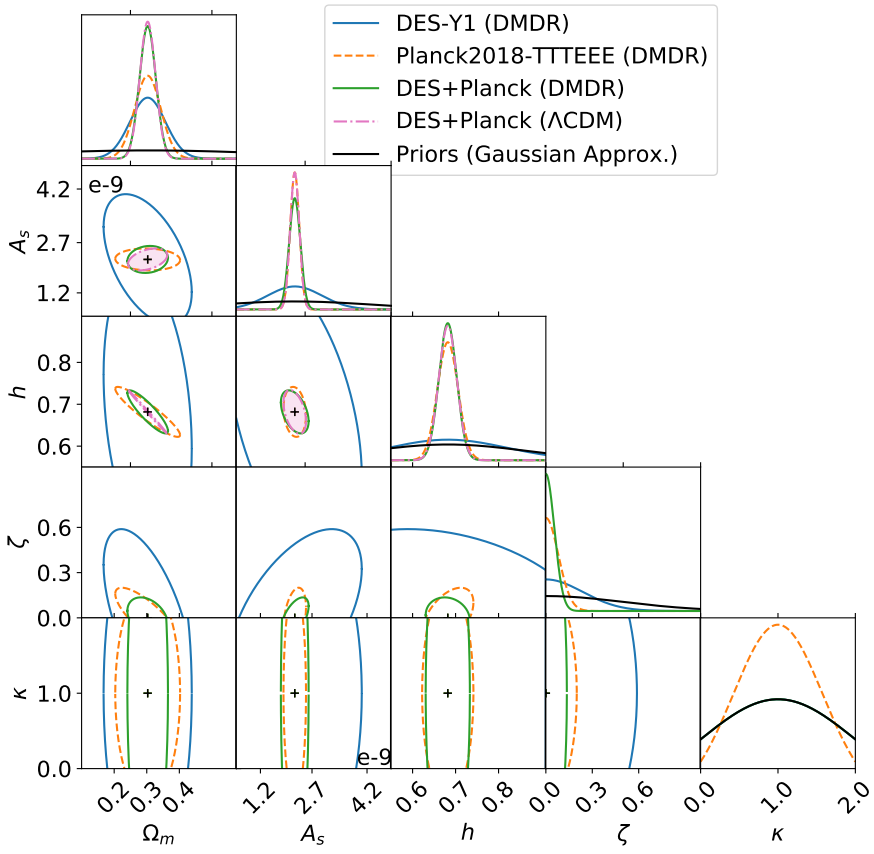

Figure 6.6: The DMDR Fisher forecasts showing 95% C.L. contours assuming simulated DES-Y1 3x2pt data, simulated Planck 2018 data, and the combination of both, all generated close to ΛCDM cosmology. The forecast is done assuming a Gaussian surface around the fiducial ΛCDM cosmology, specified by the same parameters in section 6.2.1. The combined datasets noticeably increased the constraint power, especially on the fraction of converted dark matter ζ. The ΛCDM model's degeneracy between h and Ω_m (note a very thin red contour in that plane) opened up in DMDR.

so that when the two probes are combined the degeneracy in this space is significantly reduced. Because ζ is significantly correlated with $\Omega_{\rm m}$, this degeneracy breaking greatly helps in constraining ζ.

- In figure 6.6 we assumed a DMDR cosmology very close to ΛCDM (with $\zeta = 10^{-4}$). In that case, there is effectively no constraint on the conversion rate κ, as expected.

Note again that the Fisher forecasts above are centered at $\zeta = 10^{-4}$, $\kappa = 1.0$ (near) ΛCDM. We have checked that, as the fiducial values of both ζ and κ increase away from their

ΛCDM values of zero, the forecasted constraints strengthen. Such behavior in Fisher matrix forecasts is not uncommon and occurs when the dependence of the measured quantities on the parameters of interest is nonlinear. Nevertheless, the constraints presented in figure 6.6 give us a rough idea of what to expect from the real data. We have also checked that increasing the fiducial converted fraction to $\zeta = 0.1$ only modestly strengthens constraints on κ.

We now proceed to describe our data and methodology.

6.3 Methodology

We follow the general scheme for the ΛCDM extension model analysis of the DES-Y1 3x2pt combined probes, which was described in detail in the DES-Y1 extensions paper [85]. In this section we will mainly focus on the methodology and systematics tests results specifically for the DMDR model, for full details, see references [85, 89].

6.3.1 Theory Prediction Pipeline

Our theory predictions for the DES 3x2pt data vector are derived from the 2D projection of the 3D matter and Weyl potential power spectra, incorporating complexities like nonlinear physics, galaxy bias, intrinsic alignments, photo-z bias, and shear calibration bias. The detailed derivation of 3x2pt theory prediction were described in Sec. IV.A of Ref. [89]. Here we only go through the procedures that are specifically modified for the DMDR model.

We first modify the Boltzmann code CAMB by implementing the equations described in section 6.2, and refer to this modified version as DMDR-CAMB. We also add a flag on σ_8 to ensure numerical stability in the nonlinear subroutine of DMDR-CAMB by attributing zero likelihood to models with $\sigma_8 > 1.4$ or $\sigma_8 < 0.4$. The resulting filter prior $\sigma_8 \in [0.4, 1.4]$, is about $\sim 10\sigma$ wide on each side of the fiducial value (relative to the DES-Y1 ΛCDM analysis [89], $\sigma_8 = 0.807^{+0.062}_{-0.041}$), and thus not expected to affect the overall constraints.

Next, the relation between the different cosmological quantities in the flat universe is enforced differently in DMDR comparing to ΛCDM because of a larger fraction of radiation density. The flat-universe relation is

$$\Omega_{\rm m} + \Omega_\Lambda + \Omega_{\rm dr} = 1. \tag{6.17}$$

Specifically, while in ΛCDM the flatness condition implies $\Omega_\Lambda = 1 - \Omega_{\rm m}$, in flat DMDR we enforce $\Omega_\Lambda = 1 - \Omega_{\rm m} - \Omega_{\rm dr}$ instead.

Finally we improve upon the usual assumption that the Weyl potential Φ is completely contributed by matter in the late universe, $\Phi = \frac{3}{2}\Omega_{\rm m}H_0^2\delta_{\rm m}/ac^2$. Recall the Weyl potential defined via the metric potentials ϕ and ψ in Newtonian gauge:

$$\begin{aligned} \Phi &= (\phi+\psi)/2 \\ ds^2 &= a^2(-(1+2\psi)dt^2 + (1-2\phi)dx^2). \end{aligned} \tag{6.18}$$

The assumption that the Φ power spectrum is proportional to the matter power spectrum is only reliable for negligible amounts of relativistic species in the late universe, which holds in ΛCDM but can break in DMDR models with large ζ. At super-horizon scales, Φ diverges from the local matter perturbation. Our strategy is to take the appropriate ratio between the linear Weyl potential power spectrum $P^{\rm lin}_{\Phi\Phi}$ and the linear matter power spectrum $P^{\rm lin}_{\delta\delta}$, and then modify the shear clustering, galaxy clustering, and galaxy–galaxy power spectra. The Weyl-corrected (WC) power spectra are:

$$P^{\rm WC}_{XX} = R_{\rm Weyl}\, P_{XX} \tag{6.19}$$

$$P^{\rm WC}_{gX} = R^{1/2}_{\rm Weyl} P_{gX}, \tag{6.20}$$

with the dimensionless Weyl-correction factor defined as

$$R_{\rm Weyl} \equiv \frac{P^{\rm lin}_{\Phi\Phi}}{\left[\frac{3}{2}\Omega_{\rm m}H_0^2(z+1)^2/c^2\right]^2}\frac{1}{P^{\rm lin}_{\delta\delta}} \tag{6.21}$$

where $X \in \{\gamma, {\rm IA}\}$ is a component of the correlation function that needs the Weyl correction (specifically, the shear and intrinsic alignments), and g stands for the galaxy position [5]. Hence $P^{\rm WC}_{XX}, P^{\rm WC}_{gX}$ are building blocks for the corresponding projected (two-dimensional) angular correlation functions; for example $P^{\rm WC}_{\delta\delta}$ is used for the calculation of 2D lensing shear power. The physical reason that the IA and shear components require the gravitational potential correction is that these processes are directly determined by the gravitational field; galaxy shear is formed by the bending of light in the gravitational field, and IA is induced by the tidal gravitational field generated by nearby mass.

The Weyl potential and Newtonian potential in principle differ because they depend on different gravitational fields. In practice, we find that their relative difference is $< 1\%$ throughout the expansion history in a not-strongly-anisotropic metric in both DMDR and ΛCDM. We are thus justified to calculate the correction ratio in equation (6.21) from the

[5] Here $P^{\rm lin}_{\Phi\Phi}$ has the same dimension as $P^{\rm lin}_{\delta\delta}$, for the output from CAMB multiplies the gravitational potential spectra by k^4.

Weyl-potential power spectrum. We further assume that Weyl potential correction is linear and commutes with intrinsic alignments and galaxy bias (this dramatically simplifies the implementation in the code). While this is not guaranteed to be true, given the current linear modeling of intrinsic alignments and galaxy bias any leading-order adjustment is likely absorbed by the nuisance parameters. Any scale-dependent caveats of this assumption should be further suppressed by the fact that we adopt conservative scale cuts to limit the impact of uncertainties in the modeling of nonlinearities,

Lastly, as discussed in section 6.2.4, we adopt Takahashi et al. halofit prescription [71] to produce the nonlinear matter power spectrum. Since it is designed by the halo model under the ΛCDM cosmology, we enforce the robustness of our analysis by cutting out the data points at nonlinear scales.

In Appendix B.1 we include a comparison between Y1 analysis pipeline and our DMDR pipeline when both are applied to the ΛCDM mock data vector. It illustrates that the pipeline modifications do not induce noticeable bias ($\lesssim 0.1\sigma$).

6.3.2 Parameters and Priors

The DES 3x2pt data analysis applied to the DMDR model includes a total of 28 parameters; they are listed in table 6.1. There are eight cosmological parameters and 20 nuisance parameters. DMDR introduces two additional cosmological parameters to the usual six $(\Omega_{\rm m}, h, \Omega_{\rm b}, n_{\rm s}, A_{\rm s}, \Omega_\nu h^2)$: the fraction of the converted dark matter ζ and the dark matter conversion rate κ. When combining DES 3x2pt data set with the external data sets, three more parameters, the reionization optical depth τ, supernova absolute magnitude M, and the Planck-lite likelihood nuisance parameter $a_{\rm Planck}$ are added into the variables. Their priors are presented in table 6.2.

The prior on ζ is flat in the range $\zeta \in [0.0, 1.0]$. This range is bounded by the limit when there is no dark matter conversion, and the limit when half of the dark matter has converted since the primordial time. The latter choice is based on the fact that the early-time Planck measurement of the matter density, $\Omega_{\rm m} = 0.3166 \pm 0.0084$ [99], is within 20% of the late-time DES measurement, $\Omega_{\rm m} = 0.264^{+0.032}_{-0.019}$. Hence, there is no indication that a large fraction of the dark matter has converted at $z \lesssim 1000$; this conclusion is also in line with previous work [134, 135, 140, 186].

The prior on the conversion rate κ is also flat, with the range $\kappa \in [10^{-7}, 2]$. We set the lower bound very slightly above zero in order to ensure numerical stability of the modified code, and checked that in this small-κ limit the observables agree with those of ΛCDM. The upper prior limit is determined by the fact that neither the matter power spectrum nor the

CMB angular power spectrum varies at a detectable level when $\kappa > 2$. This, in turn, can be understood from the evolution of the dark matter density illustrated in figure 6.1. When the conversion rate is as high as 2, new physics happened well after recombination and in the late stages of structure formation, allowing the DMDR model to mimic a ΛCDM universe with a higher density of dark matter. Thus models with $\kappa \gtrsim 2$ display a strong degeneracy between the new parameters (ζ, κ) and $\Omega_{\rm m}$, and are difficult to constrain tightly. It is important to keep this in mind when interpreting the κ posterior when it is pushed to the upper prior bound.

The cosmological parameters have flat priors that are nearly the same as in DES-Y1 (there are a few very minor differences between the two), and the nuisance parameters that model tomographic intrinsic alignments effect, photo-z uncertainty, shear calibration, and galaxy bias have the same Gaussian priors as in the DES-Y1 3x2 analysis [89]. We also impose a hard filter on the derived parameter σ_8 within $[0.4, 1.4]$ as described in section 6.3.1.

6.3.3 Datsets

Our cosmological parameters analysis will be performed on DES-Y1 3x2pt datasets, external datasets, and the combination of all datasets separately.

We first describe the DES-Y1 "3x2pt" measurements; here 3x2pt refers to three sets of two-point correlation functions as follows. Let i and j denote source-redshift bins (out of four total), and a and b denote the lens bins (out of five total). The correlation functions that form a set of observables that we call the "data vector" are:

- $\xi_{\pm}^{ij}(\theta)$, the correlation between galaxy shear measured in source bins i and j;
- $\gamma_t^{ib}(\theta)$, the cross correlation between the galaxy shear in source bin i and the galaxy positions in lens bin a;
- $w^{ab}(\theta)$ the correlation between galaxy positions in lens bins a and b.

The five redshift bins of the lens galaxy catalog are processed using redMaGiC [187]

$$z = [(0.15 \sim 0.3), (0.3 \sim 0.45), (0.45 \sim 0.6), \\ (0.6 \sim 0.75), (0.75 \sim 0.9)],$$

while the four redshift bins of the source galaxy catalog, obtained using the process called `METACALIBRATION` [188], are

$$z = [(0.2 \sim 0.43), (0.43 \sim 0.63), (0.63 \sim 0.9), (0.9 \sim 1.3)].$$

Table 6.1: Cosmological and nuisance parameters in DES-Y1 3x2pt analysis, and their priors.

Parameter	Prior
Cosmological	
$\Omega_{\rm m}$	flat (0.1, 0.9)
h	flat (0.55, 0.91)
$\Omega_{\rm b}$	flat (0.03,0.07)
$n_{\rm s}$	flat (0.87, 1.07)
$A_{\rm s}$	flat (5×10^{-10}, 5×10^{-9})
$\Omega_\nu h_0^2$	flat (0.0006, 0.01)
ζ	flat (0.0, 1.0)
κ	flat (1×10^{-7}, 2.0)
σ_8 (derived)	$\in$ (0.4, 1.4)
Lens Galaxy Bias	
$b_i, (i = 1, ...5)$	flat(0.8, 3.0)
Intrinsic Alignment	
$A_{IA}(z) = A_{IA}[(1+z)/1.62]\eta_{IA}$	
A_{IA}	flat (-5, 5)
η_{IA}	flat (-5, 5)
Lens photo-z shift (red sequence)	
Δz_l^1	Gauss (0.008, 0.007)
Δz_l^2	Gauss (-0.005, 0.007)
Δz_l^3	Gauss (0.006, 0.006)
Δz_l^4	Gauss (0.00, 0.01)
Δz_l^5	Gauss (0.00, 0.01)
Source photo-z shift	
Δz_s^1	Gauss (-0.001, 0.016)
Δz_s^2	Gauss (-0.019, 0.013)
Δz_s^3	Gauss (0.009, 0.011)
Δz_s^4	Gauss (-0.018, 0.022)
Shear calibration	
$m^i, (i = 1, ...4)$	Gauss (0.012, 0.023)

Table 6.2: Additional parameters used in the analysis with external datasets, along with their priors.

Parameter	Prior
Cosmological	
τ	flat (0.01, 0.2)
Supernovae Parameter	
M	flat (-20.0, -18.0)
Planck-lite Nuisance Parameter	
$a_{\rm Planck}$	Gauss (1.0, 0.0025)

Each tomographic two-point correlation function has 20 log-spaced angular bins in the range $2.5' < \theta < 250'$, and a total of 45 tomographic angular correlation functions in each theta-bin, for a total of $20 \times 45 = 900$ data points. Cutting out small angular scales to avoid uncertainties with modeling nonlinearities (see section 6.2.4) leaves 334 measurements. We refer the reader for other details, including those of theoretical modeling, to [89]. Treatment of some details specific for the DMDR is discussed in section 6.3.1.

Now we describe the external datasets that we adopt; they are:

- Cosmic microwave background (CMB): *Planck* 2018 high-ℓ TT, TE, EE, polarization modes temperature spectra with $\ell \geq 30$ from Plik-lite likelihood, and TT, EE of the low-ℓ, $\ell \leq 29$ from Commander and SimAll likelihood, plus lensing potential C_ℓs with multipoles $8 \leq L \leq 400$ from SMICA likelihood. [99, 189]

- Type Ia supernovae: we adopt the binned Pantheon SNe Ia dataset [93] covering the redshift range $0.01 < z < 2.3$.

- Baryon acoustic oscillation (BAO): we adopt the BOSS DR12 [90] measurements of $Hr_s/r_s^{\rm fid}, D_m r_s^{\rm fid}/r_s$ at redshifts [0.38, 0.51, 0.61], the SDSS-MGS [92] measurement of $\alpha = (D_V/D_V^{\rm fid})(r_s^{\rm fid}/r_s)$ at redshift 0.15, and the 6dFGS [91] measurement of r_s/D_V at redshift 0.106. The BOSS DR12 data come with a full covariance matrix, while all other data points only have diagonal uncertainties.

We do not include the redshift space distortion (RSD) measurements that we previously used in the DES+External data analysis [85]. We make this choice because DMDR allows for a scale-dependent growth of linear density perturbations, and the bias on $f\sigma_8$ measurements could be significant when the default ΛCDM templates are used in the compression of RSD information in the presence of a scale-dependent growth [190, 191].

6.3.4 Samplers

For our principal results — constraints in the multi-dimensional parameter space — we use `Polychord` [96]. `Polychord` is a nested sampler with outstanding performance on Bayesian evidence estimation, which is useful for tension and model comparison analysis. We set `Polychord` live_points = 250, num_repeats = 60, and tolerance = 0.1. This combination of settings was optimized to obtain precise and accurate results — especially in regards to the Bayesian-evidence computation — given our available CPU time.

We also need to run a number of chains for our systematic tests (shown further below in figure 6.7). High-quality nested-sampler runs are too time-consuming to be used for these runs. We thus make use of a couple of alternative numerical tools. First, we use

the `Multinest` [95] sampler, which is faster than `Polychord`. We use the `Multinest` sampler with settings live points = 250, efficiency = 0.3 and tolerance = 0.01. Second, we adopt our own importance sampler.

We use these two in conjunction as follows. We first run a baseline chain on uncontaminated theory predicted data vector, and save 334 3x2pt data points for each sample in the chain file. For the importance sampling, we re-weight the samples by a factor $w_{\rm new} = [\mathcal{L}_{\rm new}/\mathcal{L}_{\rm old}]w_{\rm old}$, where $\mathcal{L}_{\rm old}$ is the old likelihood from the MCMC chain, and $\mathcal{L}_{\rm new}$ is the new likelihood calculated using the systematics contaminated data vector and the theory 3x2pt saved for the MCMC samples. In this way, the importance sampler can produce a chain for certain systematic tests in minutes, as opposed to days which running the theoretical pipeline at each sample would take. This process is therefore very CPU-time-efficient, but is only valid in cases when importance sampling is representative on the baseline samples, and when the parameter space remains the same. Because sample systematics considered in our tests happen to lead to small deviations from the fiducial model — thanks to our adoption of linear-only scales and nuisance parameters to model general systematics — this assumption is justified. Quantitatively, the criterion for the effectiveness of the importance sampling is given by the effective sample size (ESS) given by ESS $= (\sum w)^2/\sum(w^2)$. We regard importance sampling as trustworthy if post-importance sampling ESS preserves $\gtrapprox 0.8$ of the baseline ESS, and this is satisfied for all of our systematic tests that use importance sampling.

In summary, for the real data chains we used `Polychord` as the sampler. The systematic tests using the importance sampler are the baryonic, non-Limber, magnification and RSD non-Limber effects. The IA systematics are modeled by nuisance parameters, so they cannot use importance sampling. We run `multinest` chain for the two IA systematics validation.

Now we proceed to the validation of pipeline robustness against systematics.

6.3.5 Systematics Tests

Systematic errors, both theoretical and observational, are always a worry for large-scale structure analyses. To address this, we adopt a two-pronged strategy. First, we restrict ourselves to linear scales only, as described in section 6.2.4. Second, we perform a battery of validation tests by adding various systematic effects to the data and monitoring how the results on the key cosmological parameters change. We now describe this latter strategy.

We start from a noiseless ΛCDM mock data vector for DES and Planck; that is, corresponding power spectra that contain no stochastic noise and are centered on the concordance theory model. The Planck mock likelihood is based on the compressed likelihood work [184],

centered at ΛCDM fiducial cosmology. The DES likelihood is identical to the one adopted in this analysis, using theory predicted mock data files. We calculate the cosmological constraints from this baseline case. We then add the systematic effects described in Sec. IV.A of DES-Y1 extended-models paper [85], corresponding to baryonic effects, Limber approximation, magnification bias, Limber approximation with redshift space distortion, two intrinsic alignment models and nonlinear galaxy bias, to generate systematics contaminated data vectors. In each of those cases, we redo the cosmological analysis and evaluate the errors on the key parameters.

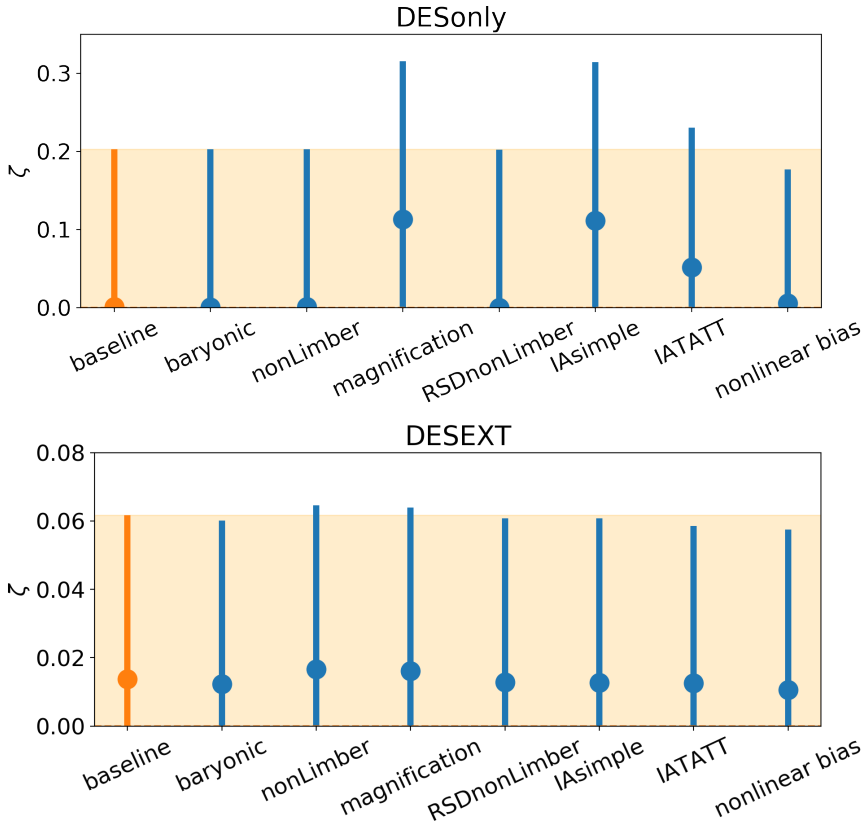

Figure 6.7: The effect of different systematics biases on ζ for DES-only (top) and DES+EXT (bottom) analysis. The only systematics that show a visible impact are the magnification and intrinsic alignments for the DES-only data, causing a $\approx 0.5\sigma$ bias on ζ. All other systematics studied here lead to negligible biases.

The results are shown in figure 6.7 for the DES-only case (upper panel) and DES+EXTERNAL dataset (lower panel). We see that the systematics are causing at most 0.5σ bias in dark matter converted fraction ζ in DES-only analysis, and no noticeable bias is observed when for the combination of DES and External dataset. The slight deviation ($\sim 0.2\sigma$) between the best-fit value of ζ and the assumed ΛCDM input $\zeta = 0.0$ is most likely due to the fact

that we ran this test with synthetic DES likelihood but real BAO and supernovae data, and the latter two are not enforced to recover the input-model parameter values.

Because the fiducial simulated data vector is at the ΛCDM cosmology, κ is not constrained and no interesting conclusion could be made on systematic bias. We therefore conclude that our results are robust to some of the key systematic errors, at least to the extent that our systematic models represent the real-world errors.

6.3.6 Blinding

We blinded our real data analysis in the following way. After obtaining the MCMC chain on the real data, before unblinding the cosmological results, we added a random number scaled by the variance of the parameter to the MCMC samples. During the blinded stage of the analysis, we carried out the postprocesses including 2-D contour plots and marginalized parameter constraints on these shifted samples. Our blinding preserves the shape of the contours with random shifting. Thus before proceeding to unblinding, we checked that the contour shapes are reasonable for the data constraining power, and the last few samples have the likelihoods at correct order of magnitude (they are usually not the MAP). In the end we unblinded the cosmological results by resuming the raw samples of the real data MCMC chain. No change to the pipeline was done after unblinding, for the results reported in the next section. The real data analysis pipeline is completely consistent with the systematics test in the above subsection.

6.4 Results

We now present our constraints on DMDR cosmology, followed by the tension and model-comparison results.

6.4.1 Constraints on DMDR model

The constraints on DMDR parameters ζ and κ are shown in figure 6.8, and their 1D marginalized statistics summarized in table 6.3. For the converted dark matter fraction ζ, we find:

$$\zeta < 0.32 \quad \text{DES-only, 65\% C.L.} \tag{6.22}$$

$$< 0.030 \quad \text{External-only, 65\% C.L.} \tag{6.23}$$

$$< 0.037 \quad \text{DES+External, 65\% C.L.} \tag{6.24}$$

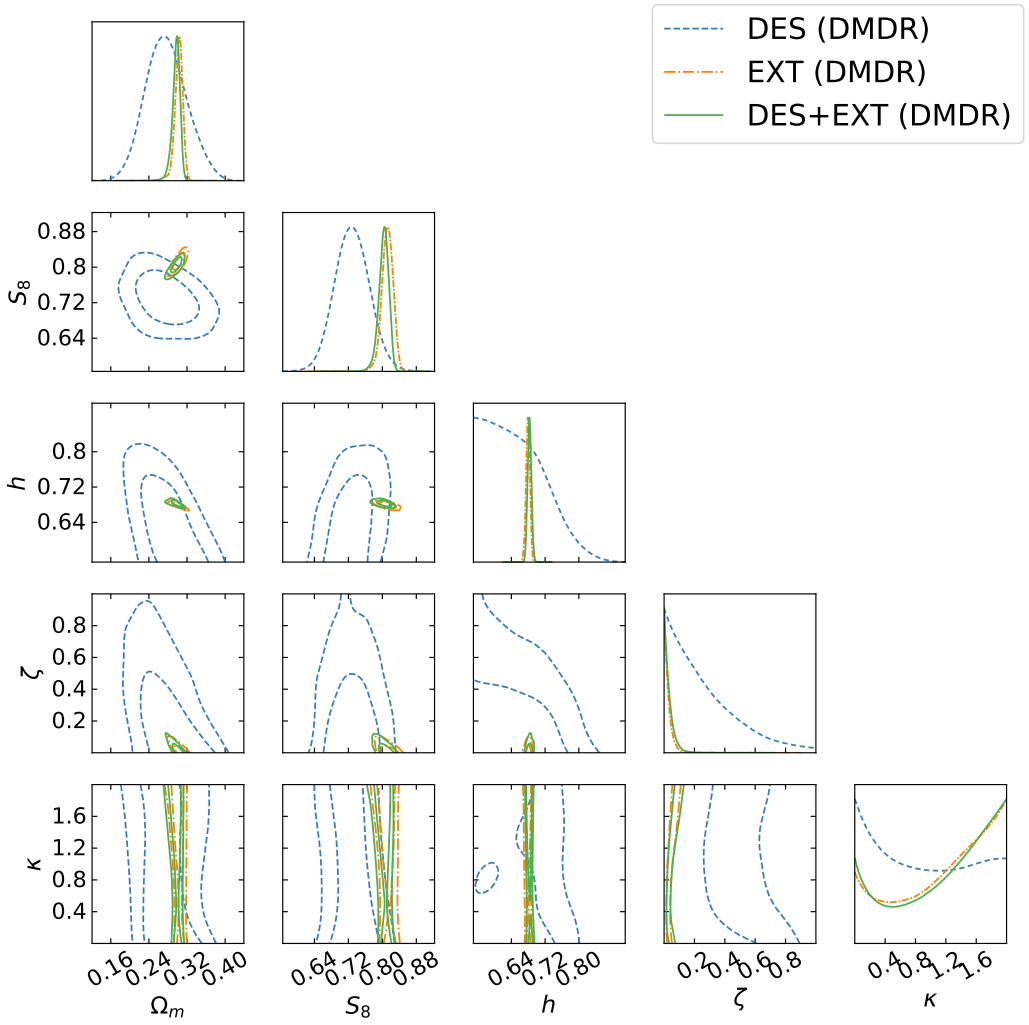

Figure 6.8: Constraints by DES-only, External-only, and DES+External data on the converted dark matter fraction ζ and rate κ, along with those on $\Omega_{\rm m}$, S_8, and h.

Note that we see a slightly looser constraint on ζ with DES+External dataset than External-only dataset. This is somewhat counter-intuitive, as our forecast predicted that weak lensing and galaxy clustering would tighten the constraint on ζ by anchoring the matter density at low redshift. However the Fisher forecast of course assumes Gaussian likelihood in all parameters. In the presence of non-Gaussianities, especially in a high-dimensional space, combined constraints are often (slightly) worse than those from individual probes.

No constraint on conversion rate κ is obtained; see the bottom right of figure 6.8. This agrees with the expectation that κ is unconstrained in the limit when the amount of converted dark matter, ζ, is very small.

We can see a raising posterior profile towards the upper bound of the κ prior. Although

not statistically meaningful, such posterior profile suggest that we possibly underestimated the prior upper bound. Other explanations include the IA systematics and high-dimensional parameter space geometry. In any case, higher κ, namely even faster conversion that happens at extremely low-z is still open for investigation. However exploration of this avenue requires a more specific analysis, similar to one in models with a late dark-energy transition [192] in order to take the distance-ladder calibration into consideration. Hence we leave this for future work.

Other cosmological parameters that are of interest because they are tightly constrained or exhibit tensions between surveys — h, $\Omega_{\rm m}$ and $S_8 = \sigma_8\sqrt{\Omega_{\rm m}/0.3}$ — are also illustrated in the triangle plot figure 6.8, and summarized in table 6.3.

6.4.2 Model Comparison and Tensions

As the tension between early and late universe surveys draws more and more attention in the cosmology community, there has been increasing number of works dedicated to quantify the concordance and discordance into statistical metrics [193–195]. In this work, we quote Bayesian evidence and maximum a posteriori (MAP) χ^2 difference as the model-comparison metrics, and use the "suspiciousness" metric defined in reference [194]. We also report the one-dimensional differences in units of error bars for the parameters suspected to be tension, i.e. $h, \Omega_{\rm m}$ and S_8. We stress that we avoid combining any datasets that are known to be in tension, such as *Planck* and distance ladder (for h) or *Planck* and DES (for S_8).

We now report the model-comparison results.

- χ^2 **at MAP Cosmology**. A very traditional criterion of the goodness of a model is the χ^2 evaluated at the maximum a posteriori parameter values $\chi^2_{\rm MAP} = (d-M)^{\rm T}C^{-1}(d-M)|_{\rm MAP}$, where d is the full dataset, M is the theory prediction evaluated at the maximum posterior sample, and C is the covariance matrix of the full dataset. A preferred model should have smaller MAP χ^2, and be punished by the number of extra parameters. Due to the non-gaussianity and the different normalization scheme of different survey likelihoods, we choose to report the effective χ^2 defined as:

$$\chi^2_{\rm MAP} = -2\log\mathcal{L}|_{\rm MAP}. \tag{6.25}$$

  We ran an optimizer three times, adopting the `scipy` optimizer with Nelder–Mead method to calculate the MAP from the `Polychord` chain samples; from these we report the best final MAP value. The χ^2 difference between the DMDR and ΛCDM

model is

$$\begin{aligned} \Delta\chi^2_{\rm MAP} &= -0.6 \qquad \text{DES-only} \\ &= +0.8 \qquad \text{External-only} \\ &= +0.1 \quad \text{DES+External.} \end{aligned} \tag{6.26}$$

as summarized in table 6.4. Therefore our DMDR model does not give a substantially better global fit to the data than ΛCDM.

- **Bayesian Evidence Ratio.** Bayesian evidence $\mathcal{Z}$ is defined as

$$\mathcal{Z} = \int \mathcal{L}(d|\theta)\Pi(\theta)d\theta \tag{6.27}$$

where $\mathcal{L}$ is the likelihood, d is the data vector, and θ are the model parameters. We report $\mathcal{Z}$ reported by the nested sampler `Polychord`, with statistics done by `Anesthetic` [196].[6] The evidence ratio could be interpreted as the probability of two models given data through [197]:

$$\frac{P(\text{DMDR}|d,I)}{P(\Lambda\text{CDM}|d,I)} = \frac{P(\text{DMDR}|I)}{P(\Lambda\text{CDM}|I)}\frac{\mathcal{Z}(\text{DMDR})}{\mathcal{Z}(\Lambda\text{CDM})} \tag{6.28}$$

where I is the prior that these two models are in the consideration. Assuming no prior preference for either DMDR or ΛCDM, namely $P(\text{DMDR}|I) = P(\Lambda\text{CDM}|I)$, the ratio of DMDR and ΛCDM probabilities is equal to the ratio of their respective evidences $\mathcal{Z}$. These, in turn, are reported by the `Polychord` sampler; their ratio is

$$\begin{aligned} K = \frac{\mathcal{Z}(\text{DMDR})}{\mathcal{Z}(\Lambda\text{CDM})} &= 0.31 \qquad \text{DES-only} \\ &= 0.03 \qquad \text{External-only} \\ &= 0.09 \quad \text{DES+External.} \end{aligned} \tag{6.29}$$

We interpret the Bayesian evidence ratio in terms of the Jeffreys' scale (making this also consistent with DES-Y1 paper [89]). Assuming an equal prior on ΛCDM and DMDR model, $0.31 < K < 1.0$ would indicate no conclusive preference for either model, $0.1 < K < 0.31$ would imply substantial evidence favouring ΛCDM, $0.031 < K < 0.1$ would imply strong evidence favouring ΛCDM, and $K < 0.031$ would imply very strong evidence favouring ΛCDM [198, 199].

[6] https://github.com/williamjameshandley/anesthetic

Under Jeffreys' scale, our results therefore indicate that the DES-Y1-only dataset does not prefer either DMDR or ΛCDM, while the External-only dataset very strongly disfavors the DMDR model. Finally the combination of all datasets strongly disfavors DMDR.

- **Suspiciousness.** This tension statistic [194] has the merit of being less affected by the choice of the priors than Bayesian evidence. Suspiciousness $\mathcal{S}$ is defined in terms of the Bayesian evidence ratio R and information ratio I:

$$\log \mathcal{S} = \log R - \log I, \tag{6.30}$$

where

$$R = \frac{\mathcal{Z}_{AB}}{\mathcal{Z}_A \mathcal{Z}_B} \tag{6.31}$$

$$\log I = \mathcal{D}_A + \mathcal{D}_B - \mathcal{D}_{AB} \tag{6.32}$$

$$\mathcal{D} = \int \mathcal{P}(\theta) \log \frac{\mathcal{P}(\theta)}{\Pi(\theta)} d\theta, \tag{6.33}$$

where $\mathcal{D}$ is the Kullback–Leibler divergence of the posterior against prior, quantifying the information gained by the data. The calculation of suspiciousness requires our knowledge of the posterior $\mathcal{P}$, prior Π, and evidence $\mathcal{Z}$ from MCMC chains. Here A and B stand for the DES-Y1 and External datasets that we are comparing, and AB for their combination. We report the $\log \mathcal{S}$ calculated by `Anesthetic` [196]:

$$\begin{aligned} \log \mathcal{S} &= -2.21, \quad p = 0.08 \qquad \text{DMDR} \\ \log \mathcal{S} &= -2.93, \quad p = 0.04 \qquad \Lambda\text{CDM} \end{aligned} \tag{6.34}$$

where each p-value is interpreted as the probability that datasets A and B can be both described by the parameters of the model. We therefore find that DMDR reduces the tension between DES and the external data, as indicated by a higher p-value, at the expense of two new parameters.

- **Hubble and S_8 tensions.** We now specifically investigate the impact of the new freedom in DMDR to two widely discussed tensions in ΛCDM: the 4-5σ tension in the (scaled) Hubble constant h between CMB and local measurements, and the 2-3σ tension in S_8 between CMB and weak lensing plus clustering. We take the probability distribution of the parameter difference $\Delta h = h_A - h_B$ or, alternatively, $\Delta S_8 = S_{8,A} - S_{8,B}$, from the 1D marginalized probability distribution obtained by different datasets.

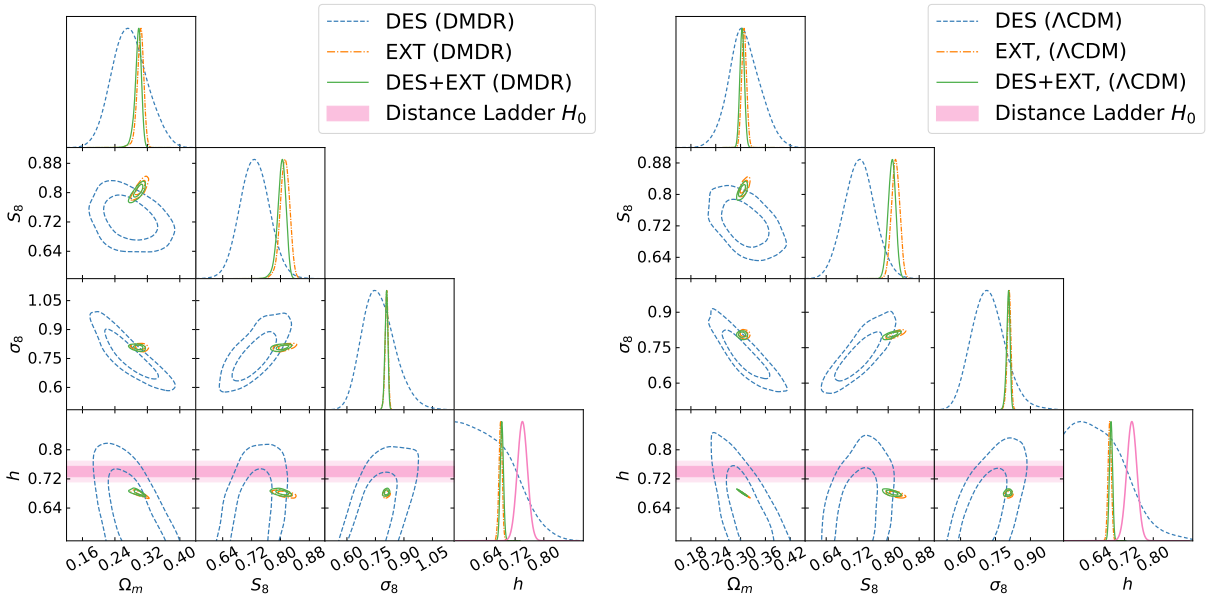

Figure 6.9: Upper panel: Cosmological parameters $\Omega_{\rm m}, S_8, \sigma_8, h$ constraints in DMDR model, reported for DES, External, and DES+External datasets, together with the local Hubble measurement [4] in pink. Lower panel: same plot in the ΛCDM cosmology. By comparing the panels involving σ_8, S_8 on both sides, we can see how DMDR reduced the tension in the matter density fields between DES and the CMB+Supernovae+BAOs.

Here A and B are the two datasets between which we want to estimate the tension (in either h or S_8). For a cosmological parameter of interest θ, we integrate over the interval bounded by the $\Delta\theta$ values that have the equal posterior, and one of the boundaries is $\Delta\theta = 0$. Thus we get the tension probability p:

$$p = \int_{\Delta\theta=0}^{\rm eq-post} P(\Delta\theta = \theta_A - \theta_B) d\Delta\theta. \tag{6.35}$$

We then interpret p into $z - \sigma$ tension using

$$p = \text{erf}\left(\frac{z}{\sqrt{2}}\right). \tag{6.36}$$

For the tension in the Hubble parameter, the dataset A is the full DES+CMB+Supernovae+BAO data, while dataset B is the Gaussian-distributed constraint on h from the distance-ladder measurement [4]. For the ΔS_8 tension, our A dataset is the DES-Y1 3x2pt only data, while B is the CMB+Supernovae+BAO External dataset. The zoomed-in constraints on Ω_m, S_8, σ_8 and h are illustrated in figure 6.9, over-plotted with the distance ladder measurement of H_0 from [4]. We find that:

– When comparing the DES+External datasets with local Hubble measurement in [4], $h = 0.7403 \pm 0.0142$, the tension in h assuming either DMDR or ΛCDM is 3.8σ.

– When comparing DES-Y1 dataset with External dataset, the tension in S_8 is 1.9σ for DMDR model, slightly reduced from 2.3σ for ΛCDM model.

Hence our DMDR model does not substantially alleviate the Hubble tension, but does help in reducing the S_8 tension.

6.5 Conclusions

In this work, we test a late-time dark matter to dark radiation conversion model, dubbed the DMDR model, against cosmological data. Our model is specified by two new parameters defined in equations (6.1) and (6.2): the fraction of dark matter that has converted ζ, and the rate of its conversion (to dark radiation) κ. We work out the perturbation equations in this model, and incorporate them in the Einstein–Boltzmann code CAMB [171]. Our analysis pipeline is modified for the DMDR model in the following respects. 1) we scale-dependently correct the shear and intrinsic alignment terms in the two-point correlation functions to account for the non-trivial relation between gravitational field and matter density perturbation field, and 2) we adopt conservative scale cuts to protect the analysis against systematic errors due to the modeling of clustering on nonlinear scales. In our analysis, we principally consider the DES-Y1 "3x2pt" (weak lensing and galaxy clustering) data. We also study the impact of adding external datasets: Planck-2018 CMB power spectra (TT, TE, EE, and lensing spectrum); Pantheon compilation of type Ia supernovae data; and compressed BAO measurements from BOSS-DR12, MGS and 6dFGS surveys.

The constraint on the fraction of the converted dark matter obtained from all data combined is $\zeta < 0.037$. We find no constraint on the conversion rate parameter κ as expected in the limit when $\zeta \to 0$. We further find that the evidence-ratio test applied with the full combined data does not favor the DMDR model compared to ΛCDM. DMDR does however reduce the suspiciousness tension metric between DES-Y1 and the combination of CMB, Supernovae and BAO data, raising the probability that DES and external data are concordant from 4% to 8%. Finally, DMDR does not help in alleviating the Hubble tension, but does reduce the tension in the DES and external-data measurements of $S_8 = \sigma_8\sqrt{\Omega_{\rm m}/0.3}$, making it go from 2.3σ (in ΛCDM) to 1.9σ (in DMDR).

We stress that the above conclusions are drawn for the late-universe dark matter-dark radiation conversion model introduced in section 6.2.1. Further generalizations of this cata-

logue [125, 126, 128–142], for example where dark matter is a composition of some fraction of interacting dark matter and cold dark matter, or where the transition time is short, or the transition occurs in the early universe, were not considered in this work. These variants could in principle better fit the background evolution of the universe than the model we studied, and are thus a promising target for further investigations.

There are several other directions in which our analysis could be extended. One possibility is to model the nonlinear matter power spectrum in real and redshift space in DMDR models [182, 200, 201]. This could be particularly helpful for DES Year-3 and Year-6 data which have more statistical power and where pushing to smaller, nonlinear scales could improve the constraints. Another future direction is to enable the use of the uncompressed BAO data (that is, the broadband galaxy and quasar power spectra). This would benefit not only the DMDR model but also other beyond-ΛCDM models, and could become an important analysis tool for future surveys such as those to be undertaken by DESI, the Rubin Observatory (LSST), Euclid, and the Roman Space Telescope.

Our investigation also has limitations on the observational probes that we used. As we are assembling this paper, several higher-precision new data release are already available from different surveys. Further more, the high-redshift observations, for example the Lyman-α BAO measurements from high-z quasars, and the 21-cm signal background plus spectrum, could be very helpful for constraining such beyond-ΛCDM models like DMDR. In this kind of models slow transitions are proposed to happen in the unknown era between the current time $z < 1$ and recombination.

In summary, many forthcoming investigations are waiting to be done on the theoretical, analytical, and the observational side for the beyond-ΛCDM cosmology.

Table 6.3: 1D marginalized statistics of cosmological parameters. The means of the marginalized 1D posteriors and 1σ confidence levels are reported, with global maximum posterior sample in the parenthesis. The dashed lines mean that there is no constraint on the parameter (but we report the global posterior maximum), while the N/A means that the parameter is not relevant to the model studied. For the DES-only DMDR constraint, the global best fit of $\Omega_{\rm m}$ is about 2σ away from the mean value, possibly due to the ζ–$\Omega_{\rm m}$ degeneracy. The degeneracy is broken for the External and DES+External datasets, when information from a wide redshift range is taken into consideration.

	h	$\Omega_{\rm m}$	S_8	ζ	κ
DES (DMDR)	< 0.68 (0.64)	$0.276^{+0.039}_{-0.046}$ (0.346)	0.729 ± 0.040 (0.700)	< 0.32 (0.01)	— (1.38)
DES (ΛCDM)	< 0.69 (0.72)	$0.310^{+0.035}_{-0.040}$ (0.306)	0.726 ± 0.039 (0.723)	N/A	N/A
EXT (DMDR)	0.6794 ± 0.0046 (0.6767)	$0.3025^{+0.0091}_{-0.0069}$ (0.3113)	0.812 ± 0.013 (0.829)	< 0.030 (0.028)	— (0.0033)
EXT (ΛCDM)	0.6786 ± 0.0046 (0.6783)	0.3085 ± 0.0059 (0.3093)	0.819 ± 0.011 (0.826)	N/A	N/A
DES+EXT (DMDR)	0.6830 ± 0.0045 (0.6822)	$0.2970^{+0.0091}_{-0.0062}$ (0.2994)	$0.803^{+0.013}_{-0.010}$ (0.808)	< 0.037 (0.020)	— (1.90)
DES+EXT (ΛCDM)	0.6822 ± 0.0043 (0.6825)	0.3038 ± 0.0054 (0.3036)	$0.809^{+0.010}_{-0.009}$ (0.808)	N/A	N/A
SH0ES	0.740 ± 0.014	N/A	N/A	N/A	N/A

Table 6.4: Difference in $\chi^2_{\rm MAP}$, evaluated at the maximum *a posteriori* point in parameter space, between DMDR and ΛCDM for different dataset combinations.

	DES-Y1 3x2pt	Planck2018-CMB	Planck2018-lensing	Pantheon	6dFGS	BOSS DR12	MGS	Total
DES $\Delta\chi^2_{\rm MAP}$	-0.6							-0.6
EXT $\Delta\chi^2_{\rm MAP}$		0.0	0.0	0.1	0.1	0.7	-0.1	0.8
DES+EXT $\Delta\chi^2_{\rm MAP}$	0.7	-0.4	-0.4	-0.0	0.0	0.3	-0.1	0.1

Chapter 7

Closing Remarks: Combined Probes Constraining Extended Cosmology in the Future

The major content of this chapter is dedicated to review the effect of ΛCDM assumptions in the cosmological survey when applied to extended models analysis. These are the evolving ingredients for a cosmological SNOWMASS-2021 review letter. This chapter ends with a summary of the thesis.

In response to the Hubble tension between late and early universe measurements, a growing number of extended cosmological models beyond ΛCDM model have been proposed and examined [106,109,134,202–204] . To obtain strong constraints on the model parameters and to explore their possible remedy of the tensions, many of these tests are done by combining published measurements from different surveys. However, the data analysis of current high-precision cosmological and astrophysical probes is complicated and uses many assumptions of ΛCDM in the analysis pipeline. Some of these assumptions are as obvious as the ΛCDM background geometry, while others are hidden in the details. The misuse of measured data based on ΛCDM assumptions on the beyond-ΛCDM models where these assumptions break down could result in misleading conclusions [122, 205]. To combat this, theorists should be cautious when analyzing their models, and observers should be clear about the specific assumptions in the published key paper results.

Strictly speaking, there is no clear-cut boundary between the statement of "doing your theoretical model predictions right" and the point of "alleviating the ΛCDM assumptions in the surveys". Here, the focus on the later aims to elucidate some profound technical details that might have been overlooked by the working groups using the **publicly published and deeply post-processed** cosmological/astrophysical survey results.

Baryonic acoustic oscillation (BAO) Recently the impact of fiducial cosmology assumptions on BAO measurements are discussed in several papers [206, 207]. A standard methodology for the recent BAO analysis is to reconstruct the galaxy power spectrum in a fiducial cosmology, then extract the sharpened BAO features from the reconstructed galaxy over-densities [208]. In this way, the BAO feature that has been smeared by the bulk flow of the astrophysical objects is recovered. The paper by P. Carter et al. [206] discussed the effect of fiducial cosmology assumption in the reconstruction process, and summarized three approximations that extended models should obey to avoid bias when using the fiducial BAO measurements. Among these approximations, the first thing that we should pay attention to is the re-scaling of the redshift-distance relationship, at least on the scales relevant to the BAO survey. If the redshift-distance relationship rescaling is more complicated than a linear factor multiplication in the redshift range of the galaxy samples, the configuration space distortion introduced by placing the galaxy at wrong distance is likely be unable to be captured by the Alcock–Paczynski (AP) parameters. The other approximations are mainly related to whether the power spectrum template used in the BAO information compression is inclusive enough to mitigate the cosmology dependence. These assumptions need further detailed analytic or simulation validation per model. The reassuring news is that in most of the cases studied so far, BAO measurement bias is below current precision for models. Both [206, 207] warned that this might be no longer true in higher precision next generation measurements due to fiducial cosmology assumption, even just in ΛCDM with varying cosmological parameters.

The inverse distance ladder approach of the BAO measurements is also worth mentioning. In this method, the sound horizon r_s is taken as a standard ruler thus the BAO measured angle corresponding to r_s at given redshift calibrates the distance to the observation. In this way we can get the constraint on H_0. Some literature cites this method as a "late universe" or "cosmology independent" measurement of H_0, which is not exactly true. There is no way to constrain H_0 without any early universe physics assumption on r_s, when the only information we know is $H_0 r_s$ (maybe plus $\Omega_b h^2$, which still does not specify the sound speed completely). This is an indicator that ΛCDM or fixed early universe is an essential presumption in inverse distance ladder H_0 constraints. Actually, in several strictly classical distance ladder BAO analyses [209, 210] without any cosmological assumptions (not inverse, anchored to the late universe supernovae or strong lensing), r_s is found to be systematically smaller than the Planck CMB result. Given these, it is not surprising that the inverse distance ladder BAO constraint on H_0 is on the early universe side of the current H_0 tension.

Redshift space distortion (RSD) It has been discussed extensively for some relatively more established beyond-ΛCDM model, like $f(R)$ modified gravity, that the compressed RSD survey results typically reported in the form of $f\sigma_8(z)$ values might be not applicable to extended model constraints [205, 211, 212]. By definition, the growth factor and the fluctuation of matter field are scale insensitive in standard ΛCDM [63].

$$f(z) \equiv \frac{d\ln D(z)}{d\ln a} \tag{7.1}$$

$$\sigma_8^2(z) \equiv \int_0^\infty \Delta^2(k,z)\left(\frac{3j_1(kR)}{kR}\right)^2 d\ln k, \text{ where } R = 8h^{-1}\text{Mpc} \tag{7.2}$$

where $j_1(kR)$ is the spherical Bessel function of the first kind. The definition of $D(z)$ and $\Delta^2(k)$ are introduced in chapter 2. The estimate of $f\sigma_8(z)$ is usually based on a fixed fiducial cosmology template of the redshift-space power spectrum [213, 214], because we expect this quantity to be only dependent on the amplitude of the measured RSD. When the fiducial template cannot mitigate the scale-dependent features in the clustering, $f\sigma_8$ measurement could be biased. The robustness of RSD estimate of $f\sigma_8$ against certain modified gravity simulations have been tested by [205, 211, 212]. Specifically, these studies found that the bias tends to be non-negligible for the models with scale dependent growth rates deviating from standard ΛCDM. This might be due to the fact that the multiplicative template parameters cannot absorb such scale dependent deviations from the fiducial cosmology. This finding is likely to appear in other beyond-ΛCDM models which introduce scale-dependent growth rate in the scale range sensible to the RSD measurements ($0.01h\text{Mpc}^{-1} \lesssim k \lesssim 0.2h\text{Mpc}^{-1}$), and the RSD compression into $f\sigma_8$ constraints should therefore be handled carefully.

Weak lensing In weak lensing, the main limitation of a fiducial cosmology assumption usually comes from the modeling of nonlinear matter power spectrum. Most halo model calculations used in fiducial pipelines for weak lensing analyses assume the same non-linear regime clustering physics as GR and ΛCDM. When testing a beyond-ΛCDM (and GR) model, the nonlinear regime should either be removed from the analysis or the nonlinear modeling should be validated – e.g. by using N-body simulations or perturbation theory calculations [215, 216].

Another place where beyond-ΛCDM modeling is needed is in the default analysis pipeline of the weak lensing surveys, for example the one used in DES [50], the lensing kernel takes the form:

$$q_\kappa(\chi) = \frac{3H_0^2\Omega_m}{2c^2}\frac{\chi}{a(\chi)}\int_\chi^{\chi_h} d\chi' \frac{n_\kappa(z(\chi')dz/d\chi'}{\bar{n}_\kappa}\frac{\chi'-\chi}{\chi'} \tag{7.3}$$

This is based on the late universe where: 1. the matter is the predominant contributor to

the gravitational potential, and 2. the gravity is ruled by the standard general relativity. The lensing kernel above thus relates the matter overdensity to the potential using the Poisson equation:

$$\Phi = \frac{4\pi G\rho_m a^2 \delta_m}{k^2} \tag{7.4}$$

However, when the two conditions above break down in extended cosmologies, for example in certain modified gravity theories, the correct thing to do is to use equation 3.30 to directly project the Weyl potential power spectrum to 2D harmonic space to obtain the shear spectrum. This way the Poisson equation is not presumed, thus the matter power spectrum and the Weyl potential power spectrum are not necessarily linearly related by the factor $\left(\frac{4\pi G\rho_m a^2}{k^2}\right)^2$. There are multiple ways to realize this adjustment to the analysis pipeline, the simplest being to correct the matter power spectrum used in ΛCDM pipeline by the ratio:

$$R_{\rm Weyl}(k,z) = \left(\frac{k^2(1+z)^2}{4\pi G\rho_m}\right)^2 \frac{P_{\rm Weyl}(k,z)}{P_m(k,z)} \tag{7.5}$$

Where $P_{\rm Weyl}(k,z)$ is the 3D k-space spectrum for Weyl potential perturbation as defined in chapter 3 for general gravitational potentials.

CMB The CMB theory prediction for the extended cosmological models should be straightforward if the Boltzmann codes are modified correctly for new Einstein and Boltzmann equations. When using a CMB lensing likelihood and/or high-ℓ lensed TT, EE, TE likelihoods, one should note that the nonlinear matter power spectrum is expected to be different from the ΛCDM modeling, thus its importance on the CMB observables. The nonlinear matter power spectrum or the Weyl potential power spectrum used for CMB lensing calculation should be treated as is described above in the "Weak lensing" paragraph. Alternatively, we limit our analysis to the linear scales, and here in CMB they mean not-too-high ℓs. Figure 7.1 illustrates the effect of nonlinear large scale structure on the lensed CMB temperature spectrum and the CMB lensing spectrum, where takahashi-halofit is used as the nonlinear model. The blue shade is the cosmic variance $\sigma = \sqrt{\frac{2}{(2\ell+1)}}C_\ell$. The difference between linearly and nonlinearly lensed TT spectrum exceeds the cosmic variance for $\ell \gtrsim 3000$. This difference shows up for $L \gtrsim 400$ in CMB lensing spectrum, roughly the complement of the conservative multipole range of the Planck 2018 CMB lensing likelihood [217].

Supernovae and distance ladder In many of the papers discussing the extended cosmology resolution to the Hubble tension, the distance ladder measurements of H_0 are incorporated into the analysis as a Gaussian likelihood. Recently several works [218, 219] have

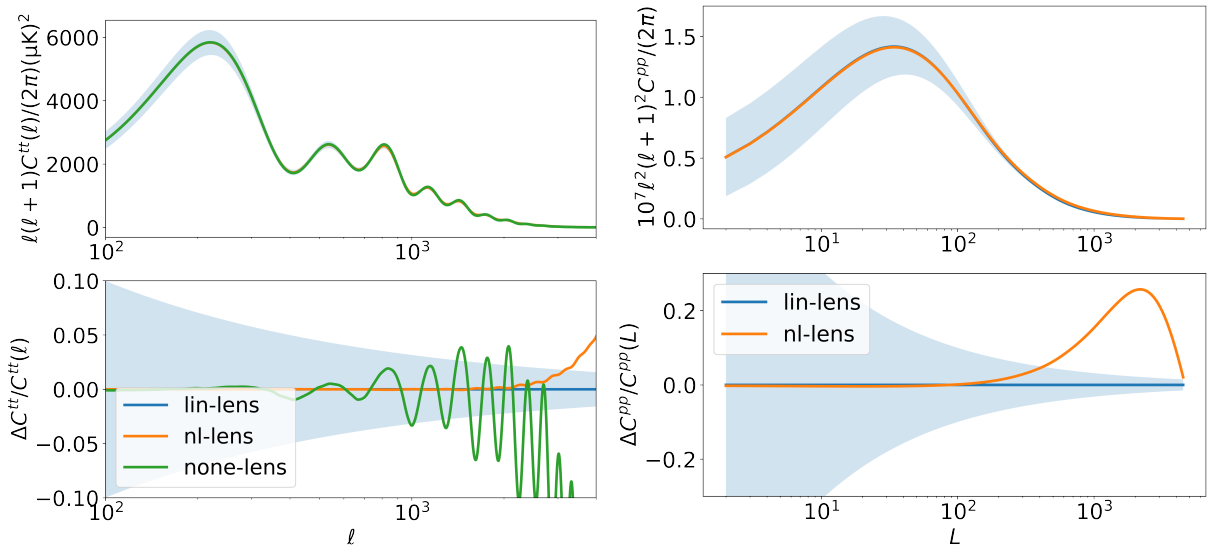

Figure 7.1: The lensing effect on CMB power spectra modeled by linear and nonlinear matter power spectra. Left panel: CMB TT spectrum and the relative differences. Right panel: CMB lensing potential spectrum and the relative differences. The legend "lin-lens" means that the CMB lensing potential spectrum is modeled by the linear matter power spectrum; "nl-lens" means that the CMB lensing potential spectrum is modeled by the nonlinear matter power spectrum; and "none-lens" means that the CMB TT spectrum is not lensed at all ($C^{pp}(L) = 0$). The blue shade depicts the cosmic variance range. There is no critical difference between ℓ and L notation of the moments and they are just kept the same as Planck 2018 papers conventions.

warned against this practice due to the caveat on extremely late universe transitional models. The reason for this is that local late universe measurements of H_0 depend on observations of astrophysical objects that extend into the Hubble flow. For example the SH0ES [220] results, that have been most frequently quoted, uses Pantheon supernovae sample in the redshift range $0.023 < z < 0.15$. Hence the distance ladder H_0 actually calibrates the absolute magnitude of the supernovae sample that includes higher redshifts objects. If a model predicts a higher Hubble constant can be achieved by extremely late transitional effect at $z < 0.02$, as with the example of red curve in figure 1 of [218], it is not actually resolving the Hubble tension. [221] gives the simplest method to correctly combine the distance ladder measurement of H_0:

$$\mathcal{L} = \mathcal{L}_{\rm SN} \times \mathcal{N}(M, \bar{M}(H_0), \sigma_M^2(\sigma_{H_0})) \tag{7.6}$$

i.e. to include the distance ladder H_0 measurement as the supernovae absolute magnitude prior.

This detail should be especially noted for extended cosmological models which deviate from ΛCDM phenomenology in late time (below several redshifts). However, note that

the consequence is not as severe as implied by [219] if the transition is not restrained to $z < 0.02$. The main point of the discussion above is that the H_0 measured at late time is not exactly the value at $z = 0$, and thus should be related to the supernovae absolute magnitude calibration at the same range of low redshifts. This means that the models which hide all the new physics at such low redshifts that are irrelevant to the $0.02 \lesssim z \lesssim 0.2$ Hubble flow measurements are naturally off the mark, as for example, the red curve in figure 1 of [192]. If a model has no drastic jump in the Hubble constant at $z < 0.02$, but a gradual change throughout several redshifts, the low redshift Hubble measurement $z \sim \mathcal{O}(0.1)$ could still be a reasonable anchor of current time H_0, and should be equivalent to equation 7.6. To keep things safer, Equation 7.6 is still recommended for any future analysis using distance ladder H_0 combined with supernovae sample.[1]

Summary and Conclusion

In this thesis, I have presented works on 1. the systematics in DES weak lensing cosmic shear measurements and 2. constraining ΛCDM and extended cosmological models using combined probes. Aiming at better fundamental physics parameter constraints, extensive studies have been carried out in service of precision analyses of cosmological surveys. In chapter 2, an overview of the stories in modern cosmology theory was presented, in the ΛCDM model background. In chapter 3, theory predictions of the galaxy clustering, weak lensing cosmic shear, and galaxy-galaxy lensing statistics were derived. Starting in chapter 4 the focus shifted to DES analysis, where the baryonic systematics in the cosmic shear analysis were investigated and the strategy for handling these systematics for DES Year-3 was determined. Chapter 5 focused on another aspect of the cosmological survey analysis, namely the statistical interpretations of the final results. This topic was investigated in the process of constraining the extended cosmologies using DES Year-1 combined with external data sets. Chapter 6 presented an analysis constraining a dark matter to dark radiation conversion model using DES and external data. Many details about the theory prediction and the full analysis pipeline on such extension models are discussed. Finally, in chapter 7, based on the experience of working on multiple probes constraining the DMDR model, I discussed the caveats of assuming ΛCDM in the cosmological surveys analysis pipelines.

We can see from the pretty facial materials in this chapter that analyzing the standard

[1] A rather irrelevant remark: in any case, I am personally objective to the idea of using the distance ladder Hubble measurement as Gaussian likelihood together with the early universe measurments like CMB or BAO inverse distance ladder, although most of the people are doing so. They are measurements that are currently in tension, hence should be confronted against each other but not combined, before we find a model or systematics that could accommodate both. The order should not be carried out inversely.

and extended cosmological models for combined probes in the current and next generation cosmological surveys is not merely a case of just introducing extra parameters into the calculation. I hope that this thesis has made points about how important some previously overlooked subtleties are for unveiling the true, exciting new physics. Theoretical models are fairly flexible modules in this kind of analyses, and we could look for the promising ones from the theorists' proposals. However, to concretely rule out or confirm a model we have to understand extremely well what we are doing with the real world observations, and to understand what the theoretical models imply phenomenologically. I am optimistic that such efforts would be very rewarding in the next generation precision cosmology, potentially providing much new information about our universe.

Appendix A

DES Analysis Pipeline

This appendix presents the DES Cosmosis analysis pipeline of the measured 3x2pt data vector. In order to obtain the constraint on the cosmological parameters, we need to sample through the parameter space based on the sampling strategy provided by a Monte Carlo sampler. At each sample point that specifies a sequence of the parameter values, we calculate the theory predicted data vector $\mathbf{M}(\mathbf{p})$ using the pipeline that will be described in section A.1 and obtain the posterior using equation 4.2. Section A.2 will introduce the sampler settings used in DES Year-1 analysis.

A.1 Cosmosis Pipeline Producing Single Likelihood

Here I list the Cosmosis DES Year-1 pipeline modules with their inputs and outputs.

1. consistency. **Input:** Cosmological parameters specifying a cosmology. **Output:** The rest of the cosmological parameters derived from the input in a consistent cosmology.

   This module ensures that the input cosmology parameters have no contradictions and computes the required derived parameters for the following modules. The most important physics consistency it checks is that $\sum_i \Omega_i = 1$.

2. camb. **Input:** cosmological parameters. **Output:** linear matter power, distances, σ_8, linear cold dark matter transfer function.

   camb is the code solving Boltzmann and Einstein equations, where the most physics happens. Linear matter power spectrum and CMB spectra are calculated by this module. DES Year-1 implemented Jan 2015 version of CAMB into Cosmosis.

3. halofit. **Input:** linear matter power. **Output:** nonlinear matter power.

Uses halo model to calculate nonlinear matter power spectrum from linear matter power spectrum.

4. growth. **Input:** $\Omega_m, \Omega_\Lambda, w$ and w_a **Output:** growth function $D(z)$ and $f(z)$, as defined in chapter 2 and 7.

   This module uses late time approximated perturbation equation to solve for the linear growth factor of matter over-density in a flat universe. The growth factor f is used in RSD likelihoods later.

5. extrapolate. **Input:** linear and nonlinear matter power. **Output:** extrapolated linear and nonlinear matter power.

6. fits_nz. **Input:** None. **Output:** source and lens galaxy $n(z)$

   Reads in the $n(z)$ measurements for source and lens galaxies.

7. lens_photoz_bias, source_photoz_bias. **Input:** source or lens $n(z)$, and photo-z errors for source or lens galaxies per bin. **Output:** shifted $n(z)$

   These modules read in the lens or source photo-z bias parameter Δz^i and shifts the number density $n^i(z) \to n^i(z - \Delta z^i)$.

8. unbiased_galaxies. **Input:** nonlinear matter power. **Output:** galaxy power.

   Copies matter power spectrum into galaxy power spectrum, assuming no galactic bias.

9. bias_neutrinos.**Input:** Cosmological parameters. **Output:** galactic bias.

   This module calculates the galactic bias $b_\nu(z, k)$ due to the neutrino free-streaming.

10. multiply_pk. **Input:** nonlinear matter power, $b_\nu(z, k)$. **Output:** galaxy power, matter-galaxy power.

    This module calculates galaxy power spectrum and matter-galaxy cross power spectrum by multiplying nonlinear matter power spectrum with $b_\nu^2(z, k)$ and $b_\nu(z, k)$. It overwrites the unbiased galaxy power saved in the upstream of pipeline.

11. IA. **Input:** Ω_m, intrinsic alignment amplitude A, nonlinear matter power, linear matter power, matter-galaxy power. **Output:** intrinsic alignment power, matter-IA power, galaxy-IA power.

    In DES Year-1 pipeline this module is configured to use the corrected Bridle & King method to calculate intrinsic alignment of the galaxies.

12. ia_z_field. **Input:** intrinsic alignment power law parameter α, intrinsic alignment power, matter-IA power, and galaxy-IA power. **Output:** z-dependent intrinsic alignment power, matter-IA power, and galaxy-IA power.

    This module decorates IA power with $(1+z)^{2\alpha}$ and matter-IA, galaxy-IA power with $(1+z)^{\alpha}$.

13. pk_to_cl. **Input:** matter-galaxy power, nonlinear matter power, galaxy power, intrinsic alignment power, matter-IA power, galaxy-IA power. **Output:** $C(\ell)$ spectrum for cosmic shear-galaxy position, shear-shear, position-position, IA-IA, shear-IA, position-IA correlations.

    This module carries out the Limber approximated integral for 3D power spectrum in $k-$space to obtain 2D $\ell-$space spectra.

14. bin_bias. **Input:** bin-wise galactic bias parameter, galaxy $C(\ell)$. **Output:** galaxy $C(\ell)$ multiplied by galactic bias.

    This module applies bin-wise linear galactic bias on galaxy $C(\ell)$s.

15. add_intrinsic **Input:** $C(\ell)$ spectrum for cosmic shear-galaxy position, shear-shear, IA-IA, shear-IA, position-IA correlations. **Output:** $C(\ell)$ spectrum for shear-shear and shear-position, with intrinsic alignment corrections.

    This module adds intrinsic alignment corrections into shear-shear and shear-position spectrum:

$$\text{shearshear} = \text{shearshear} + \text{IAIA} + 2\text{shearIA} \tag{A.1}$$

$$\text{shearposition} = \text{shearposition} + \text{positionIA} \tag{A.2}$$

    The order of the correlation pair is commutative.

16. shear_m_bias. **Input:** bin-wize shear calibration parameter m^i, shear-shear and shear-position $C(\ell)$. **Output:** shear calibration corrected shear-shear and shear-position $C(\ell)$.

    This module multiplies shear-shear $C^{ij}(\ell)$ by $(1+m^i)(1+m^j)$ and shear-position C^{ia} by $(1+m^i)$, where i, j are redshift bin numbers for source galaxy catalogs and a is one for a lens galaxy catalog.

17. 2pt_gal, 2pt_gal_shear, 2pt_shear. **Input:** $C(\ell)$s for galaxy position-position, shear-position and shear-shear correlations. **Output:** angular space 2pt-correlation functions for position-position, shear-position and shear-shear, i.e. the 3x2pt data vector including $w(\theta), \gamma_t(\theta)$ and $\xi_{\pm}(\theta)$.

These three modules integrate the product of $C(\ell)$ spectra with the corresponding Bessel functions to get 2pt-correlation functions in θ space, as described in equations 3.12, 3.35, 3.28 and 3.29.

18. 2pt_like. **Input:** The 3x2pt measurements and the covariance matrix. **Output:** 2pt Likelihood.

    This module calculates the 3x2pt likelihood as equation 4.3 using the measurement $\mathbf{D}$ and the covariance matrix C produced by DES survey Year-1 results.

A.2 Samplers

To infer the constraint on cosmological parameters, we sample through the parameter space, run the pipeline in the previous section A.1 at each sample point, and get an ensemble of the posteriors as expressed in equation 4.2. DES Year-1 key paper and extensions paper used two kind of samplers, Multinest and Emcee.

Multinest sampler [95] is a nested sampler. Such samplers are designed to find the collection of sample points in equal-likelihood prior volumes, so that the integral over equal-likelihood prior volumes could give us a reasonable estimation of the Bayesian evidence. The down side of nested samplers is that they typically converge much slower than the Monte-Carlo Markov Chain (MCMC) samplers with simpler algorithms, and save less samples in the chain. We used Multinest sampler with setting: number of live points = 500, efficiency = 0.3, and tolerance = 0.1. The typical number of the saved samples in a converged chain is $\sim 20,000$.

Emcee sampler [222] is a MCMC sampler. It modified the Metropolis-Hasting algorithm by using parallel multiple walkers, and by raising the proposals for these walkers in a correlated way so that the chain converges more efficiently. In DES Year-1, in the case that a model's parameter space is having difficulty to converge for a Multinest chain, we use Emcee sampler. We cannot calculate the Bayesian evidence from Emcee sampler outputs. We found that for DES Year-1 analysis, typically 300,000 samples burn-in is sufficient to get a stabilized Emcee chain [50], with number of walkers = 110. The typical number of samples in a burnt-in chain is $\sim 500,000$.

Appendix B

DMDR appendices

B.1 Pipeline Comparison on ΛCDM

We want to make sure that, any cosmological parameters constraints that are found different from the DES-Y1 3x2pt Key paper [89] ones are physical, namely caused by the DMDR model, but not due to the pipeline choices variance. Hence we run full `multinest` MCMC chains on the same ΛCDM simulated data vector, using DES-Y1 analysis pipeline and our DMDR analysis pipeline with $\zeta = 0.0$, $\kappa = 1.0$ fixed (ΛCDM subspace, so κ value is irrelevant). The results are shown in figures B.1 and B.2 for DES only and DES+External Data. In both cases, except for the parameters that are not effectively constrained like h, $\Omega_\nu h^2$ and n_s for DES only data, the posteriors from two pipelines agree with each other at $\lesssim 0.1\sigma$ level.

B.2 Dark Radiation Hierarchy equations

In B18, perturbation equations were derived from the perturbation expansion of the energy–momentum tensor for dark matter and dark radiation,

$$T^{\rm dm}_{\mu\nu} = \bar{\rho}_{\rm dm}(1+\delta_{\rm dm})u^{\rm dm}_\mu u^{\rm dm}_\nu \tag{B.1}$$

$$T^{\rm dr}_{\mu\nu} = \frac{4}{3}\bar{\rho}_{\rm dr}(1+\delta_{\rm dr})u^{\rm dr}_\mu u^{\rm dr}_\nu + \frac{\bar{\rho}_{\rm dr}(1+\delta_{\rm dr})}{3}g_{\mu\nu} + \Pi^{\rm dr}_{\mu\nu} \tag{B.2}$$

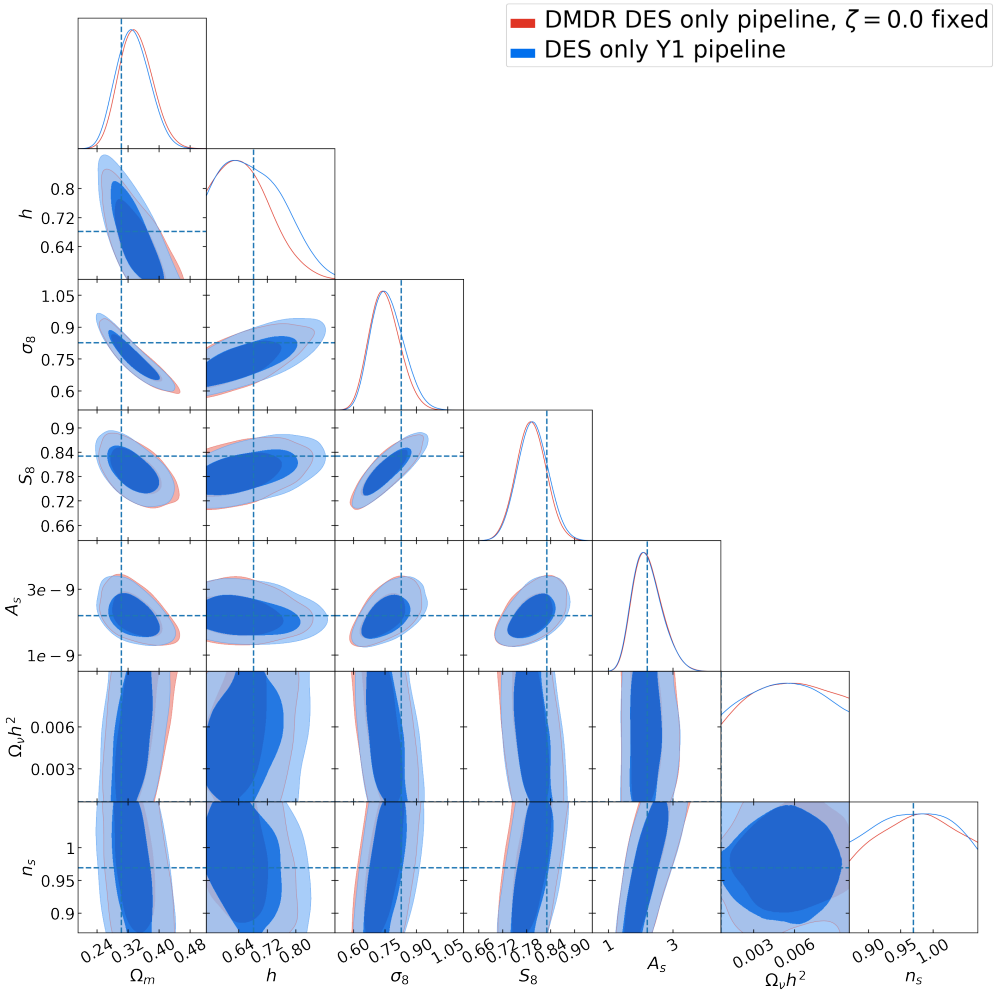

Figure B.1: Comparison of the constraints using DES-Y1 analysis pipeline (blue) and our DMDR analysis pipeline with new parameters fixed ($\zeta = 0.0$, $\kappa = 1.0$; red contours). We use a simulated ΛCDM data vector on which we apply the `multinest` MCMC chains for both runs.

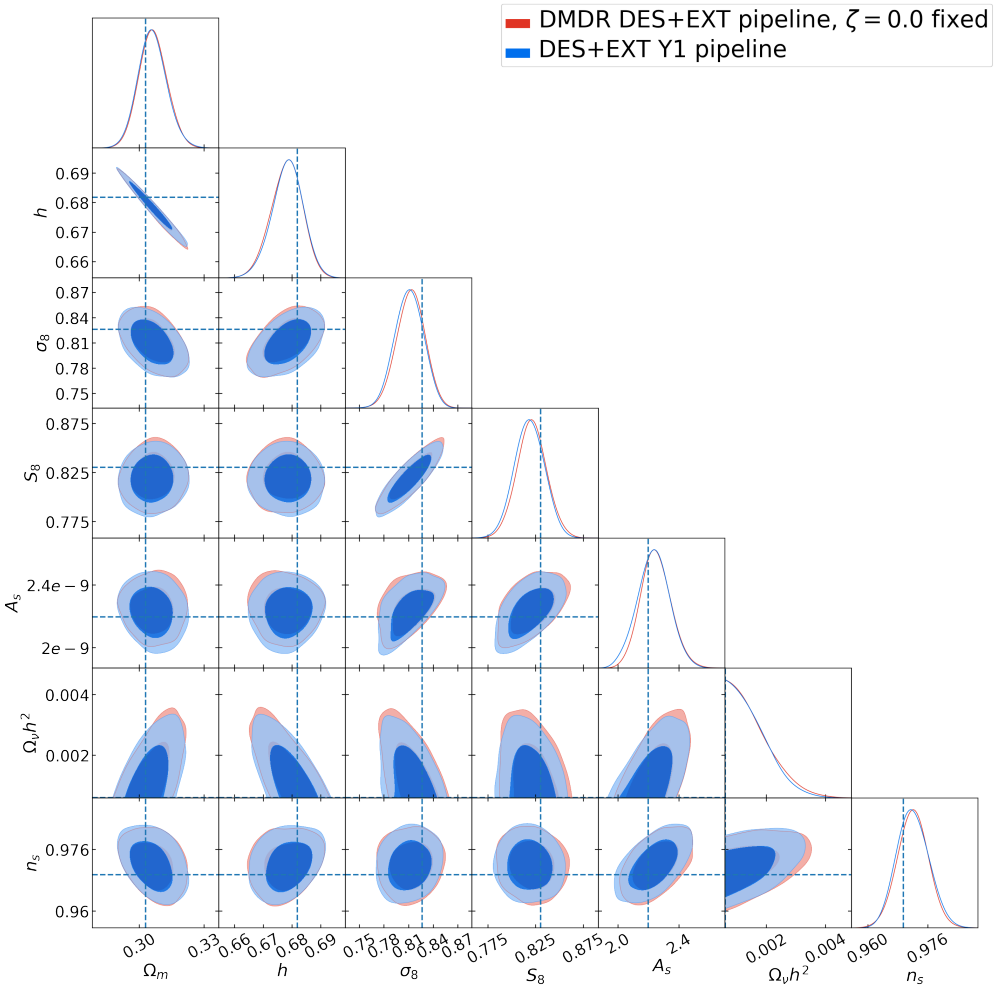

Figure B.2: Same as figure B.1, but for DES-Y1+External simulated data.

where in synchronous gauge $u_\mu^{\rm dm} = a(1,\vec{0})$, $u_\mu^{\rm dr} = a(1,\vec{v}^{\rm dr})$. For such dark matter and dark radiation, we can write the continuity equations and Einstein equations:

$$\nabla^\nu T_{\mu\nu}^{\rm dm} = -\nabla^\nu T_{\mu\nu}^{\rm dr} = -\mathcal{Q} u_\mu^{\rm dm} \tag{B.3}$$

$$R_{\mu\nu} - \frac{1}{2}R g_{\mu\nu} + \Lambda g_{\mu\nu} = \frac{8\pi G}{c^4} T_{\mu\nu} \tag{B.4}$$

where $u_\mu^{\rm dm}$ is the proper velocity of the dark matter. Note that the right-hand side of the continuity equation has a collision term instead of zero for CDM. In B18 the dark radiation is only expanded up to $\delta_{\rm dr}$, $\theta_{\rm dr} = \partial_i v_{\rm dr}^i$ and one anisotropy shear $\Pi_{ij}^{\rm dr} = (\partial_i\partial_j - \frac{1}{3}\delta_{ij}\nabla^2)\Pi^{\rm dr}$, which is sufficient when dark radiation self-interacts or continues to interact with dark matter after produced so the higher ℓ terms damp out.

In our work, we assume dark radiation to be a completely free-streaming relativistic species and write down the full phase space perturbation hierarchy equations for it, which differs from the massless neutrino ones by a collision term. The phase space dynamics of the dark radiation with collision terms are [172]:

$$\begin{aligned}\frac{\partial F_{\rm dr}(\vec{k},\hat{n},\tau)}{\partial\tau} + ik\mu F_{\rm dr}(\vec{k},\hat{n},\tau) = -\frac{2}{3}\dot{h}(\vec{k},\tau) - \frac{4}{3}(\dot{h}(\vec{k},\tau) \\ + 6\dot{\eta}(\vec{k},\tau))P_2(\hat{k}\cdot\hat{n}) + \left(\frac{\partial F_{\rm dr}(\vec{k},\hat{n},\tau)}{\partial\tau}\right)_C\end{aligned} \tag{B.5}$$

The phenomenology of the microphysics of the dark matter to dark radiation conversion process is mostly demonstrated in the collision term

$$\left(\frac{\partial F_{\rm dr}(\vec{k},\hat{n},\tau)}{\partial\tau}\right)_C = \frac{a}{\rho_{\rm dr}(a)}(-\mathcal{Q}(a)F_{\rm dr}(\vec{k},\hat{n},\tau) + \delta\mathcal{Q}), \tag{B.6}$$

especially its perturbation part $\delta\mathcal{Q}$ which depends on the details of the interacting physical quantities like particle momentum. However, from several case studies in B18 on Sommerfeld enhancement and single-body decay processes, it seems that the precision of the current generation of cosmological observations is not sufficient to discriminate between the specific forms of $\delta\mathcal{Q}$. Hence we assume the simplest form of the collision perturbation $\delta\mathcal{Q} = \mathcal{Q}\delta_{\rm dm}$, without dependence on polarization or momentum anisotropy:

$$\left(\frac{\partial F_{\rm dr}(\vec{k},\hat{n},\tau)}{\partial\tau}\right)_C = \frac{\mathcal{Q}(a)a}{\rho_{\rm dr}(a)}(-F_{\rm dr}(\vec{k},\hat{n},\tau) + \delta_{\rm dm}(\vec{k},\tau)) \tag{B.7}$$

Expanding $F_{\rm dr}$ in equation (B.7) into harmonics, we get

$$F_{\rm dr}(\vec{k},\hat{n},\tau)=\sum_{l=1}^{\infty}(-i)^l(2l+1)F_{\rm dr}l(\vec{k},\tau)P_l(\hat{k}\cdot\hat{n}). \tag{B.8}$$

Noticing that only $F_{\rm dr}(\vec{k},\hat{n},\tau)$ itself needs expansion while other terms in equation (B.7) are constant to the orientation variable $\hat{k}\cdot\hat{n}$, we get the hierarchy equation [172, 173, 175, 176]:

$$\begin{aligned}(J_l^{\rm dr})'=&\frac{k}{2l+1}[lJ_{l-1}^{\rm dr}-\beta_{l+1}(l+1)J_{l+1}^{\rm dr}]\\&+\frac{8}{15}k\sigma\delta_{l2}-\frac{4}{3}k\mathcal{Z}\delta_{l0}-\frac{aQ}{\bar{\rho}_{\rm dr}}J_l^{\rm dr}\end{aligned} \tag{B.9}$$

where $J_0^{\rm dr}\equiv\delta_{\rm dr}$, $J_1^{\rm dr}\equiv q_{\rm dr}=\frac{4}{3}\theta_{\rm dr}/k$, $J_2^{\rm dr}\equiv\pi_{\rm dr}=\Pi^{\rm dr}/\bar{\rho}_{\rm dr}$ in CAMB convention, δ_{l0},δ_{l2} are Dirac delta-functions. Equations $l=0, l=1$ agree with the Eqs. (14) and (15) in B18.

Bibliography

[1] S. Dodelson, *Modern Cosmology*. Academic Press, Amsterdam, 2003.

[2] **Supernova Cosmology Project** Collaboration, S. Perlmutter et al., *Measurements of Ω and Λ from 42 high redshift supernovae*, *Astrophys. J.* **517** (1999) 565–586, [astro-ph/9812133].

[3] M. J. Mortonson, D. Huterer, and W. Hu, *Figures of merit for present and future dark energy probes*, *Phys. Rev. D* **82** (2010) 063004, [arXiv:1004.0236].

[4] A. G. Riess, S. Casertano, W. Yuan, L. M. Macri, and D. Scolnic, *Large magellanic cloud cepheid standards provide a 1% foundation for the determination of the hubble constant and stronger evidence for physics beyond λcdm*, *The Astrophysical Journal* **876** (2019), no. 1 85.

[5] A. Einstein, *The Field Equations of Gravitation*, *Sitzungsber. Preuss. Akad. Wiss. Berlin (Math. Phys.)* **1915** (1915) 844–847.

[6] E. Hubble, *A relation between distance and radial velocity among extra-galactic nebulae*, *Proceedings of the national academy of sciences* **15** (1929), no. 3 168–173.

[7] H. Hildebrandt et al., *KiDS-450: Cosmological parameter constraints from tomographic weak gravitational lensing*, *Mon. Not. Roy. Astron. Soc.* **465** (2017) 1454, [arXiv:1606.05338].

[8] **BOSS** Collaboration, S. Alam et al., *The clustering of galaxies in the completed SDSS-III Baryon Oscillation Spectroscopic Survey: cosmological analysis of the DR12 galaxy sample*, *Mon. Not. Roy. Astron. Soc.* **470** (2017), no. 3 2617–2652, [arXiv:1607.03155].

[9] **DES** Collaboration, T. Abbott et al., *Dark Energy Survey year 1 results: Cosmological constraints from galaxy clustering and weak lensing*, *Phys. Rev. D* **98** (2018), no. 4 043526, [arXiv:1708.01530].

[10] **Planck** Collaboration, N. Aghanim et al., *Planck 2018 results. VI. Cosmological parameters*, *Astron. Astrophys.* **641** (2020) A6, [arXiv:1807.06209].

[11] D. Scolnic et al., *The Complete Light-curve Sample of Spectroscopically Confirmed SNe Ia from Pan-STARRS1 and Cosmological Constraints from the Combined Pantheon Sample*, *Astrophys. J.* **859** (2018), no. 2 101, [arXiv:1710.00845].

[12] **LIGO Scientific, Virgo** Collaboration, B. Abbott et al., *GW190425: Observation of a Compact Binary Coalescence with Total Mass* $\sim 3.4 M_{\odot}$, *Astrophys. J. Lett.* **892** (2020), no. 1 L3, [arXiv:2001.01761].

[13] **Event Horizon Telescope** Collaboration, K. Akiyama et al., *First M87 Event Horizon Telescope Results. I. The Shadow of the Supermassive Black Hole*, *Astrophys. J.* **875** (2019), no. 1 L1, [arXiv:1906.11238].

[14] J. D. Bowman, A. E. E. Rogers, R. A. Monsalve, T. J. Mozdzen, and N. Mahesh, *An absorption profile centred at 78 megahertz in the sky-averaged spectrum*, *Nature* **555** (2018), no. 7694 67–70, [arXiv:1810.05912].

[15] K. C. Wong et al., *H0LiCOW – XIII. A 2.4 per cent measurement of H0 from lensed quasars: 5.3σ tension between early- and late-Universe probes*, *Mon. Not. Roy. Astron. Soc.* **498** (2020), no. 1 1420–1439, [arXiv:1907.04869].

[16] N. Kaiser, *On the Spatial correlations of Abell clusters*, *Astrophys. J. Lett.* **284** (1984) L9–L12.

[17] A. H. Guth, *The Inflationary Universe: A Possible Solution to the Horizon and Flatness Problems*, *Adv. Ser. Astrophys. Cosmol.* **3** (1987) 139–148.

[18] J. C. Mather, E. Cheng, R. Eplee Jr, R. Isaacman, S. Meyer, R. Shafer, R. Weiss, E. Wright, C. Bennett, N. Boggess, et al., *A preliminary measurement of the cosmic microwave background spectrum by the cosmic background explorer (cobe) satellite*, *The Astrophysical Journal* **354** (1990) L37–L40.

[19] **WMAP** Collaboration, C. Bennett et al., *Nine-Year Wilkinson Microwave Anisotropy Probe (WMAP) Observations: Final Maps and Results*, *Astrophys. J. Suppl.* **208** (2013) 20, [arXiv:1212.5225].

[20] R. Keisler, C. Reichardt, K. Aird, B. Benson, L. Bleem, J. Carlstrom, C. Chang, H. Cho, T. Crawford, A. Crites, et al., *A measurement of the damping tail of the cosmic microwave background power spectrum with the south pole telescope*, *The Astrophysical Journal* **743** (2011), no. 1 28.

[21] **Atacama Cosmology Telescope** Collaboration, J. L. Sievers et al., *The Atacama Cosmology Telescope: Cosmological parameters from three seasons of data*, *JCAP* **10** (2013) 060, [arXiv:1301.0824].

[22] **COrE** Collaboration, F. R. Bouchet et al., *COrE (Cosmic Origins Explorer) A White Paper*, arXiv:1102.2181.

[23] **CMB-S4** Collaboration, K. N. Abazajian et al., *CMB-S4 Science Book, First Edition*, arXiv:1610.02743.

[24] L. Fu et al., *Very weak lensing in the CFHTLS Wide: Cosmology from cosmic shear in the linear regime*, *Astron. Astrophys.* **479** (2008) 9–25, [arXiv:0712.0884].

[25] R. Mandelbaum, A. Slosar, T. Baldauf, U. Seljak, C. M. Hirata, R. Nakajima, R. Reyes, and R. E. Smith, *Cosmological parameter constraints from galaxy-galaxy lensing and galaxy clustering with the SDSS DR7*, *Mon. Not. Roy. Astron. Soc.* **432** (2013) 1544, [arXiv:1207.1120].

[26] **Euclid** Collaboration, A. Blanchard et al., *Euclid preparation: VII. Forecast validation for Euclid cosmological probes*, *Astron. Astrophys.* **642** (2020) A191, [arXiv:1910.09273].

[27] S. A. Johnson, M. Penny, B. S. Gaudi, E. Kerins, N. J. Rattenbury, A. C. Robin, S. C. Novati, and C. B. Henderson, *Predictions of the nancy grace roman space telescope galactic exoplanet survey. ii. free-floating planet detection rates*, *The Astronomical Journal* **160** (2020), no. 3 123.

[28] **DESI** Collaboration, M. Levi et al., *The DESI Experiment, a whitepaper for Snowmass 2013*, arXiv:1308.0847.

[29] **LSST Science, LSST Project** Collaboration, P. A. Abell et al., *LSST Science Book, Version 2.0*, arXiv:0912.0201.

[30] D. Branch and G. Tammann, *Type ia supernovae as standard candles*, *Annual review of astronomy and astrophysics* **30** (1992) 359–389.

[31] W. J. Percival, *Large Scale Structure Observations*, in *186th Course of International School of Physics 'Enrico Fermi': New Horizons for Observational Cosmology*, vol. 186, pp. 101–135, 2014. arXiv:1312.5490.

[32] **LIGO Scientific, Virgo** Collaboration, B. P. Abbott et al., *A gravitational-wave measurement of the Hubble constant following the second observing run of Advanced LIGO and Virgo*, arXiv:1908.06060.

[33] **SKA** Collaboration, D. J. Bacon et al., *Cosmology with Phase 1 of the Square Kilometre Array: Red Book 2018: Technical specifications and performance forecasts*, *Publ. Astron. Soc. Austral.* **37** (2020) e007, [arXiv:1811.02743].

[34] A. Chen, D. Huterer, S. Lee, A. Ferté, N. Weaverdyck, O. A. Alves, C. D. Leonard, N. MacCrann, M. Raveri, A. Porredon, et al., *Constraints on decaying dark matter with des-y1 and external data*, *arXiv preprint arXiv:2011.04606* (2020).

[35] A. D. Linde, *A New Inflationary Universe Scenario: A Possible Solution of the Horizon, Flatness, Homogeneity, Isotropy and Primordial Monopole Problems*, *Phys. Lett. B* **108** (1982) 389–393.

[36] G. Steigman, *Primordial nucleosynthesis: successes and challenges*, *Int. J. Mod. Phys. E* **15** (2006) 1–36, [astro-ph/0511534].

[37] F. Zwicky, *Die Rotverschiebung von extragalaktischen Nebeln*, *Helv. Phys. Acta* **6** (1933) 110–127.

[38] V. C. Rubin and W. K. Ford, Jr., *Rotation of the Andromeda Nebula from a Spectroscopic Survey of Emission Regions*, *Astrophys. J.* **159** (1970) 379–403.

[39] A. G. Riess, A. V. Filippenko, P. Challis, A. Clocchiatti, A. Diercks, P. M. Garnavich, R. L. Gilliland, C. J. Hogan, S. Jha, R. P. Kirshner, et al., *Observational evidence from supernovae for an accelerating universe and a cosmological constant*, *The Astronomical Journal* **116** (1998), no. 3 1009.

[40] P. J. E. Peebles and B. Ratra, *The Cosmological Constant and Dark Energy*, *Rev. Mod. Phys.* **75** (2003) 559–606, [astro-ph/0207347].

[41] C.-P. Ma and E. Bertschinger, *Cosmological perturbation theory in the synchronous and conformal Newtonian gauges*, *Astrophys. J.* **455** (1995) 7–25, [astro-ph/9506072].

[42] A. Lewis and A. Challinor, *Camb: Code for anisotropies in the microwave background*, *Astrophysics source code library* (2011) ascl–1102.

[43] J. Lesgourgues, *The Cosmic Linear Anisotropy Solving System (CLASS) I: Overview*, arXiv:1104.2932.

[44] L. Verde, T. Treu, and A. G. Riess, *Tensions between the early and late universe*, *Nature Astronomy* **3** (2019) 891–895.

[45] A. G. Riess, *The expansion of the universe is faster than expected*, *Nature Reviews Physics* **2** (2020), no. 1 10–12.

[46] A. G. Riess et al., *New Parallaxes of Galactic Cepheids from Spatially Scanning the Hubble Space Telescope: Implications for the Hubble Constant*, *Astrophys. J.* **855** (2018), no. 2 136, [arXiv:1801.01120].

[47] J. D. Bowman, A. E. Rogers, R. A. Monsalve, T. J. Mozdzen, and N. Mahesh, *An absorption profile centred at 78 megahertz in the sky-averaged spectrum*, *Nature* **555** (2018), no. 7694 67.

[48] L. Perivolaropoulos and F. Skara, *Challenges for λcdm: An update*, *arXiv preprint arXiv:2105.05208* (2021).

[49] P. Lemos, A. Challinor, and G. Efstathiou, *The effect of Limber and flat-sky approximations on galaxy weak lensing*, *JCAP* **05** (2017) 014, [arXiv:1704.01054].

[50] **DES** Collaboration, E. Krause et al., *Dark Energy Survey Year 1 Results: Multi-Probe Methodology and Simulated Likelihood Analyses*, arXiv:1706.09359.

[51] **DES** Collaboration, J. Elvin-Poole et al., *Dark Energy Survey year 1 results: Galaxy clustering for combined probes*, *Phys. Rev. D* **98** (2018), no. 4 042006, [arXiv:1708.01536].

[52] **DES** Collaboration, M. A. Troxel et al., *Dark Energy Survey Year 1 results: Cosmological constraints from cosmic shear*, *Phys. Rev. D* **98** (2018), no. 4 043528, [arXiv:1708.01538].

[53] C. M. Hirata and U. Seljak, *Intrinsic alignment-lensing interference as a contaminant of cosmic shear*, *Phys. Rev. D* **70** (2004) 063526, [astro-ph/0406275]. [Erratum: Phys.Rev.D 82, 049901 (2010)].

[54] J. Blazek, N. MacCrann, M. A. Troxel, and X. Fang, *Beyond linear galaxy alignments*, *Phys. Rev. D* **100** (2019), no. 10 103506, [arXiv:1708.09247].

[55] H. Hildebrandt, M. Viola, C. Heymans, S. Joudaki, K. Kuijken, C. Blake, T. Erben, B. Joachimi, D. Klaes, L. t. Miller, et al., *Kids-450: Cosmological parameter constraints from tomographic weak gravitational lensing*, *Monthly Notices of the Royal Astronomical Society* **465** (2016), no. 2 1454–1498.

[56] H. Aihara et al., *The Hyper Suprime-Cam SSP Survey: Overview and Survey Design*, *Publ. Astron. Soc. Jap.* **70** (2018) S4, [arXiv:1704.05858].

[57] J. Prat, C. Sánchez, Y. Fang, D. Gruen, J. Elvin-Poole, N. Kokron, L. Secco, B. Jain, R. Miquel, N. MacCrann, et al., *Dark energy survey year 1 results: Galaxy-galaxy lensing*, *Physical Review D* **98** (2018), no. 4 042005.

[58] **DES** Collaboration, E. Rozo et al., *redMaGiC: Selecting Luminous Red Galaxies from the DES Science Verification Data*, *Mon. Not. Roy. Astron. Soc.* **461** (2016), no. 2 1431–1450, [arXiv:1507.05460].

[59] E. Huff and R. Mandelbaum, *Metacalibration: Direct self-calibration of biases in shear measurement*, *arXiv preprint arXiv:1702.02600* (2017).

[60] E. S. Sheldon and E. M. Huff, *Practical weak-lensing shear measurement with metacalibration*, *The Astrophysical Journal* **841** (2017), no. 1 24.

[61] J. Zuntz, T. Kacprzak, L. Voigt, M. Hirsch, B. Rowe, and S. Bridle, *Im3shape: a maximum likelihood galaxy shear measurement code for cosmic gravitational lensing*, *Monthly Notices of the Royal Astronomical Society* **434** (2013), no. 2 1604–1618.

[62] J. Zuntz, E. Sheldon, S. Samuroff, M. A. Troxel, M. Jarvis, N. MacCrann, D. Gruen, J. Prat, C. Sánchez, A. Choi, et al., *Dark energy survey year 1 results: weak lensing shape catalogues*, *Monthly Notices of the Royal Astronomical Society* **481** (2018), no. 1 1149–1182.

[63] D. Huterer, *Principles of Cosmology*. to be published, 2021.

[64] M. Jarvis, G. Bernstein, and B. Jain, *The skewness of the aperture mass statistic*, *Mon. Not. Roy. Astron. Soc.* **352** (2004) 338–352, [astro-ph/0307393].

[65] E. Krause and T. Eifler, *cosmolike – cosmological likelihood analyses for photometric galaxy surveys*, *Mon. Not. Roy. Astron. Soc.* **470** (2017), no. 2 2100–2112, [arXiv:1601.05779].

[66] M. Takada and W. Hu, *Power Spectrum Super-Sample Covariance*, *Phys. Rev. D* **87** (2013), no. 12 123504, [arXiv:1302.6994].

[67] I. Sevilla-Noarbe, K. Bechtol, M. C. Kind, A. C. Rosell, M. Becker, A. Drlica-Wagner, R. Gruendl, E. Rykoff, E. Sheldon, B. Yanny, et al., *Dark energy survey year 3 results: Photometric data set for cosmology*, *arXiv preprint arXiv:2011.03407* (2020).

[68] E. Lawrence, K. Heitmann, J. Kwan, A. Upadhye, D. Bingham, S. Habib, D. Higdon, A. Pope, H. Finkel, and N. Frontiere, *The Mira-Titan Universe II: Matter Power Spectrum Emulation*, *Astrophys. J.* **847** (2017), no. 1 50, [arXiv:1705.03388].

[69] **Euclid** Collaboration, M. Knabenhans et al., *Euclid preparation: II. The EuclidEmulator – A tool to compute the cosmology dependence of the nonlinear matter power spectrum*, *Mon. Not. Roy. Astron. Soc.* **484** (2019) 5509–5529, [arXiv:1809.04695].

[70] R. E. Smith, J. A. Peacock, A. Jenkins, S. White, C. Frenk, F. Pearce, P. A. Thomas, G. Efstathiou, and H. Couchman, *Stable clustering, the halo model and non-linear cosmological power spectra*, *Monthly Notices of the Royal Astronomical Society* **341** (2003), no. 4 1311–1332.

[71] R. Takahashi, M. Sato, T. Nishimichi, A. Taruya, and M. Oguri, *Revising the halofit model for the nonlinear matter power spectrum*, *The Astrophysical Journal* **761** (2012), no. 2 152.

[72] A. Schneider and R. Teyssier, *A new method to quantify the effects of baryons on the matter power spectrum*, *Journal of Cosmology and Astroparticle Physics* **2015** (2015), no. 12 049.

[73] M. P. van Daalen, J. Schaye, C. M. Booth, and C. D. Vecchia, *The effects of galaxy formation on the matter power spectrum: A challenge for precision cosmology*, *Mon. Not. Roy. Astron. Soc.* **415** (2011) 3649–3665, [arXiv:1104.1174].

[74] A. Mead, J. Peacock, C. Heymans, S. Joudaki, and A. Heavens, *An accurate halo model for fitting non-linear cosmological power spectra and baryonic feedback models*, *Mon. Not. Roy. Astron. Soc.* **454** (2015), no. 2 1958–1975, [arXiv:1505.07833].

[75] A. Mead, C. Heymans, L. Lombriser, J. Peacock, O. Steele, and H. Winther, *Accurate halo-model matter power spectra with dark energy, massive neutrinos and modified gravitational forces*, *Mon. Not. Roy. Astron. Soc.* **459** (2016), no. 2 1468–1488, [arXiv:1602.02154].

[76] K. Heitmann, M. White, C. Wagner, S. Habib, and D. Higdon, *The Coyote Universe I: Precision Determination of the Nonlinear Matter Power Spectrum*, *Astrophys. J.* **715** (2010) 104–121, [arXiv:0812.1052].

[77] J. Schaye, C. D. Vecchia, C. Booth, R. P. Wiersma, T. Theuns, M. R. Haas, S. Bertone, A. R. Duffy, I. McCarthy, and F. van de Voort, *The physics driving the*

cosmic star formation history, *Monthly Notices of the Royal Astronomical Society* **402** (2010), no. 3 1536–1560.

[78] **DES** Collaboration, H.-J. Huang et al., *Dark Energy Survey Year 1 Results: Constraining Baryonic Physics in the Universe*, arXiv:2007.15026.

[79] K. Heitmann, M. White, C. Wagner, S. Habib, and D. Higdon, *The coyote universe. i. precision determination of the nonlinear matter power spectrum*, *The Astrophysical Journal* **715** (2010), no. 1 104.

[80] K. Heitmann, E. Lawrence, J. Kwan, S. Habib, and D. Higdon, *The Coyote Universe Extended: Precision Emulation of the Matter Power Spectrum*, *Astrophys. J.* **780** (2014) 111, [arXiv:1304.7849].

[81] P. L. Taylor, F. Bernardeau, and E. Huff, *x-cut Cosmic Shear: Optimally Removing Sensitivity to Baryonic and Nonlinear Physics with an Application to the Dark Energy Survey Year 1 Shear Data*, *Phys. Rev. D* **103** (2021), no. 4 043531, [arXiv:2007.00675].

[82] J. F. Navarro, C. S. Frenk, and S. D. M. White, *A universal density profile from hierarchical clustering*, *The Astrophysical Journal* **490** (dec, 1997) 493–508.

[83] T. Hamana et al., *Cosmological constraints from cosmic shear two-point correlation functions with HSC survey first-year data*, *Publ. Astron. Soc. Jap.* **72** (2020), no. 1 Publications of the Astronomical Society of Japan, Volume 72, Issue 1, February 2020, 16, https://doi.org/10.1093/pasj/psz138, [arXiv:1906.06041].

[84] H.-J. Huang, T. Eifler, R. Mandelbaum, and S. Dodelson, *Modelling baryonic physics in future weak lensing surveys*, *Mon. Not. Roy. Astron. Soc.* **488** (2019), no. 2 1652–1678, [arXiv:1809.01146].

[85] T. Abbott, F. Abdalla, S. Avila, M. Banerji, E. Baxter, K. Bechtol, M. Becker, E. Bertin, J. Blazek, S. Bridle, et al., *Dark energy survey year 1 results: Constraints on extended cosmological models from galaxy clustering and weak lensing*, *Physical Review D* **99** (2019), no. 12 123505.

[86] P. Creminelli, G. D'Amico, J. Norena, and F. Vernizzi, *The Effective Theory of Quintessence: the w<-1 Side Unveiled*, *JCAP* **02** (2009) 018, [arXiv:0811.0827].

[87] T. Baker, P. G. Ferreira, C. Skordis, and J. Zuntz, *Towards a fully consistent parametrization of modified gravity*, *Physical Review D* **84** (2011), no. 12 124018.

[88] T. Baker, P. G. Ferreira, and C. Skordis, *The Parameterized Post-Friedmann framework for theories of modified gravity: concepts, formalism and examples*, *Phys. Rev. D* **87** (2013), no. 2 024015, [arXiv:1209.2117].

[89] T. Abbott, F. Abdalla, A. Alarcon, J. Aleksić, S. Allam, S. Allen, A. Amara, J. Annis, J. Asorey, S. Avila, et al., *Dark energy survey year 1 results: Cosmological constraints from galaxy clustering and weak lensing*, *Physical Review D* **98** (2018), no. 4 043526.

[90] S. Alam, M. Ata, S. Bailey, F. Beutler, D. Bizyaev, J. A. Blazek, A. S. Bolton, J. R. Brownstein, A. Burden, C.-H. Chuang, et al., *The clustering of galaxies in the completed sdss-iii baryon oscillation spectroscopic survey: cosmological analysis of the dr12 galaxy sample*, *Monthly Notices of the Royal Astronomical Society* **470** (2017), no. 3 2617–2652.

[91] F. Beutler, C. Blake, M. Colless, D. H. Jones, L. Staveley-Smith, G. B. Poole, L. Campbell, Q. Parker, W. Saunders, and F. Watson, *The 6df galaxy survey: $z = 0$ measurements of the growth rate and σ_8*, *Monthly Notices of the Royal Astronomical Society* **423** (2012), no. 4 3430–3444.

[92] A. J. Ross, L. Samushia, C. Howlett, W. J. Percival, A. Burden, and M. Manera, *The clustering of the sdss dr7 main galaxy sample–i. a 4 per cent distance measure at z= 0.15*, *Monthly Notices of the Royal Astronomical Society* **449** (2015), no. 1 835–847.

[93] D. Jones, D. Scolnic, A. Riess, A. Rest, R. Kirshner, E. Berger, R. Kessler, Y.-C. Pan, R. Foley, R. Chornock, et al., *Measuring dark energy properties with photometrically classified pan-starrs supernovae. ii. cosmological parameters*, *The Astrophysical Journal* **857** (2018), no. 1 51.

[94] J. Dunkley, M. Bucher, P. G. Ferreira, K. Moodley, and C. Skordis, *Fast and reliable markov chain monte carlo technique for cosmological parameter estimation*, *Monthly Notices of the Royal Astronomical Society* **356** (2005), no. 3 925–936.

[95] F. Feroz, M. P. Hobson, and M. Bridges, *MultiNest: an efficient and robust Bayesian inference tool for cosmology and particle physics*, *Monthly Notices of the Royal Astronomical Society* **398** (09, 2009) 1601–1614, [https://academic.oup.com/mnras/article-pdf/398/4/1601/3039078/mnras0398-1601.pdf].

[96] W. Handley, M. Hobson, and A. Lasenby, *Polychord: nested sampling for cosmology*, *Monthly Notices of the Royal Astronomical Society: Letters* **450** (2015), no. 1 L61–L65.

[97] A. Lewis, *Getdist: a python package for analysing monte carlo samples*, *arXiv preprint arXiv:1910.13970* (2019).

[98] M. C. Jones, *Simple boundary correction for kernel density estimation*, *Statistics and computing* **3** (1993), no. 3 135–146.

[99] N. Aghanim, Y. Akrami, M. Ashdown, J. Aumont, C. Baccigalupi, M. Ballardini, A. Banday, R. Barreiro, N. Bartolo, S. Basak, et al., *Planck 2018 results. vi. cosmological parameters*, *arXiv preprint arXiv:1807.06209* (2018).

[100] C. D. Huang, A. G. Riess, S. L. Hoffmann, C. Klein, J. Bloom, W. Yuan, L. M. Macri, D. O. Jones, P. A. Whitelock, S. Casertano, et al., *A near-infrared period–luminosity relation for miras in ngc 4258, an anchor for a new distance ladder*, *The Astrophysical Journal* **857** (2018), no. 1 67.

[101] A. G. Riess, S. Casertano, W. Yuan, L. M. Macri, and D. Scolnic, *Large magellanic cloud cepheid standards provide a 1% foundation for the determination of the hubble constant and stronger evidence for physics beyond λcdm*, *The Astrophysical Journal* **876** (2019), no. 1 85.

[102] W. L. Freedman, B. F. Madore, D. Hatt, T. J. Hoyt, I. S. Jang, R. L. Beaton, C. R. Burns, M. G. Lee, A. J. Monson, J. R. Neeley, et al., *The carnegie-chicago hubble program. viii. an independent determination of the hubble constant based on the tip of the red giant branch*, *The Astrophysical Journal* **882** (2019), no. 1 34.

[103] K. C. Wong, S. H. Suyu, G. C.-F. Chen, C. E. Rusu, M. Millon, D. Sluse, V. Bonvin, C. D. Fassnacht, S. Taubenberger, M. W. Auger, et al., *H0licow xiii. a 2.4% measurement of h_0 from lensed quasars: 5.3\σ tension between early and late-universe probes*, *arXiv preprint arXiv:1907.04869* (2019).

[104] E. Di Valentinoa, A. Melchiorrib, O. Menac, and S. Vagnozzid, *Interacting dark energy in the early 2020s: a promising solution to the h0 and cosmic shear tensions*, *arXiv preprint arXiv:1908.04281* (2019).

[105] V. Poulin, T. L. Smith, T. Karwal, and M. Kamionkowski, *Early dark energy can resolve the hubble tension*, *Physical review letters* **122** (2019), no. 22 221301.

[106] M.-X. Lin, G. Benevento, W. Hu, and M. Raveri, *Acoustic dark energy: Potential conversion of the hubble tension*, *Physical Review D* **100** (2019), no. 6 063542.

[107] N. Blinov, C. Keith, and D. Hooper, *Warm decaying dark matter and the hubble tension*, *Journal of Cosmology and Astroparticle Physics* **2020** (2020), no. 06 005.

[108] J. Sola, A. Gomez-Valent, J. d. C. Perez, and C. Moreno-Pulido, *Brans-dicke cosmology with a λ-term: a possible solution to λcdm tensions*, *arXiv preprint arXiv:2006.04273* (2020).

[109] K. Jedamzik and L. Pogosian, *Relieving the hubble tension with primordial magnetic fields*, *arXiv preprint arXiv:2004.09487* (2020).

[110] E. Elizalde, M. Khurshudyan, S. D. Odintsov, and R. Myrzakulov, *An analysis of the h_{0} tension problem in a universe with a viscous dark fluid*, *arXiv preprint arXiv:2006.01879* (2020).

[111] X. Li and A. Shafieloo, *Generalised emergent dark energy model: Confronting lambda and pede*, *arXiv preprint arXiv:2001.05103* (2020).

[112] W. Yang, E. Di Valentino, S. Pan, and O. Mena, *A complete model of Phenomenologically Emergent Dark Energy*, *arXiv preprint arXiv:2007.02927* (2020) [arXiv:2007.02927].

[113] L. Hart and J. Chluba, *Updated fundamental constant constraints from planck 2018 data and possible relations to the hubble tension*, *Monthly Notices of the Royal Astronomical Society* **493** (2020), no. 3 3255–3263.

[114] M. Ballardini, M. Braglia, F. Finelli, D. Paoletti, A. A. Starobinsky, and C. Umiltà, *Scalar-tensor theories of gravity, neutrino physics, and the h_0 tension*, *arXiv preprint arXiv:2004.14349* (2020).

[115] A. Leauthaud, S. Saito, S. Hilbert, A. Barreira, S. More, M. White, S. Alam, P. Behroozi, K. Bundy, J. Coupon, et al., *Lensing is low: cosmology, galaxy formation or new physics?*, *Monthly Notices of the Royal Astronomical Society* **467** (2017), no. 3 3024–3047.

[116] W. Lin and M. Ishak, *Cosmological discordances. ii. hubble constant, planck and large-scale-structure data sets*, *Physical Review D* **96** (2017), no. 8 083532.

[117] E. Di Valentino and S. Bridle, *Exploring the tension between current cosmic microwave background and cosmic shear data*, *Symmetry* **10** (2018), no. 11 585.

[118] M. Asgari, T. Tröster, C. Heymans, H. Hildebrandt, J. L. v. d. Busch, A. H. Wright, A. Choi, T. Erben, B. Joachimi, S. Joudaki, et al., *Kids+ viking-450 and des-y1 combined: Mitigating baryon feedback uncertainty with cosebis*, *arXiv preprint arXiv:1910.05336* (2019).

[119] M. A. Buen-Abad, G. Marques-Tavares, and M. Schmaltz, *Non-abelian dark matter and dark radiation*, *Physical Review D* **92** (2015), no. 2 023531.

[120] R. Murgia, S. Gariazzo, and N. Fornengo, *Constraints on the coupling between dark energy and dark matter from cmb data*, *Journal of Cosmology and Astroparticle Physics* **2016** (2016), no. 04 014.

[121] E. Di Valentino, C. Bœhm, E. Hivon, and F. R. Bouchet, *Reducing the h 0 and σ 8 tensions with dark matter-neutrino interactions*, *Physical Review D* **97** (2018), no. 4 043513.

[122] J. C. Hill, E. McDonough, M. W. Toomey, and S. Alexander, *Early dark energy does not restore cosmological concordance*, *arXiv preprint arXiv:2003.07355* (2020).

[123] M. M. Ivanov, E. McDonough, J. C. Hill, M. Simonović, M. W. Toomey, S. Alexander, and M. Zaldarriaga, *Constraining early dark energy with large-scale structure*, *arXiv preprint arXiv:2006.11235* (2020).

[124] A. Klypin, V. Poulin, F. Prada, J. Primack, M. Kamionkowski, V. Avila-Reese, A. Rodriguez-Puebla, P. Behroozi, D. Hellinger, and T. L. Smith, *Clustering and halo abundances in early dark energy cosmological models*, *arXiv preprint arXiv:2006.14910* (2020).

[125] A. Doroshkevich, A. Klypin, and M. Khlopov, *Large-scale structure of the universe in unstable dark matter models*, *Monthly Notices of the Royal Astronomical Society* **239** (1989), no. 3 923–938.

[126] M. Oguri, K. Takahashi, H. Ohno, and K. Kotake, *Decaying cold dark matter and the evolution of the cluster abundance*, *The Astrophysical Journal* **597** (2003), no. 2 645.

[127] M.-Y. Wang and A. R. Zentner, *Weak Gravitational Lensing as a Method to Constrain Unstable Dark Matter*, *Phys. Rev. D* **82** (2010) 123507, [arXiv:1011.2774].

[128] M. Cirelli, E. Moulin, P. Panci, P. D. Serpico, and A. Viana, *Gamma ray constraints on decaying dark matter*, *Physical Review D* **86** (2012), no. 8 083506.

[129] M.-Y. Wang and A. R. Zentner, *Effects of unstable dark matter on large-scale structure and constraints from future surveys*, *Physical Review D* **85** (2012), no. 4 043514.

[130] O. E. Bjaelde, S. Das, and A. Moss, *Origin of δneff as a result of an interaction between dark radiation and dark matter*, *Journal of Cosmology and Astroparticle Physics* **2012** (2012), no. 10 017.

[131] M.-Y. Wang, R. A. Croft, A. H. Peter, A. R. Zentner, and C. W. Purcell, *Lyman-α forest constraints on decaying dark matter*, *Physical Review D* **88** (2013), no. 12 123515.

[132] G. Blackadder and S. M. Koushiappas, *Dark matter with two-and many-body decays and supernovae type ia*, *Physical Review D* **90** (2014), no. 10 103527.

[133] S. Aoyama, T. Sekiguchi, K. Ichiki, and N. Sugiyama, *Evolution of perturbations and cosmological constraints in decaying dark matter models with arbitrary decay mass products*, *Journal of Cosmology and Astroparticle Physics* **2014** (2014), no. 07 021.

[134] K. Enqvist, S. Nadathur, T. Sekiguchi, and T. Takahashi, *Decaying dark matter and the tension in $\sigma 8$*, *Journal of Cosmology and Astroparticle Physics* **2015** (2015), no. 09 067.

[135] V. Poulin, S. Pasquale, D., and L. Julien, *A fresh look at linear cosmological constraints on a decaying dark matter component*, *Journal of Cosmology and Astroparticle Physics* **08** (2016) [arXiv:1606.02073].

[136] T. Bringmann, F. Kahlhoefer, K. Schmidt-Hoberg, and P. Walia, *Converting nonrelativistic dark matter to radiation*, *Physical Review D* **98** (2018), no. 2 023543.

[137] K. L. Pandey, T. Karwal, and S. Das, *Alleviating the h0 and s8 anomalies with a decaying dark matter model*, *Journal of Cosmology and Astroparticle Physics* (2019).

[138] K. Vattis, S. M. Koushiappas, and A. Loeb, *Late universe decaying dark matter can relieve the h_0 tension*, *arXiv preprint arXiv:1903.06220* (2019).

[139] M. Archidiacono, D. C. Hooper, R. Murgia, S. Bohr, J. Lesgourgues, and M. Viel, *Constraining dark matter-dark radiation interactions with cmb, bao, and lyman-α*, *Journal of Cosmology and Astroparticle Physics* **2019** (2019), no. 10 055.

[140] S. J. Clark, K. Vattis, and S. M. Koushiappas, *Cmb constraints on late-universe decaying dark matter as a solution to the h_0 tension*, *arXiv preprint arXiv:2006.03678* (2020).

[141] B. S. Haridasu and M. Viel, *Late-time decaying dark matter: constraints and implications for the h_0-tension*, *arXiv preprint arXiv:2004.07709* (2020).

[142] K. Enqvist, S. Nadathur, T. Sekiguchi, and T. Takahashi, *Constraints on decaying dark matter from weak lensing and cluster counts*, *Journal of Cosmology and Astroparticle Physics* **2020** (2020), no. 04 015.

[143] S. Tulin and H.-B. Yu, *Dark matter self-interactions and small scale structure*, *Physics Reports* **730** (2018) 1–57.

[144] M. Valli and H.-B. Yu, *Dark matter self-interactions from the internal dynamics of dwarf spheroidals*, *Nature Astronomy* **2** (2018), no. 11 907–912.

[145] J. S. Bullock and M. Boylan-Kolchin, *Small-scale challenges to the λcdm paradigm*, *Annual Review of Astronomy and Astrophysics* **55** (2017).

[146] S. Aiola, A. Kosowsky, and B. Wang, *Gaussian approximation of peak values in the integrated sachs-wolfe effect*, *Physical Review D* **91** (2015), no. 4 043510.

[147] A. Kovács, C. Sánchez, J. García-Bellido, J. Elvin-Poole, N. Hamaus, V. Miranda, S. Nadathur, T. Abbott, F. Abdalla, J. Annis, et al., *More out of less: an excess integrated sachs–wolfe signal from supervoids mapped out by the dark energy survey*, *Monthly Notices of the Royal Astronomical Society* **484** (2019), no. 4 5267–5277.

[148] M. Aguilar, L. A. Cavasonza, B. Alpat, G. Ambrosi, L. Arruda, N. Attig, P. Azzarello, A. Bachlechner, F. Barao, A. Barrau, et al., *Towards understanding the origin of cosmic-ray electrons*, *Physical review letters* **122** (2019), no. 10 101101.

[149] A. Boyarsky, O. Ruchayskiy, D. Iakubovskyi, and J. Franse, *Unidentified line in x-ray spectra of the andromeda galaxy and perseus galaxy cluster*, *Physical review letters* **113** (2014), no. 25 251301.

[150] M.-Y. Wang, A. H. Peter, L. E. Strigari, A. R. Zentner, B. Arant, S. Garrison-Kimmel, and M. Rocha, *Cosmological simulations of decaying dark matter: implications for small-scale structure of dark matter haloes*, *Monthly Notices of the Royal Astronomical Society* **445** (2014), no. 1 614–629.

[151] K. N. Abazajian, *Sterile neutrinos in cosmology*, *Physics Reports* **711** (2017) 1–28.

[152] Y. Farzan and M. Rajaee, *Dark matter decaying into millicharged particles as a solution to ams-02 positron excess*, *Journal of Cosmology and Astroparticle Physics* **2019** (2019), no. 04 040.

[153] A. Das, B. Dasgupta, and A. Ray, *Galactic positron excess from selectively enhanced dark matter annihilation*, *Physical Review D* **101** (2020), no. 6 063014.

[154] K. Ishiwata, O. Macias, S. Ando, and M. Arimoto, *Probing heavy dark matter decays with multi-messenger astrophysical data*, *Journal of Cosmology and Astroparticle Physics* **2020** (2020), no. 01 003.

[155] C. Dessert, N. L. Rodd, and B. R. Safdi, *The dark matter interpretation of the 3.5-kev line is inconsistent with blank-sky observations*, *Science* **367** (2020), no. 6485 1465–1467.

[156] S. Bhargava, P. Giles, A. Romer, T. Jeltema, J. Mayers, A. Bermeo, M. Hilton, R. Wilkinson, C. Vergara, C. Collins, et al., *The xmm cluster survey: new evidence for the 3.5 kev feature in clusters is inconsistent with a dark matter origin*, *Monthly Notices of the Royal Astronomical Society* (2020).

[157] M.-Y. Wang, L. E. Strigari, M. R. Lovell, C. S. Frenk, and A. R. Zentner, *Mass assembly history and infall time of the Fornax dwarf spheroidal galaxy*, *Mon. Not. Roy. Astron. Soc.* **457** (2016), no. 4 4248–4261, [arXiv:1509.04308].

[158] M. Pospelov and M. Trott, *R-parity preserving super-wimp decays*, *Journal of High Energy Physics* **2009** (2009), no. 04 044.

[159] R. Allahverdi, B. Dutta, F. S. Queiroz, L. E. Strigari, and M.-Y. Wang, *Dark matter from late invisible decays to and of gravitinos*, *Physical Review D* **91** (2015), no. 5 055033.

[160] U. Ellwanger, H. Cyril, and T. Ana, M., *The next-to-minimal supersymmetric standard model.*, *Physics Reports* **496** (2010), no. 1 [arXiv:0910.1785v].

[161] T. Higaki and F. Takahashi, *Dark radiation and dark matter in large volume compactifications*, *Journal of High Energy Physics* **2012** (2012), no. 11 125.

[162] K. Bondarenko, J. Pradler, and A. Sokolenko, *Constraining dark photons and their connection to 21 cm cosmology with cmb data*, *arXiv preprint arXiv:2002.08942* (2020).

[163] C. Bernard, K. Florian, and S. Marit, *Primordial black holes as dark matter.*, *PHYSICAL REVIEW D* **94** (2016), no. 8 [arXiv:1607.06077].

[164] M. Raidal, V. Vaskonen, and H. Veermäe, *Gravitational waves from primordial black hole mergers*, *Journal of Cosmology and Astroparticle Physics* **2017** (2017), no. 09 037.

[165] I. Masina, *Dark matter and dark radiation from evaporating primordial black holes*, *arXiv preprint arXiv:2004.04740* (2020).

[166] R. Laha, *Primordial black holes as a dark matter candidate are severely constrained by the galactic center 511 kev γ-ray line*, *Physical Review Letters* **123** (2019), no. 25 251101.

[167] S. Clesse and J. García-Bellido, *Seven hints for primordial black hole dark matter*, *Physics of the Dark Universe* **22** (2018) 137–146.

[168] P. Montero-Camacho, X. Fang, G. Vasquez, M. Silva, and C. M. Hirata, *Revisiting constraints on asteroid-mass primordial black holes as dark matter candidates*, *Journal of Cosmology and Astroparticle Physics* **2019** (2019), no. 08 031.

[169] N. Smyth, S. Profumo, S. English, T. Jeltema, K. McKinnon, and P. Guhathakurta, *Updated constraints on asteroid-mass primordial black holes as dark matter*, *Physical Review D* **101** (2020), no. 6 063005.

[170] J. Jin and Z. S. Jjie, *Computation of special functions*. Wiley, 1996.

[171] C. Howlett, A. Lewis, A. Hall, and A. Challinor, *Cmb power spectrum parameter degeneracies in the era of precision cosmology*, *Journal of Cosmology and Astroparticle Physics* **2012** (2012), no. 04 027.

[172] C.-P. Ma and E. Bertschinger, *Cosmological perturbation theory in the synchronous and conformal newtonian gauges*, *arXiv preprint astro-ph/9506072* (1995).

[173] A. Lewis, *Camb notes*, 2011.

[174] K. Ichiki, M. Oguri, and K. Takahashi, *Constraints from the wilkinson microwave anisotropy probe on decayingcold dark matter*, *Physical Review Letters* **93** (Aug, 2004).

[175] D. Blas, J. Lesgourgues, and T. Tram, *The cosmic linear anisotropy solving system (class). part ii: approximation schemes*, *Journal of Cosmology and Astroparticle Physics* **2011** (2011), no. 07 034.

[176] B. Audren, J. Lesgourgues, G. Mangano, P. D. Serpico, and T. Tram, *Strongest model-independent bound on the lifetime of dark matter*, *Journal of Cosmology and Astroparticle Physics* **2014** (2014), no. 12 028.

[177] S. McAlpine, J. C. Helly, M. Schaller, J. W. Trayford, Y. Qu, M. Furlong, R. G. Bower, R. A. Crain, J. Schaye, T. Theuns, et al., *The eagle simulations of galaxy formation: Public release of halo and galaxy catalogues*, *Astronomy and Computing* **15** (2016) 72–89.

[178] **VIRGO Consortium** Collaboration, R. E. Smith, J. A. Peacock, A. Jenkins, S. D. M. White, C. S. Frenk, F. R. Pearce, P. A. Thomas, G. Efstathiou, and H. M. P. Couchmann, *Stable clustering, the halo model and nonlinear cosmological power spectra*, *Mon. Not. Roy. Astron. Soc.* **341** (2003) 1311, [astro-ph/0207664].

[179] S. Bird, M. Viel, and M. G. Haehnelt, *Massive Neutrinos and the Non-linear Matter Power Spectrum*, *Mon. Not. Roy. Astron. Soc.* **420** (2012) 2551–2561, [arXiv:1109.4416].

[180] A. Mead, C. Heymans, L. Lombriser, J. Peacock, O. Steele, and H. Winther, *Accurate halo-model matter power spectra with dark energy, massive neutrinos and modified gravitational forces*, *Monthly Notices of the Royal Astronomical Society* **459** (2016), no. 2 1468–1488.

[181] J. Dakin, S. Hannestad, and T. Tram, *Fully relativistic treatment of decaying cold dark matter in n-body simulations*, *Journal of Cosmology and Astroparticle Physics* **2019** (2019), no. 06 032.

[182] M. Cataneo, L. Lombriser, C. Heymans, A. Mead, A. Barreira, S. Bose, and B. Li, *On the road to percent accuracy: non-linear reaction of the matter power spectrum to dark energy and modified gravity*, *Monthly Notices of the Royal Astronomical Society* **488** (2019), no. 2 2121–2142.

[183] **Planck** Collaboration, P. A. R. Ade et al., *Planck 2015 results. XIV. Dark energy and modified gravity*, *Astron. Astrophys.* **594** (2016) A14, [arXiv:1502.01590].

[184] H. Prince and J. Dunkley, *Data compression in cosmology: A compressed likelihood for planck data*, *Physical Review D* **100** (2019), no. 8 083502.

[185] J. Zuntz, M. Paterno, E. Jennings, D. Rudd, A. Manzotti, S. Dodelson, S. Bridle, S. Sehrish, and J. Kowalkowski, *Cosmosis: Modular cosmological parameter estimation*, *Astronomy and Computing* **12** (2015) 45–59.

[186] S. Kumar, R. C. Nunes, and S. K. Yadav, *Cosmological bounds on dark matter-photon coupling*, *Physical Review D* **98** (2018), no. 4 043521.

[187] R. Cawthon, C. Davis, M. Gatti, P. Vielzeuf, J. Elvin-Poole, E. Rozo, J. Frieman, E. S. Rykoff, A. Alarcon, G. M. Bernstein, et al., *Dark energy survey year 1 results: calibration of redmagic redshift distributions in des and sdss from cross-correlations*, *Monthly Notices of the Royal Astronomical Society* **481** (2018), no. 2 2427–2443.

[188] E. S. Sheldon and E. M. Huff, *Practical weak-lensing shear measurement with metacalibration*, *The Astrophysical Journal* **841** (2017), no. 1 24.

[189] N. Aghanim, Y. Akrami, M. Ashdown, J. Aumont, C. Baccigalupi, M. Ballardini, A. Banday, R. Barreiro, N. Bartolo, S. Basak, et al., *Planck 2018 results. v. cmb power spectra and likelihoods*, *arXiv preprint arXiv:1907.12875* (2019).

[190] A. Taruya, K. Koyama, T. Hiramatsu, and A. Oka, *Beyond consistency test of gravity with redshift-space distortions at quasilinear scales*, *Physical Review D* **89** (2014), no. 4 043509.

[191] A. Barreira, A. G. Sanchez, and F. Schmidt, *Validating estimates of the growth rate of structure with modified gravity simulations*, *Physical Review D* **94** (2016), no. 8 084022.

[192] G. Benevento, W. Hu, and M. Raveri, *Can late dark energy transitions raise the hubble constant?*, *Physical Review D* **101** (2020), no. 10 103517.

[193] M. Raveri and W. Hu, *Concordance and discordance in cosmology*, *Physical Review D* **99** (2019), no. 4 043506.

[194] W. Handley and P. Lemos, *Quantifying tension: interpreting the des evidence ratio*, *arXiv preprint arXiv:1902.04029* (2019).

[195] W. Wu, P. Motloch, W. Hu, and M. Raveri, *Hubble constant tension between cmb lensing and bao measurements*, *arXiv preprint arXiv:2004.10207* (2020).

[196] W. Handley, *anesthetic: nested sampling visualisation*, *The Journal of Open Source Software* **4** (Jun, 2019) 1414.

[197] K. H. Knuth, M. Habeck, N. K. Malakar, A. M. Mubeen, and B. Placek, *Bayesian evidence and model selection*, *Digital Signal Processing* **47** (2015) 50–67.

[198] H. Jeffreys, *Theory of probability, clarendon*, 1961.

[199] C. P. Robert, N. Chopin, J. Rousseau, et al., *Harold jeffreys's theory of probability revisited*, *Statistical Science* **24** (2009), no. 2 141–172.

[200] B. Giblin, M. Cataneo, B. Moews, and C. Heymans, *On the road to per cent accuracy–ii. calibration of the non-linear matter power spectrum for arbitrary cosmologies*, *Monthly Notices of the Royal Astronomical Society* **490** (2019), no. 4 4826–4840.

[201] G. d'Amico, J. Gleyzes, N. Kokron, K. Markovic, L. Senatore, P. Zhang, F. Beutler, and H. Gil-Marín, *The cosmological analysis of the sdss/boss data from the effective field theory of large-scale structure*, *Journal of Cosmology and Astroparticle Physics* **2020** (2020), no. 05 005.

[202] S. Kumar, R. C. Nunes, and S. K. Yadav, *Dark sector interaction: a remedy of the tensions between CMB and LSS data*, *Eur. Phys. J. C* **79** (2019), no. 7 576, [arXiv:1903.04865].

[203] S. Pan, W. Yang, E. Di Valentino, E. N. Saridakis, and S. Chakraborty, *Interacting scenarios with dynamical dark energy: Observational constraints and alleviation of the H_0 tension*, *Phys. Rev. D* **100** (2019), no. 10 103520, [arXiv:1907.07540].

[204] A. Hryczuk and K. Jodłowski, *Self-interacting dark matter from late decays and the H_0 tension*, *Phys. Rev. D* **102** (2020), no. 4 043024, [arXiv:2006.16139].

[205] A. Barreira, A. G. Sánchez, and F. Schmidt, *Validating estimates of the growth rate of structure with modified gravity simulations*, *Phys. Rev. D* **94** (2016), no. 8 084022, [arXiv:1605.03965].

[206] P. Carter, F. Beutler, W. J. Percival, J. DeRose, R. H. Wechsler, and C. Zhao, *The impact of the fiducial cosmology assumption on BAO distance scale measurements*, *Mon. Not. Roy. Astron. Soc.* **494** (2020), no. 2 2076–2089, [arXiv:1906.03035].

[207] B. D. Sherwin and M. White, *The Impact of Wrong Assumptions in BAO Reconstruction*, *JCAP* **02** (2019) 027, [arXiv:1808.04384].

[208] H. Gil-Marín, W. J. Percival, A. J. Cuesta, J. R. Brownstein, C.-H. Chuang, S. Ho, F.-S. Kitaura, C. Maraston, F. Prada, S. Rodríguez-Torres, et al., *The clustering of galaxies in the sdss-iii baryon oscillation spectroscopic survey: Bao measurement from the los-dependent power spectrum of dr12 boss galaxies*, *Monthly Notices of the Royal Astronomical Society* **460** (2016), no. 4 4210–4219.

[209] K. Aylor, M. Joy, L. Knox, M. Millea, S. Raghunathan, and W. L. K. Wu, *Sounds Discordant: Classical Distance Ladder \& ΛCDM -based Determinations of the Cosmological Sound Horizon*, *Astrophys. J.* **874** (2019), no. 1 4, [arXiv:1811.00537].

[210] R. Wojtak and A. Agnello, *The hubble–lemaître constant and sound horizon from low-redshift probes*, *Monthly Notices of the Royal Astronomical Society* **486** (2019), no. 4 5046–5051.

[211] A. Taruya, K. Koyama, T. Hiramatsu, and A. Oka, *Beyond consistency test of gravity with redshift-space distortions at quasilinear scales*, *Phys. Rev. D* **89** (2014), no. 4 043509, [arXiv:1309.6783].

[212] B. Bose, K. Koyama, W. A. Hellwing, G.-B. Zhao, and H. A. Winther, *Theoretical accuracy in cosmological growth estimation*, *Phys. Rev. D* **96** (2017), no. 2 023519, [arXiv:1702.02348].

[213] A. Taruya, T. Nishimichi, and S. Saito, *Baryon Acoustic Oscillations in 2D: Modeling Redshift-space Power Spectrum from Perturbation Theory*, *Phys. Rev. D* **82** (2010) 063522, [arXiv:1006.0699].

[214] **BOSS** Collaboration, A. G. Sanchez et al., *The clustering of galaxies in the completed SDSS-III Baryon Oscillation Spectroscopic Survey: cosmological implications of the configuration-space clustering wedges*, *Mon. Not. Roy. Astron. Soc.* **464** (2017), no. 2 1640–1658, [arXiv:1607.03147].

[215] M. Cataneo, L. Lombriser, C. Heymans, A. Mead, A. Barreira, S. Bose, and B. Li, *On the road to percent accuracy: non-linear reaction of the matter power spectrum to dark energy and modified gravity*, *Mon. Not. Roy. Astron. Soc.* **488** (2019), no. 2 2121–2142, [arXiv:1812.05594].

[216] B. Giblin, M. Cataneo, B. Moews, and C. Heymans, *On the road to per cent accuracy – II. Calibration of the non-linear matter power spectrum for arbitrary cosmologies*, *Mon. Not. Roy. Astron. Soc.* **490** (2019), no. 4 4826–4840, [arXiv:1906.02742].

[217] **Planck** Collaboration, N. Aghanim et al., *Planck 2018 results. VIII. Gravitational lensing*, *Astron. Astrophys.* **641** (2020) A8, [arXiv:1807.06210].

[218] G. Benevento, W. Hu, and M. Raveri, *Can Late Dark Energy Transitions Raise the Hubble constant?*, *Phys. Rev. D* **101** (2020), no. 10 103517, [arXiv:2002.11707].

[219] G. Efstathiou, *To h0 or not to h0?*, *arXiv preprint arXiv:2103.08723* (2021).

[220] A. G. Riess, L. M. Macri, S. L. Hoffmann, D. Scolnic, S. Casertano, A. V. Filippenko, B. E. Tucker, M. J. Reid, D. O. Jones, J. M. Silverman, et al., *A 2.4% determination of the local value of the hubble constant*, *The Astrophysical Journal* **826** (2016), no. 1 56.

[221] M. Raveri, G. Zacharegkas, and W. Hu, *Quantifying concordance of correlated cosmological data sets*, *Phys. Rev. D* **101** (2020), no. 10 103527, [arXiv:1912.04880].

[222] D. Foreman-Mackey, D. W. Hogg, D. Lang, and J. Goodman, *emcee: the mcmc hammer*, *Publications of the Astronomical Society of the Pacific* **125** (2013), no. 925 306.